A STUDY OF ELECTROMAGNETIC PROPERTIES OF EXCITED NUCLEAR STATES

'Se non è vero, è molto ben trovato.'

Giordano Bruno.

To My Parents, Brother, and Sisters.

LIBRARY
28.VII.67

A STUDY OF ELECTROMAGNETIC PROPERTIES OF EXCITED NUCLEAR STATES

by

Robin A.I. Bell

Worcester College

BODLEIAN LIBRARY OXFORD
DEPOSITED
THESIS
28. vii. 69.

A thesis submitted for the degree of Doctor of Philosophy in the University of Oxford

Trinity Term, 1969

C O N T E N T S

Page

ABSTRACT i

Acknowledgements

CHAPTER 1. MOTIVATION 1.1

CHAPTER 2. EXPERIMENTAL ARRANGEMENTS 2.1

2.1 The Tritium Beam Experiments 2.1

2.1. 1 Beam Line and Detectors 2.1

2.1. 2 Electronics 2.3

2.2 Neutron-Gamma Coincidence Experiments 2.4

2.2. 1 Neutron Detection 2.4

2.2. 2 Pulse Shape Discrimination 2.7

2.2. 3 P.S.D. Set-Up and Performance ... 2.11

2.2. 4 Gamma Detectors and Electronics .. 2.15

CHAPTER 3. ELECTROMAGNETIC FORMULAE AND DATA ANALYSIS 3.1

3.1 Electromagnetic Transition Formulae 3.1
(Matrix Elements and Angular Distributions)

3.2 Angular Correlation Analysis 3.8

3.2. 1 Substate Population; Finite Size Effects 3.8

Page

3.2. 2 Data Reduction; Legendre Fits 3.11

3.2. 3 Spin and Mixing Ratio Determination . 3.13

3.3 Doppler Shift Attenuation Lifetime Measurement 3.19

3.3. 1 Basic Principles 3.19

3.3. 2 Stopping Processes and $F(\tau)$ Calculations 3.21

3.3. 3 $F(\tau)$ Accuracy and Corrections 3.28

3.3. 4 $F(\tau)$ for Cascade Gamma Rays 3.32

3.3. 5 Centroid Determination and Error Formulae 3.34

CHAPTER 4. TRITIUM BEAM EXPERIMENTS: ^{11}B and ^{14}C ANGULAR CORRELATIONS 4.1

4.1 Introduction and Experimental Details 4.1

4.2 Experimental Results 4.7

4.2. 1 The 4.44 MeV level of ^{11}B 4.7

4.2. 2 The 5.02 MeV level of ^{11}B 4.7

4.2. 3 The 6.72 MeV level of ^{14}C 4.9

4.2. 4 The 7.01 MeV level of ^{14}C 4.10

4.2. 5 The 7.35 MeV level of ^{14}C 4.11

CHAPTER 5. NEUTRON-GAMMA ANGULAR CORRELATIONS: ^{18}Ne and ^{19}Ne 5.1

5.1 Introduction 5.1

5.2 ^{18}Ne Results 5.2

5.2. 1 Level Positions and Decay Schemes ... 5.2

Page

5.2. 2 The 1.89 MeV level of ^{18}Ne 5.9

5.2. 3 The 3.38, 3.58 and 3.62 MeV levels of ^{18}Ne 5.13

5.2. 4 Experimental Conclusions for ^{18}Ne .. 5.16

5.3 ^{19}Ne Results 5.17

5.3. 1 Introduction 5.17

5.3. 2 Results (levels below 3 MeV) for ^{19}Ne 5.20

5.3. 3 Conclusions for ^{19}Ne 5.23

CHAPTER 6. NEUTRON-GAMMA COINCIDENCE LIFETIME MEASUREMENTS: ^{26}Si 6.1

6.1 Introduction 6.1

6.2 Experimental Arrangements 6.3

6.2. 1 General 6.3

6.2. 2 Distant Geometry Lifetime Measurements 6.4

6.2. 3 Close Geometry Lifetime and Decay Measurements 6.7

6.3 Experimental Results for ^{26}Si 6.9

6.3. 1 The 1.80 MeV level of ^{26}Si 6.9

6.3. 2 The 2.78, 3.33 and 4.14 MeV levels of ^{26}Si 6.15

6.3. 3 Decay Schemes, higher states 6.17

6.3. 4 The 3.76 and 3.84 MeV levels of ^{26}Si 6.18

6.3. 5 The 4.09, 4.45, and 4.81 MeV levels of ^{26}Si 6.20

Page

CHAPTER 7. DISCUSSION OF RESULTS 7.1

7.1 The 4.44 and 5.02 MeV levels of ^{11}B 7.1

7.2 The ^{14}C Results 7.6

7.2. 1 Introduction 7.6

7.2. 2 The 6.72 MeV level of ^{14}C 7.10

7.2. 3 The 7.01 MeV level of ^{14}C 7.15

7.2. 4 The 7.35 MeV level of ^{14}C 7.18

7.3 The ^{18}Ne Results 7.20

7.3. 1 Deformed v. Shell Model States ... 7.20

7.3. 2 Deformed State Wavefunctions and Matrix Elements 7.23

7.3. 3 Comparison of Theory and Experiment for ^{18}Ne 7.28

7.4 The ^{26}Si Results 7.31

7.4. 1 Spins, Parities and Transition Strengths 7.31

7.4. 2 The 1.80, 2.78 and 3.33 MeV levels of ^{26}Si 7.31

7.4. 3 The 3.76, 3.84, 4.09, 4.14, 4.45 and 4.81 MeV levels of ^{26}Si 7.33

7.4. 4 Analogue levels in mass 26 ..... 7.34

7.4. 5 Shell model calculations for mass 26 ..... 7.35

REFERENCES R.1

ABSTRACT

Gamma decays of excited states of ^{11}B, ^{14}C, ^{18}Ne, ^{19}Ne, and ^{26}Si have been studied experimentally and the results used to test the predictions of various nuclear models. The phase-consistent Rose and Brink treatment of electromagnetic transitions was used throughout.

States of ^{11}B and ^{14}C were studied using the reactions $^{12}C(t,\alpha)^{11}B$ and $^{12}C(t,p)^{14}C$ in conjunction with a conventional charged particle-gamma ray coincidence angular correlation technique. For the ^{11}B, 4.44 MeV, $J = 5/2$ level previous measurements of the ground state decay mixing ratio were confirmed ($\delta = -0.19 \pm 0.015$). For the ^{11}B, 5.02 MeV level the spin was found to be $J = 3/2$; the mixing ratio of the ($88 \pm 2.5\%$) transition to the ground state was measured to be $\delta = 0.03 \pm 0.05$, and that of the 5.02 $\rightarrow$ 2.12 MeV transition $\delta = -0.05 \pm 0.2$. The results for both ^{11}B levels are in substantial agreement with the predictions of intermediate coupling calculations.

The results for ^{14}C levels are summarised in the table (where parities and final state spins have been taken from the literature).

^{14}C Results

Transition (MeV)	Initial J^π	Final J^π	Branch (%)	Mixing Ratio δ
6.72 → g.s.	3^-	0^+	97.3 ± 1.0	0
6.72 → 6.09	3^-	1^-	2.7 ± 1.0	-
7.01 → g.s.	2^+	0^+	98.6 ± 0.7	0
7.01 → 6.09	2^+	1^-	1.4 ± 0.7	-
7.35 → g.s.	2^-	0^+	14 ± 4	0
7.35 → 6.09	2^-	1^-	52 ± 5	-0.04 ± 0.09
7.35 → 6.72	2^-	3^-	34 ± 4	0.07 ± 0.3

The results are compared to predictions of True's model of ^{14}C, in which the active particles are two neutrons in the $1p_{1/2}$, $2s_{1/2}$, $1d_{3/2}$ and $1d_{5/2}$ shells. For the 6.72 MeV level agreement is good, but the 7.01 → 6.09 MeV and the 7.35 MeV → g.s. decays are predicted too strong. The explanation probably lies in excitation of the $1p_{3/2}$ core particles, as considered by Sebe.

The bound states of ^{18}Ne were studied using the $^{16}O(^3He,n)^{18}Ne$ reaction in conjunction with a neutron-gamma ray coincidence angular correlation technique. Neutrons were detected in a large liquid scintillator using pulse shape discrimination. Gamma ray detection in large-volume Ge(Li) counters enabled separation of the level-decays under study.

The missing $J^{\pi} = 0^+$ level was found at 3.58 MeV and its origin in ^{18}Ne confirmed. The decay schemes and mixing ratios are shown below. The level spins and parities above 2 MeV have been deduced by synthesis of the present results with published ^{18}Ne level lifetimes and double stripping studies, and by analogies with the mirror nucleus ^{18}O.

^{18}Ne Results

Transition (MeV)	Initial J^{π}	Final J^{π}	Branch (%)	Mixing Ratio δ
3.38 → 0	4^+	0^+	<4	
→ 1.89	4^+	2^+	100	$+0.06 \pm 0.07$
3.58 → 0	0^+	0^+	<17	
→ 1.89	0^+	2^+	100	
3.62 → 0	2^+	0^+	<9	
→ 1.89	2^+	2^+	100	$-1.1 \,^{+1.0}_{-0.3}$

The ^{18}Ne results are shown to be in good accord with the predictions of the Benson-Irvine model which includes a deformed 4-particle-2-hole component in the wavefunctions along with the conventional two-proton $(sd)^2$ configurations.

Decays of excited states of ^{19}Ne below 3 MeV were similarly studied using the ^{19}F(p,n)^{19}Ne reaction. By

synthesis with published lifetimes, and by analogy with levels of the mirror nucleus ^{19}F, the results in the table were obtained:

^{19}Ne Results

Transition (MeV)	Initial J^π	Final J^π	Branch (%)	Mixing Ratio (δ)
1.51 → g.s.	$5/2^-$	$1/2^+$	<3	-
1.51 → 0.24	$5/2^-$	$5/2^+$	12 ± 7	-
1.51 → 0.28	$5/2^-$	$1/2^-$	88 ± 3	0.1 ± 0.2
1.54 → g.s.	$3/2^+$	$1/2^+$	<7	-
1.54 → 0.24	$3/2^+$	$5/2^+$	100	-
1.54 → 0.28	$3/2^+$	$1/2^-$	<7	-
1.62 → g.s.	$3/2^-$	$1/2^+$	20 ± 2	-
1.62 → 0.24	$3/2^-$	$5/2^+$	10 ± 2	-
1.62 → 0.28	$3/2^-$	$1/2^-$	70 ± 2	-
2.79 → g.s.	$9/2^+$	$1/2^+$	<10	-
2.79 → 0.24	$9/2^+$	$5/2^+$	100	0.0 ± 0.1
2.79 → 0.28	$9/2^+$	$1/2^-$	<10	-
2.79 → 1.51	$9/2^+$	$5/2^-$	<12	-
2.79 → 1.54	$9/2^+$	$3/2^+$	<10	-
2.79 → 1.62	$9/2^+$	$3/2^-$	<10	-

Levels of ^{26}Si were studied using the reaction $^{24}Mg(^3He,n)^{26}Si$. Decay schemes and level energies were

determined, and the Doppler-shift attenuation method was used to measure level lifetimes. The results are shown in the table.

^{26}Si Results

Level Energy (keV)	Lifetime (ps)	Transition to (keV)	Branch (%)	Initial J^{π}
1795.9 ± 0.2	$1.38^{+0.7}_{-0.5}$	g.s.	100	2^+
2783.5 ± 0.4	$0.20^{+0.20}_{-0.12}$	g.s.	30 ± 5	2^+
		1796	70 ± 5	
3332.5 ± 0.3	$2.7^{+2.3}_{-1.0}$	1796	100	0^+
3756 ± 2	< 0.7	1796	70 ± 10	(3^+)
		2784	30 ± 10	
3842 ± 2	-	1796	100	(4^+)
4093 ± 3	-	g.s.	100	
4138 ± 1	$0.11^{+0.11}_{-0.10}$	g.s.	20 ± 10	
		1796	80 ± 10	
4445 ± 3	< 0.5	1796	100	
4805 ± 2	< 0.1	1796	30 ± 10	
		2784	70 ± 10	

J^{π} for the 3756 and 3842 keV levels have been deduced

from the observed decay widths and from mirror level arguments; others are from the literature.

The results are compared to shell-model calculations for ten particles in the $2s_{1/2}$-$1d_{5/2}$ orbitals using the two-nucleon matrix elements of Wildenthal (from an effective interaction fit to level energies) and of Kuo (based on the realistic Hamada-Johnston potential). Neither calculation gives a good description, though the Kuo predictions are better overall. Discrepancies underline the importance of including the $1d_{3/2}$ orbital in such calculations.

ACKNOWLEDGEMENTS

"No man is an Ilande, intire of itselfe".

John Donne.

It is a great pleasure to acknowledge the supervision of this work by Dr. H.J. Rose, whosecontinued advice, criticism and guidance have been invaluable to me.

I should like to thank Professor D.H. Wilkinson, F.R.S., and Professor K.W. Allen, for extending to me the use of the facilities of the Nuclear Physics Laboratory during my stay in Oxford. I am also grateful to Mr. E. Sparrow for the use of the 6 MeV Van der Graaff at A.E.R.E., Harwell, and to Dr. J.H. Towle for the use of the Tandem Van der Graaff at A.W.R.E., Aldermaston.

It has been the greatest pleasure to work with Dr. R.D. Gill, Mr. B.C. Robertson, and Dr.J. L'Ecuyer at Oxford and I must thank them for much assistance with these experiments. I am also indebted to Dr. Gill for the time he has spent reading this manuscript. I should like to thank Dr. B.E.F. Macefield, Dr. S. Mubarakmand, and Dr. B. Wakefield for invaluable discussions concerning neutron detection; and

Dr. I.S. Towner who kindly used his shell model program for the ^{26}Si calculations.

I am grateful to Mr. J. Takacs, Mr. E. Valentine, and Mr. D. Field for advice and assistance with electronics; to Mr. G. Parker, Mr. S.A. Tolan, and Mr. W. Sanford and their workshop staffs for their willing and obliging help in constructing apparatus; to Mr. H.R. McK.Hyder, Mr. W.W. Evans, and the operators of the Oxford accelerators for their co-operation and assistance; and to Mr. L.G. Waine for his unfailing tolerance of my efforts in the graduate workshop.

I am particularly grateful and indebted to my parents for their continuing support, interest, and encouragement. I should also like to thank the New Zealand University Grants Committee for a Postgraduate Scholarship, the Scott Fund and Advanced Studies Committee for grant assistance, and Dr. F.V. Price and Worcester College for their hospitality in Oxford and a Martin Scholarship.

Finally I should like to thank Mrs. E. Browne for her painstaking typing of this thesis.

'Where shall I begin please your Majesty?' he asked.
'Begin at the beginning', the King said, gravely,
'and then go on till you come to the end: then stop.'

Lewis Carroll.

C H A P T E R 1

MOTIVATION

The value of electromagnetic phenomena as tools for studying nuclear structure has long been recognised; it stems from two observations. Firstly, the nature of the electromagnetic interaction is well understood: as a result predictions can be made and results interpreted with considerable precision and clarity. This is in contrast to calculations involving the less well understood strong nuclear forces where (partly also because of inherent many-body aspects) the predictions and interpretations are less clear-cut. An example would be the simplicity of interpretation of Coulomb excitation experiments as contrasted to the difficulty of unambiguously interpreting double-stripping experiments.

The second point arises from the different natures of the two interactions: electromagnetic observations can throw light on aspects of nuclear structure in a useful and revealing way. One example is the relationship of gamma decay modes to collective band structure, another is the sensitivity of many electromagnetic transition rates to

wavefunction admixtures.

An experimental technique which has proved of great value in the study of electromagnetic transitions is the measurement of the angular distribution of gamma radiation following the decay of an aligned nuclear state. From such angular distributions information may be obtained on spins and (observing linear polarization) parities of the states concerned, and on the relative amplitudes of the electromagnetic multipoles contributing to the decay. All these properties can be compared with predictions calculated from various nuclear models.

The literature on gamma ray angular distributions is vast. A recent review article is that of Frauenfelder and Steffen in (Si 67). One of the most powerful techniques is that of particle-gamma angular correlations where alignment of the nuclear state produced in a reaction is achieved by detection of the emerging light particles on or close to the incident beam axis. The angular correlation of gamma rays in coincidence with these particles is then measured. The usefulness of this technique was greatly enhanced by the development of annular silicon surface barrier counters so that the incident beam reaches the target through the detector's central hole and charged particles from the

reaction are detected close to 180°. The good particle-energy resolution enables study of the gamma decays of separate energy levels using high-efficiency NaI(Tl) gamma detectors. Use of this technique has been very fully discussed by Litherland and Fergusson (Li 61).

The theory of gamma ray angular distributions grew in a rather haphazard manner. In particular phase-conventions for the electromagnetic multipole decay amplitudes were rather ill-defined so that it was difficult to relate experimental observations to model predictions. Rose and Brink have recently (Ro 67) given a phase-consistent treatment of the subject in which the ambiguities are resolved so that full use can be made of the experimental information to test nuclear models. Their formalism and conventions will be followed here.

The nuclei ^{11}B and ^{14}C lie within the nuclear 1p shell where the intermediate coupling model has had considerable success in explaining nuclear level schemes (Ku 56; Co 65). Electromagnetic decays of the low-lying levels of these nuclei provide a further more refined test of the model. The particle-gamma correlation method is well suited to study these decays using the reactions $^{12}C(t,\alpha)^{11}B$ and $^{12}C(t,p)^{14}C$ and a description of these experiments forms

the subject of Chapter 4 of this thesis.

Although angular correlations can determine the relative amplitudes of different multipoles contributing to a transition, the interesting absolute widths cannot be determined. Of particular interest vis-à-vis model calculations are transitions where collective effects in the nucleus enhance E2 transition strengths, often to the point where they compete with an M1 decay. Such decays often correspond to level lifetimes in the region 10^{-11} to 10^{-14} seconds, for the measurement of which the Doppler shift attenuation method is particularly suited. This technique depends on measurement of the reduction in the mean Doppler shift of gamma rays emitted by nuclei which are initially fast-moving, but which are brought to rest (usually in a solid medium) in a time comparable to the excited state lifetime. Reviews of this method may be found in (Li 63; Bl 66; Si 67).

The usefulness of the Doppler shift method was greatly enhanced by the development of large volume Ge(Li) counters offering resolutions of a few keV and useable detection efficiencies for gamma rays of energy up to several MeV; the reason being that nuclei recoiling from a reaction induced by a light incident particle at typical Van der

Graaff energies have velocities typically 1 - 2% of that of light. Typical gamma ray Doppler shifts of the order of 10 keV result and high resolution detectors greatly facilitate accurate measurement of these shifts.

These large Ge(li) counters have also made it possible to carry out neutron-gamma coincidence experiments with adequate separation of the levels under study. A number of proton-rich nuclei are reached most conveniently by reactions in which a neutron is emitted. Hitherto, with NaI(Tl) gamma detectors having energy resolutions of 5 - 8%, the decays of different levels of such nuclei could not be separated for no efficient neutron detector exists with energy resolution comparable to that of the surface-barrier charged particle detector. These proton-rich nuclei are of considerable interest because of the comparison which can be made with the usually well studied neutron-rich mirror nucleus. For instance collective effects have been found to be important (Be 69) in the nuclei ^{18}O and ^{19}F which lie at the beginning of the 2sld shell, although it was initially expected that they would be well described by a model in which two and three nucleons respectively moved in 2sld orbitals about an inert core of sixteen nucleons in the ls and lp shells (Ar 68).

Electromagnetic properties of the corresponding proton-rich mirror nuclei, ^{18}Ne and ^{19}Ne, are therefore of interest and in Chapter 5 neutron-gamma ray angular correlation studies of these nuclei are described. The reactions ^{16}O(^{3}He,n)^{18}Ne and ^{19}F(p,n)^{19}Ne were used and Ge(Li) counters enabled separation of the various gamma rays under study.

Another proton-rich nucleus of interest is ^{26}Si which lies in the middle of the 2s1d shell. Although shell and collective models have had some success in explaining properties of ^{24}Mg and ^{28}Si, no satisfactory account of the properties of ^{26}Mg has been given (Rob 68). Further information on the mass 26 nuclei should be useful. In Chapter 6 experiments are described where the ^{24}Mg(^{3}He,n)^{26}Si reaction and the neutron-gamma coincidence technique with Ge(Li) counters are used to make Doppler shift measurements of level lifetimes in ^{26}Si.

In Chapter 7 the experimental results for ^{11}B, ^{14}C, ^{18}Ne and ^{26}Si are considered in the light of various nuclear models. The results for ^{19}Ne are to be discussed elsewhere (Bh 70). Firstly however the experimental arrangements for the various experiments are discussed in Chapter 2, and in Chapter 3 electromagnetic formulae are reviewed and the

methods of analysing angular correlation and Doppler shift experiments are described.

'With a name like yours, you might be any

shape, almost.'

Lewis Carroll.

CHAPTER 2

EXPERIMENTAL ARRANGEMENTS

2.1 The Tritium Beam Experiments

2.1. 1 Beam line and detectors

The tritium beam was provided by the Tandem Van de Graaff Accelerator at A.W.R.E., Aldermaston. The beam was collimated by a series of eight tantalum annuli, the inner diameters of which were graded from 4 mm down to 2 mm approaching the target. This gradation gave optimum transmission when the beam was correctly focussed at the target. Separating the tantalum annuli were coaxial lead cylinders 8 cm long, 8 cm in diameter, and of central bore 1 cm. These served to strongly attenuate gamma rays arising where the beam struck the collimator annuli. Emerging from the collimator the beam passed through the 5 mm diameter centre hole of an annular surface barrier counter (the mounting of which was bolted directly to the collimator), through the target, and finally to a thick insulated tantalum beam stop some 5 metres away, at which the beam current was monitored. Current striking the collimator, which was also insulated, was monitored as a

focussing aid to the operators of the accelerator.

A glass target chamber surrounded both detector and target, facilitating examination of target position and condition. The counter-target distance was 4 cm and particles emitted between 168° and 174° to the beam direction were detected. A cylindrical piece of tantalum in the detector annulus ensured that fringes of the beam passing through could not strike the detector; for a similar reason the glass target chamber exit tube was lined with tantalum foil to prevent excessive background in the NaI(Tl) crystals when these were at forward angles.

NaI(Tl) crystals to detect the gamma rays were mounted on trolleys which rotated on a horizontal table, the axis of which passed vertically through the target. Telescope, cross-wires, and plumbline were used to align the various beamline components, including the correlation table axis and angle markings. Isotropy of the gamma detectors was essential for angular correlation work and at various times the following checks were used:

(i) Observation of the isotropic gamma radiation from a level known to have spin J = 0 or $^1/_2$ (e.g., the ^{11}B, J = $^1/_2$, 2.12 MeV level).

(ii) Similar observation, but replacing the target by a

carefully centred 1 mm diameter RdTh source.

(iii) Precise measurement at various angles of the NaI(Tl) counter distances from the beam spot.

The glass target chamber wall was cylindrical and of virtually constant radial thickness, and thus introduced no anisotropy. (A small (1-2%) attenuation correction was made for low energy gamma rays when extracting decay schemes.) Following correction for any observed anisotropy ((i) - (iii) above), the gamma detection efficiency was angle-independent to 1-2%.

A schematic drawing of the beamline and correlation apparatus is shown in fig. 2.1A.

2.1. 2 Electronics

The electronic set-up was a standard fast-slow coincidence arrangement using mainly Harwell and Oxford 2000 series modules. A schematic of a typical section of the arrangement is shown in fig. 2.1B. Points to note are:

(i) Digital stabilization of the particle detector gain which enabled setting and maintainance of accurate, narrow particle windows. This was of particular value as the detector aged during use and its performance deteriorated.

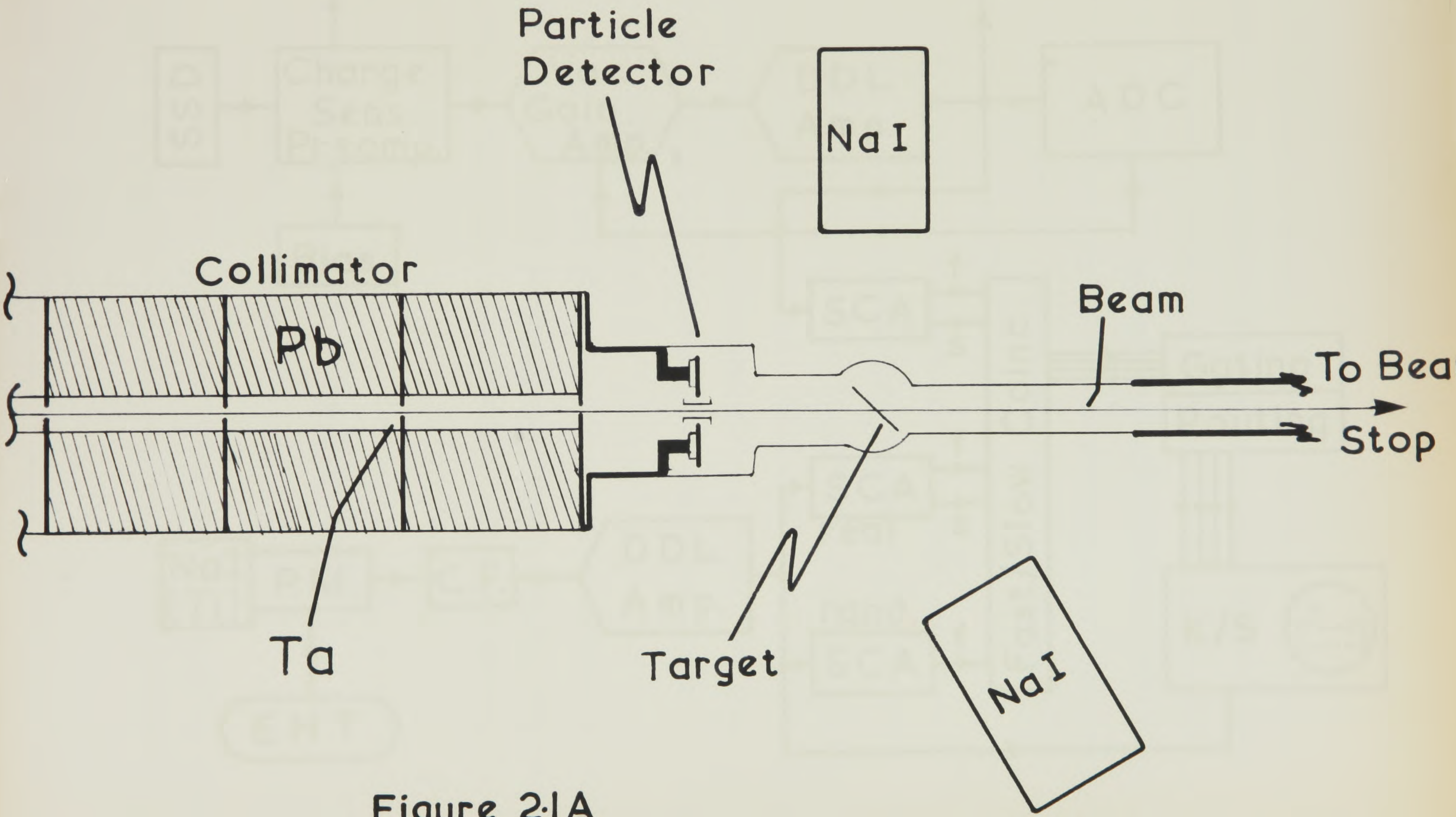

Particle
Detector
NaI
Collimator
Pb
Beam
To Beam
Stop
Ta
Target
NaI

Figure 2.1A

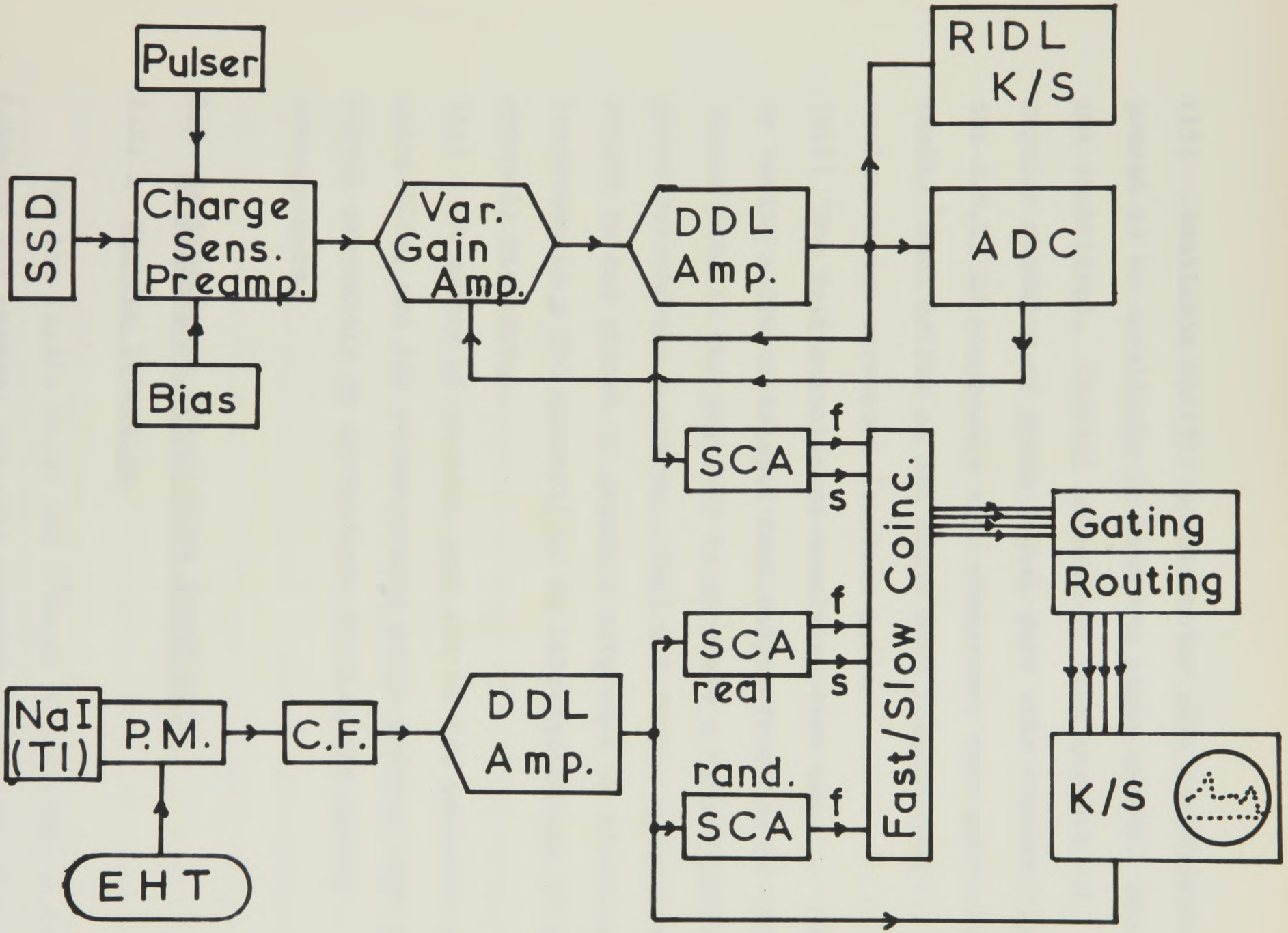

Pulser
RIDL
K/S
SSD
Charge
Sens.
Preamp.
Var.
Gain
Amp.
DDL
Amp.
ADC
Bias
SCA
f
s
Fast/Slow Coinc.
Gating
Routing
SCA
real
rand.
SCA
NaI
(Tl)
P.M.
C.F.
DDL
Amp.
K/S
EHT

Figure 2·1B

(ii) Available NaI(Tl) spectrometer gain stabilizers proved to be unreliable so that the gamma spectra were not stabilised. Careful control of beam current and regular checking of gamma signal gain with sources (using the E.H.T. to compensate when necessary) kept gain changes small. Such drifts as did occur were subsequently evaluated and corrected (section 4.1).

(iii) The fast coincidence resolving time was $\sim$ 40 ns. By taking a 200 ns delayed fast output from one of the gamma signal SCAs it was possible to generate a random particle-gamma coincidence spectrum. Real and random spectra were routed to and stored in separate subgroups of either a Victoreen (4 x 100 channel) or an Intertechniques (8 x 256 channel) kicksorter.

(iv) A number of windows were set on the particle spectrum using SCAs, and the corresponding gamma spectra were also stored separately by appropriate routing and gating arrangements.

2.2 Neutron-Gamma Coincidence Experiments

2.2.1 Neutron Detection

For the (p,n), (α,n) and (^{3}He,n) experiments a neutron detector was needed; the most important requirements for

this detector were high detection efficiency, good timing and count rate capability, and efficient discrimination against the gamma radiation accompanying any such reaction. Of the many neutron detection systems available (Ma 63; Si 66) an NE213 liquid scintillator coupled to a fast photomultiplier and pulse shape discrimination system was by far the most suitable and met all the above requirements. The only competitive alternative would have been a large Li^6 I (Eu) scintillator, which would have had the advantage over NE213 of giving useful neutron energy resolution (Mu 58). For many experiments however the high gamma energy resolution of a Ge(Li) detector was sufficient to overcome this problem; in view of this, and because of the great expense and untried nature of large Li^6 I (Eu) scintillators, the NE213 scintillator was chosen.

The thickness of the scintillator was dictated by requiring reasonably efficient neutron detection up to about 5 MeV. At this energy the total hydrogen and carbon cross-sections to neutrons are 1.7 and 1.0 bn respectively, and their densities in NE213 are 0.05 and 0.04 atoms/bn-cm. It then follows that the efficiency of a 15 cm long detector for 5 MeV neutrons will be roughly 70%. This includes a conservative estimate of the increased efficiency due to

the influence of carbon collisions (Ba 61). If the diameter is comparable to the length then multiple scattering within the scintillator raises the efficiency and increases the relative number of large pulses in the scintillation spectrum. On the other hand, for efficient light collection the photocathode of the photomultiplier should cover as large a fraction of the scintillator end face as possible.

The result of these considerations was a 15 cm long x 12.5 cm diameter NE213 liquid scintillator[x] viewed by a Mullard XP1040 fast photomultiplier having an 11 cm diameter photocathode. Mu-metal shields[≠] surrounding the PM (photomultiplier) screened it from stray magnetic fields and so reduced dependence of the gain on physical orientation. The liquid scintillator was encapsulated in a glass cylinder, all but one end of which was coated with a matt white TiO_2 reflecting paint to increase optical efficiency. The clear end was optically coupled to the PM face with Dow-Corning C-20057 silicone grease[ø], and the entire assembly was

---

x Purchased from Nuclear Enterprises Ltd., Sighthill, Edinburgh, Scotland.

≠ Telcon Metals Ltd., Manor Royal, Crawley, Sussex, England.

ø Midland Silicones Ltd., Barry, Glamorgan, Wales.

encased in a light-tight brass sheath. To this in turn the dynode chain assembly was attached.

The NE213 scintillator was mounted on the correlation table at 0° to the beam axis (fig. 2.2A). Because no charged particle detector was needed a 1.8 cm diameter glass target chamber was mounted on a similar diameter aluminium pipe extending from the collimator. This allowed Ge(Li) counter backward angles as great as 160°. It was found necessary to line both aluminium and glass components with tantalum foil to avoid unwanted neutron-gamma coincident pairs - particularly from the $^{27}Al(^{3}He,pn)^{28}Si$ reaction to the 1.779 MeV level of ^{28}Si (Q = +3.884 MeV). The beam was stopped immediately behind the target in a 100 - 200 mgm/cm^2 foil of gold, lead, or tantalum; beam current was monitored at this point.

2.2. 2 Pulse Shape Discrimination

It is a characteristic of many scintillators that the light output v. time curve is a function not only of the energy, but also of the nature of the exciting particle. This fact may be very usefully employed to distinguish neutron and gamma induced pulses in NE213 liquid scintillator. The pulse shape can often be fairly accurately described

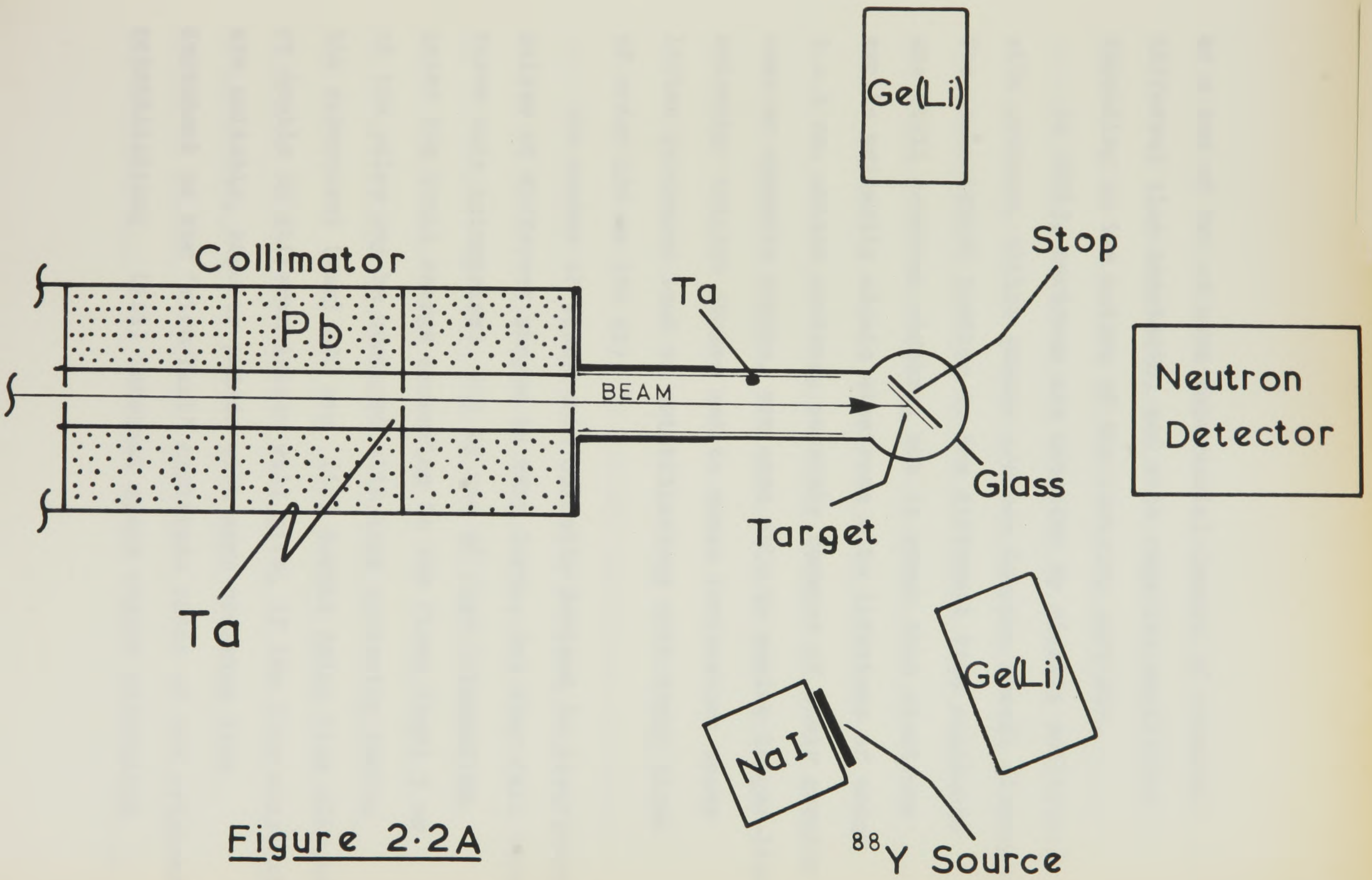

Ge(Li)
Collimator
Pb
Ta
Stop
BEAM
Neutron
Detector
Glass
Target
Ta
Ge(Li)
NaI
88Y Source

Figure 2·2A

as a sum of two or more exponential decays of somewhat different time constants, and with relative amplitudes depending on the nature of the ionizing particle.

In NE213, neutrons are detected by elastic collisions with protons, whilst gammas produce Compton recoil electrons. The mechanism(s) leading to the different time constants are still somewhat obscure, but it seems that electrons excite primarily atomic electrons with lifetimes of order 3 - 5 ns, whilst protons, possibly because of their greater mass or opposite charge, are more able to excite longer-lived molecular triplet states and to cause ionization: these latter processes lead to scintillations with decay times of order 120 ns (Pe 62).

The number of electronic circuits devised to discriminate pulses of different shapes is very large, but they fall into three main categories: (i) by use of fast integrating gates the total charge appearing in the first (say) 5 ns of the pulse may be compared with that appearing during the subsequent (say) 120 ns; (ii) double delay line clipping or double RC differentiation will give, if the time constants are suitable, bipolar pulses with zero crossing time dependent on the "slow/fast" amplitude ratio of the original scintillation; (iii) internal space charge saturation

effects may be produced in the photomultiplier (by suitable choice of electrode potentials) in such a way that pulses with a "slow" component produce a positive output pulse which is absent from solely "fast" pulses.

Circuits of all three types were tested. Those of class (i) were potentially the best but required very careful setting up, and with available integrating gates had a dead time exceeding 10 μs which too severely restricted count rate. A recently published circuit would appear to have overcome these problems, but was not available in 1966 (Jo 68).

Likewise the cross-over time walk, noise level, and time jitter of available RC and DDL amplifiers and cross-over discriminators gave inferior results using method (ii). Satisfactory n-γ discrimination was only achieved for $E_n > 2$ MeV, although when using DDL amplifiers quite high count rates could be handled ($\sim 5 \times 10^4$ c/s). The circuit finally adopted was a combination of methods (ii) and (iii). It is based on a space charge saturation technique first proposed by Owen (Ow 58; Ow 62), and improved by Batchelor et al. (Ba 60), who introduced cross-over timing to eliminate high energy gamma pulses which passed the original Owen discriminator when it was set for minimum

E_n threshold. Further improvement in the system described here results from the use of modern NIM system electronics. Fast double delay line amplifiers (DDLA) and timing single channel analysers (TSCA) permitted pulse handling rates exceeding 2×10^5 c/s, whilst replacement of a fast coincidence unit by a time-to-amplitude converter (TAC) greatly simplified and standardised the set-up procedure.

The high gain XP1040 dynode chain and the associated electronics are shown in fig. 2.2B. The voltage between the last dynode and the anode is of the order of 1 volt so that the tube space charge saturates the region between the last dynode and the anode during the initial high intensity pulse due to the large, fast decaying component of the scintillation. This drives the last dynode negative. The subsequent slow component is of much lower intensity so that the space charge clears and the dynode takes on a positive voltage. Because neutron-induced pulses contain a higher proportion of slow component for a given total charge, it is possible to adjust the last dynode-to-anode voltage (and hence the space charge clearing time) so that these (neutron) pulses swing positive roughly 1 μs earlier than gamma pulses.

Thus one obtains from the last dynode a "shape" pulse,

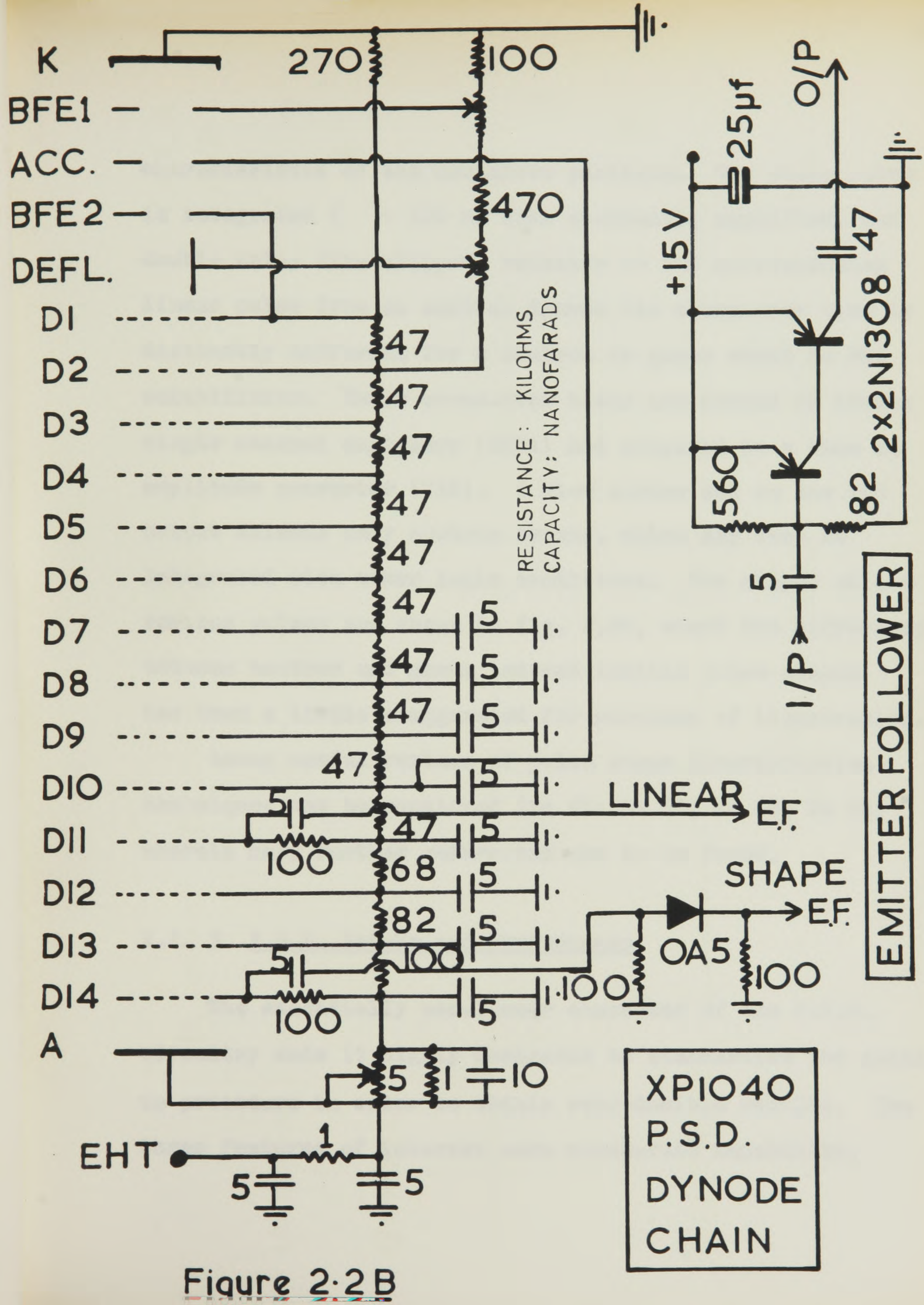

K
BFE1
ACC.
BFE2
DEFL.
D1
D2
D3
D4
D5
D6
D7
D8
D9
D10
D11
D12
D13
D14
A
EHT
270
100
470
47
5
100
68
82
1
10
RESISTANCE: KILOHMS
CAPACITY: NANOFARADS
LINEAR
E.F.
SHAPE
E.F.
OA5
.100
25µf
O/P
+15 V
560
82
2x2N1308
I/P
EMITTER FOLLOWER
XP1040
P.S.D.
DYNODE
CHAIN

Figure 2·2B

characteristic of the causative particle. The shape pulse is integrated ($\sim$ 100 ns time constant), amplified, and double delay line clipped: relative to the corresponding linear pulse from an earlier dynode its cross-over time is distinctly different for a neutron or gamma event in the scintillator. These cross-over times are sensed by timing single channel analysers (TSCA) and compared in a time to amplitude converter (TAC). A slow window set on the TAC output selects only neutron events, which may then be integrated with other logic conditions. The shapes of the various pulses are shown in fig. 2.2C, where the difference between neutron and gamma induced initial pulse shapes has been a little exaggerated for purposes of illustration.

Among useful reviews of pulse shape discrimination techniques may be mentioned (Ba 61; Ow 62; Jo 68; NE 68) wherein many further references are to be found.

2.2. 3 P.S.D. Set-Up and Performance

The essentially non-linear character of the P.S.D. circuitry made it highly desirable to standardise the setting-up procedure in order to obtain reproducible results. The three features of interest were count-rate capability,

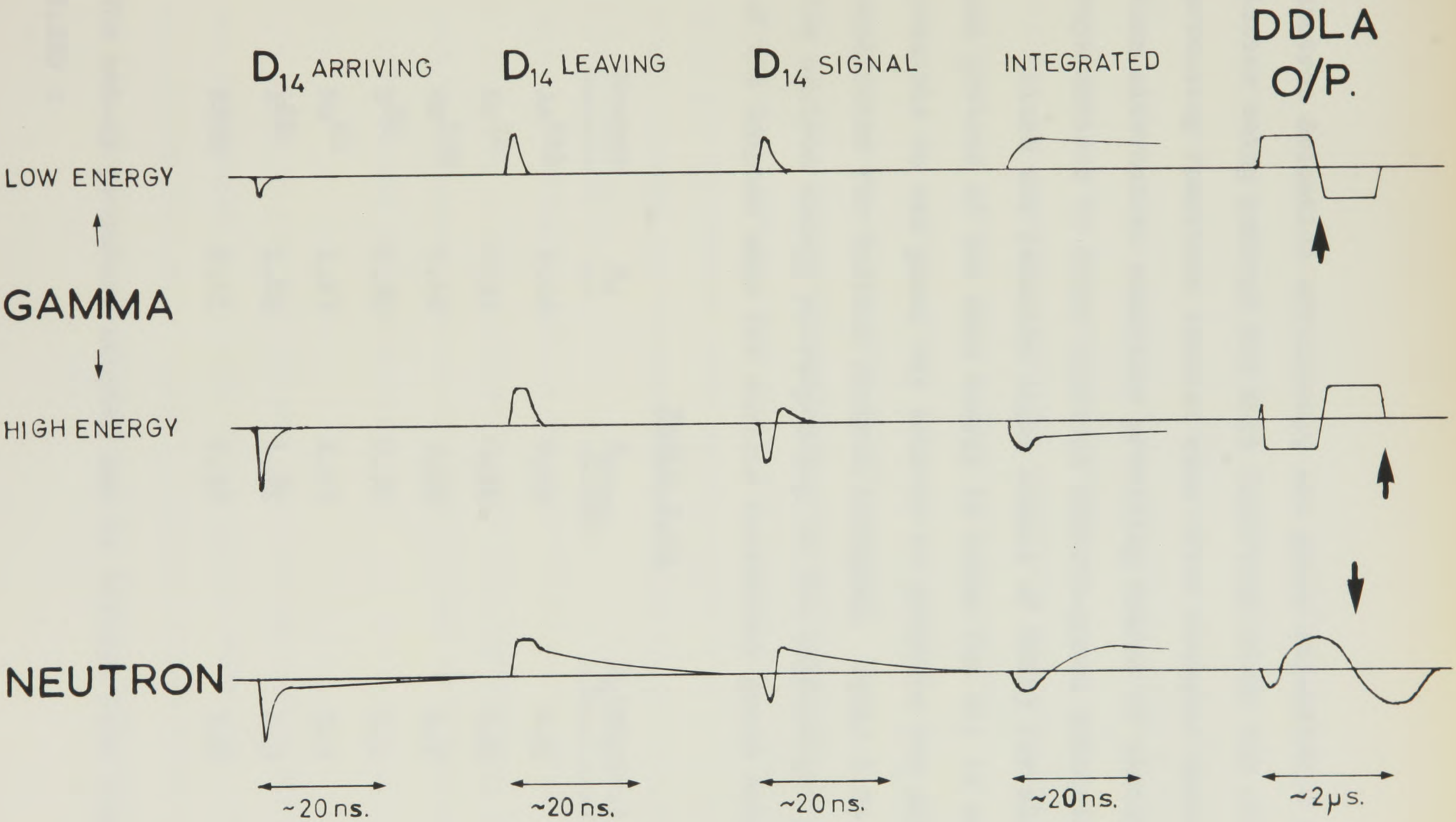

D_{14} ARRIVING
D_{14} LEAVING
D_{14} SIGNAL
INTEGRATED
DDLA O/P.
LOW ENERGY
GAMMA
HIGH ENERGY
NEUTRON
~20 ns.
~20 ns.
~20 ns.
~20 ns.
~2 μs.

Figure 2·2C

neutron detection efficiency, and gamma rejection - the latter being perhaps the most important since the neutron-producing reactions studied were often somewhat weaker than alternative reactions providing swarms of cascade gamma rays anxious to cause spurious neutron-gamma coincidences.

Since the relative light output of NE213 for electrons and protons of the same energy is known (Ba 61) it was possible to use gamma ray sources to estimate the pulse amplitudes for various neutron energies. Table 2.2A shows the neutron energy corresponding to the half-height position of the Compton edge for various convenient gamma sources.

TABLE 2.2A

Source	E_γ	$E_{Comp.}$	E_n(equiv.)
Am^{241}	0.06	0.05	0.4
Na^{22}	0.51	0.34	1.4
Cs^{137}	0.66	0.48	1.7
Y^{88}	0.89	0.70	2.1
Na^{22}	1.27	1.07	3.3
Y^{88}	1.84	1.61	4.3
RdTh	2.61	2.37	5.8

The set-up procedure adopted was as follows (see also fig. 2.2E) :

(i) Adjust neutron linear DDL amplifier gain to just not overload pulses from a RdTh source.

(ii) Set neutron linear TSCA lower level to just below ^{22}Na annihilation Compton edge, and upper level to eliminate overload pulses from a PoBe source.

(iii) Set neutron shape DDL amplifier gain to just not overload on pulses from a PoBe neutron source.

(iv) Set neutron shape TSCA discriminator to just exclude gamma pulses from a RdTh source.

(v) Examining the spectrum of the TAC output on a kicksorter, the neutron shape and linear TSCA discriminators could now be lowered until gamma pulses from a RdTh source nearly entered the neutron pulse region as determined with a PoBe source.

(vi) Setting an SCA on the TAC output, and using this to gate the neutron linear signal in a kicksorter, the neutron threshold detection energy could be determined using a PoBe source and table 2.2A.

In this way the optimum EHT for the photomultiplier was determined to be 2150 volts, which value was used for all subsequent runs. Optimum performance depended critically on the shape potentiometer setting (i.e., last dynode-anode

voltage control: fig. 2.2B). This was conveniently monitored by observing PoBe pulses from the shape output on an oscilloscope triggered from the linear TSCA output. When experience was gained it was a straightforward procedure to set the PSD circuits to admit PoBe source neutrons of energy above $\sim$ 1 MeV, whilst rejecting RdTh gamma rays by a factor of 200 : 1 for a count rate of 10^5 c/s in the linear TSCA.

On one occasion the response to neutrons was checked using the $Li^7(p,n)Be^7$ reaction, the yield of which is approximately independent of proton energy at 90° (lab.), (Bo 63). The neutron count rate (normalised to beam) increased linearly from zero at E_n = 0.9 MeV and levelled off at E_n $\sim$ 2 MeV, in good agreement with the PoBe source results.

A refinement was to interpose a 2.5 cm thick lead sheet in front of the neutron detector. This reduced the gamma count rate by $\sim$ 80%, while only reducing the neutron rate by $\sim$ 15%, thus giving a further four-fold improvement in gamma rejection.

Typical TAC output spectra for an Americium-Beryllium neutron source and for a mixed gamma source are shown in fig. 2.2D. The Am-Be source gives neutrons up to $\sim$ 10 MeV

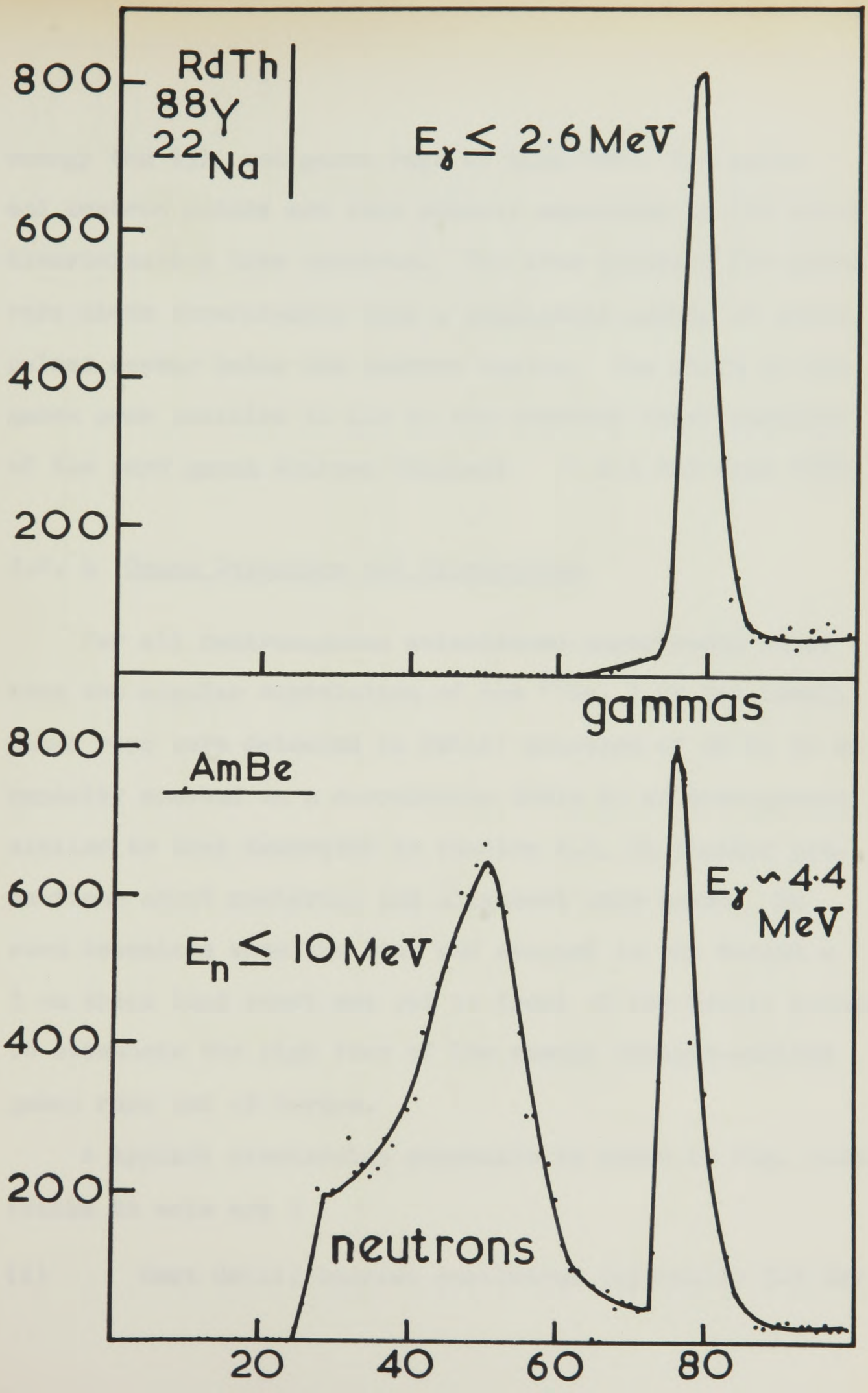

800
600
400
200
RdTh
88Y
22Na
Eγ ≤ 2·6 MeV
gammas
800
600
400
200
AmBe
En ≤ 10 MeV
Eγ ~ 4·4 MeV
neutrons
20
40
60
80

Figure 2·2D

energy (Ma 63), and gamma rays of 4.44 MeV. The gamma and neutron pulses are very clearly separated in the shape discrimination time spectrum. The time spectrum for gamma rays alone shows clearly that a negligible number of gamma pulses appear below the neutron region. The shift in the gamma peak position is due to the somewhat lower energies of the pure gamma sources (highest $\sim$ 2.6 MeV from RdTh).

2.2. 4 Gamma Detectors and Electronics

For all neutron-gamma coincidence experiments other than the angular correlation of the ^{18}Ne, 1.89 MeV level, gamma rays were detected in Ge(Li) counters of 35 to 50 cc capacity mounted on a correlation table in an arrangement similar to that described in section 2.1. 1; similar precautions about centering and alignment were taken. On some occasions when the beam was stopped in the target a 3 mm thick lead sheet was put in front of the Ge(Li) counters to attenuate the high flux of low energy Coulomb-excited gamma rays and of X-rays.

A typical electronics schematic is shown in fig. 2.2E. Points to note are :

(i) Best Ge(Li) counter resolution (typically 7-9 keV

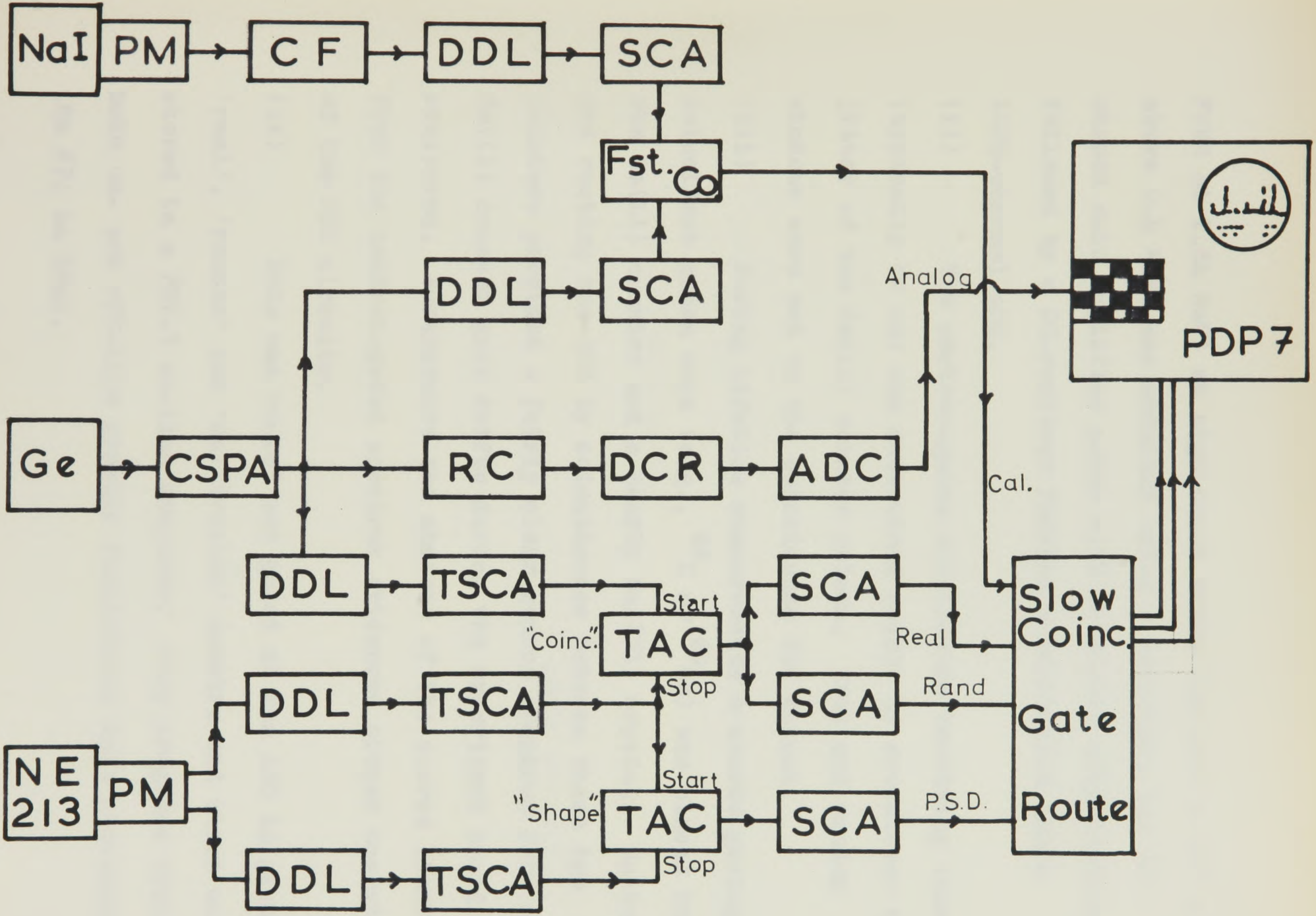

NaI
PM
C F
DDL
SCA
Fst. Co
DDL
SCA
Analog
PDP 7
Ge
CSPA
R C
DCR
ADC
Cal.
DDL
TSCA
Start
"Coinc"
TAC
SCA
Real
Slow Coinc
DDL
TSCA
Stop
SCA
Rand
Gate
NE 213
PM
Start
"Shape"
TAC
SCA
P.S.D.
Route
DDL
TSCA
Stop

Figure 2·2E

FWHM at 1.84 MeV) at high count rates (up to 2×10^4 c/s above 0.4 MeV) was obtained using a unipolar, 1μs RC-shaped main amplifier pulse with pole-zero compensation, followed by a DC-restorer feeding a DC-coupled Laben 1024-channel ADC.

(ii) The neutron-gamma coincidence resolving time (typically 80 ns) was determined mainly by cross-over time jitter of the Ge(Li) counter pulses. Real and random windows were set on the coincidence TAC output.

(iii) During lifetime measurements a source giving coincident gamma rays (e.g., ^{88}Y or ^{60}Co) was placed between the Ge(Li) counter and a nearby NaI(Tl) crystal. Gating and routing the ADC by coincidences between these two counters provided a fairly clear source spectrum from which Ge(Li) counter gain drifts during the experiment could be monitored. Furthermore the absence of the source lines from the neutron-gated spectrum evidenced proper operation of the PSD circuits.

(iv) Data was routed and gated at the ADC to give 'real', 'random' and 'calibration' spectra and these were stored in a PDP-7 on-line computer. Many programs available both on- and off-line greatly facilitated data processing (Mu 67; La 68a).

' "No, no!" said the Queen. "Sentence first-

verdict afterwards." '

Lewis Carroll.

C H A P T E R 3

ELECTROMAGNETIC FORMULAE AND DATA ANALYSIS

3.1 Electromagnetic Transition Formulae

(Matrix Elements and Angular Distributions).

The formulae quoted here are taken directly from the phase consistent treatment of Rose and Brink (Ro 67). In any such treatment points arise at which a choice of phase has to be made for various quantities (e.g., wave-functions, tensor operators, EM vector potentials). In treatments which only aim at presenting formulae for correlation analysis these choices have generally been made rather arbitrarily as they are less restricted than in a full treatment aiming to produce a set of matrix elements unambiguously related to nuclear model calculations as well as to the correlation formulae. Worse, as many authors do not explicitly state their choices great difficulty has arisen in comparing mixing ratio phases obtained using different treatments of the various correlation geometries. Further confusion has arisen over the explicit definition of E.M. operators, with absorption operators used in some cases, and emission ones in others; so that, for instance, the

phase of a mixing ratio may depend on whether it is measured as the first or second member of a gamma cascade, or as a particle-gamma correlation. Similar difficulties arise when comparing nuclear model calculations of mixing ratios with measurements.

In the Rose and Brink treatment one starts from first order perturbation theory and calculates the electromagnetic absorption process. "Time reversal invariance" is then used to uniquely relate this absorption process to the emission process. The electromagnetic vector potentials used are terms of a consistent expansion of a plane circularly polarised wave which interacts with the nucleus. This leads to a set of interaction multipole operators which are terms of an expansion of a well-defined interaction Hamiltonian; the operators themselves are explicitly defined and have definite Hermitian and time-reversal properties. Using this set of operators T^{π}_{LM} and consistently writing matrix elements in the form $\langle \text{initial} \mid T^{\pi}_{LM} \mid \text{final} \rangle$, the angular distribution formulae are derived in terms of the reduced matrix elements of T^{π}_{L}. These also have well-defined phases and are calculable from nuclear models.

An alternative treatment, which leads to the same conclusions, is to start from field theory and calculate

the emission process directly (Ro 67; Gr 68; St 68).

The definitions of the interaction multipole operators are (in the notation of (Ro 67)) :

$$T^e_{LM} = a^e_L G^e_{LM} \qquad T^m_{LM} = a^m_L G^m_{LM}$$

where $ia^m_L = a^e_L = (ik)^L (1 + 1/2L)^{\frac{1}{2}} ((2L+1)!!)^{-1}$

and the G_{LM} are the multipole operators

$$G^e_{LM} = Q_{LM} + Q'_{LM} \qquad G^m_{LM} = M_{LM} + M'_{LM}$$

where (3.1a)

$$Q_{LM} = 2g_\ell (m\beta/\hbar^2 k) [H, r^L C_{LM}]$$

$$Q'_{LM} = - g_s \beta [k/(L+1)] \underset{\sim}{L} (r^L C_{LM}) \cdot \underset{\sim}{s}$$

$$M_{LM} = 2g_\ell \beta (L+1)^{-1} \nabla (r^L C_{LM}) \cdot \underset{\sim}{\ell}$$

$$M'_{LM} = g_s \beta \nabla (r^L C_{LM}) \cdot \underset{\sim}{s}$$

Here $\beta = e\hbar/2mc$ is the nuclear magneton; $g_\ell = 1$ for a proton, 0 for a neutron; $g_s = 5.586$ for a proton, -3.826 for a neutron; the symbol H which appears in the definition of Q_{LM} is the Hamiltonian of the nuclear system.

The T_{LM} are single particle operators. Reduction of matrix elements between nuclear states to sums over single

particle elements may be performed either using successive fractional parentage expansion of the initial states, or by second quantization techniques; in the latter method particle-hole descriptions of levels can also be conveniently treated in a phase-consistent manner. Explicit formulae for the various components of the reduced single particle matrix elements are (Ro 67):

$$\langle \ell_1 j_1 \| (Q_L)_{\text{eff}} \| \ell_2 j_2 \rangle = e g_\ell I(L) b_{12}$$

$$\langle \ell_1 j_1 \| Q'_L \| \ell_2 j_2 \rangle = \tfrac{1}{2} g_s \beta k \, I(L)(a_1 - a_2) b_{12}/(L+1)$$

$$\langle \ell_1 j_1 \| M_L \| \ell_2 j_2 \rangle = 2\beta g_\ell \, i^{\ell_1 - \ell_2} (-)^{j_1 + \frac{1}{2}} I(L-1)$$

$$\times \, (\ell_1 0 \ell_2 1 / L1) W(j_1 \ell_1 j_2 \ell_2; \tfrac{1}{2} L) \hat{j}_2 \hat{\ell}_1 \hat{\ell}_2$$

$$\times \sqrt{L \, \ell_2 (\ell_2 + 1)/(L+1)(2L+1)}$$

$$\langle \ell_1 j_1 \| M'_L \| \ell_2 j_2 \rangle = \tfrac{1}{2} g_s \beta I(L-1) . (L - a_1 - a_2) b_{12} \qquad (3.1b)$$

where I(L) is the radial integral

$$I(L) = \int u_1 (r) \, r^{L+2} \, u_2 (r) \, dr$$

and

$$b_{12} = i^{\ell_1 - \ell_2} (-)^{j_1 - \frac{1}{2}} \frac{\hat{j}_2}{\hat{L}} (j_1 \tfrac{1}{2} j_2 - \tfrac{1}{2} / L 0)$$

and

$$a_1 = (\ell_1 - j_1) \hat{j}_1$$

and

$$\hat{L} = (2L+1)^{\frac{1}{2}} \text{ etc.}$$

The general angular distribution for the emission of photons of circular polarization q and wave-vector $\underset{\sim}{k}$ from an ensemble of nuclei $\sum_{M_1} w(M_1) . |J_1\ M_1\rangle$ having an axis of symmetry (taken as the quantisation axis) decaying to a state $|J_2\rangle$ (of which the final orientation is not observed) is then (Ro 67) obtained in terms of these multipole operators:

$$W^q(\underset{\sim}{k}) = \frac{k}{2\pi\hbar} \sum_{\substack{KLL' \\ \pi\pi'}} B_K(J_1) F_K(\cos\theta) (-)^{q+J_1-J_2+L'-L-K} \hat{J}_1$$

$$\times (LqL'-q \mid KO) W(J_1 J_1 LL'; KJ_2) q^{\pi+\pi'} \qquad (3.1c)$$

$$\langle J_1 \| T_L^{\pi} \| J_2 \rangle \langle J_1 \| T_{L'}^{\pi'} \| J_2 \rangle^*$$

where $$B_K(J_1) = \sum_{M_1} w(M_1) (-)^{J_1-M_1} \hat{J}_1 (J_1 M_1 J_1 -M_1 \mid KO) \qquad (3.1d)$$

with $$B_0(J_1) = 1, \quad \sum_{M_1} w(M_1) = 1,$$

π, π' = 0 for electric, 1 for magnetic transitions, and L, L' are the E.M. transition multipolarities.

In the particular case of particle-gamma correlations of the type studied in this work, where the emergent particles

are detected on the beam axis, and where the incident beam and target are unpolarised, we have alignment of the ensemble of $|J_1\rangle$: i.e., $w(M_1) = w(-M_1)$. It is then convenient to write $B_K(J_1)$ in the form

$$B_K(J_1) = \sum_{M_1=0 \text{ or } \frac{1}{2}}^{J_1} w(M_1)\, \rho_K(J_1 M_1) \qquad (3.1e)$$

where

$$\rho_K(J_1 M_1) = (2-\delta_{0,M_1})(-)^{J_1-M_1}\, \hat{J}_1 (J_1 M_1 J_1 -M_1 \mid K0).$$

Furthermore the initial and final states have definite parity, one normally expects only the two lowest multipolarities to contribute, and gamma polarisation is not observed. The general correlation formula then reduces to a sum over even values of k only :

$$W(\theta) = \frac{\sum B_k(J_1)[R_k(LLJ_1J_2) + 2\delta R_k(LL'J_1J_2) + \delta^2 R_k(L'L'J_1J_2)] P_k(\cos\theta)}{1+\delta^2} \qquad (3.1f)$$

where $R_k(LL'J_1J_2) = (-)^{1+J_1-J_2+L'-L-k}\, \hat{J}_1 \hat{L} \hat{L}'$

$$\times (L\,1\,L'-1 \mid k0)\, W(J_1J_1LL';kJ_2) \qquad (3.1g)$$

and where the multipole mixing ratio δ is given by

$$\delta = \frac{\hat{L}}{\hat{L}'} \cdot \frac{\langle J_1 \| T^{\pi'}_{L'} \| J_2 \rangle}{\langle J_1 \| T^{\pi}_{L} \| J_2 \rangle} \qquad (3.1h)$$

and $L' = L + 1$ (normally).

If the initial state $|J_1\rangle$ is followed by a series of cascade gamma rays, and one observed not the first but the n^{th} of these, then the nuclear alignment parameter $B_k(J_1)$ must be replaced by

$$B_k(J_1) \times \prod_{i=1}^{n-1} U_k(J_i J_{i+1})$$

where

$$U_k(J_1 J_2) = \frac{\sum_{L_{12}\,\pi_{12}} \left| {}^{\pi_{12}}\delta_{L_{12}} \right|^2 U_k(L_{12} J_1 J_2)}{\sum_{L_{12}\,\pi_{12}} \left| {}^{\pi_{12}}\delta_{L_{12}} \right|^2} \qquad (3.1i)$$

and

$$U_k(L_{12} J_1 J_2) = (-)^k \frac{W(J_1 J_1 J_2 J_2; k L_{12})}{W(J_1 J_1 J_2 J_2; 0 L_{12})}$$

The coefficients $R_K(LL'J_1J_2)$, $\rho_K(J_1M_1)$ and $U_K(L_{12}J_1J_2)$ have been tabulated (Ha 66; Ro 67).

An important feature of equation 3.1f is that it factors into two terms, one of which (B_k) contains all the information about the mode of formation of the state (i.e., the population parameters), and the other of which ($\sum$ R_k x powers of δ) contains all the nuclear structure information of the transition (i.e., the mixing ratios). Thus when analysing experimental results the number of unknowns is somewhat reduced since the same B_k apply to all branches from a given state.

An extensive suite of computer programs (Ha 66) based on the above treatment was available at Oxford for angular correlation analysis and matrix element computation, and was of great convenience to the present writer.

3.2 Angular Correlation Analysis

3.2.1 Substate Population; Finite Size Effects

In perfect geometry, with particles incident on a target at 0°, and with emergent particles detected only at 0° or 180°, then clearly the orbital angular momenta of incident and emergent particles have zero projection on the beam axis: classically, since $\underset{\sim}{\ell} = \underset{\sim}{r} \times \underset{\sim}{p}$, then $\underset{\sim}{\ell} \cdot \underset{\sim}{p} = 0$. If this axis is taken for quantisation, it is apparent that the population parameters $w(M_1)$ of the produced nuclear

state $|J_1\rangle$ can only be non-zero for

$$|M_1| \leqslant M_{max} = S_i + S_t + S_e \qquad (3.2a)$$

where S_i, S_t, S_e are the spins of the incident, target, and emergent (detected) particles.

For instance in the $^{12}C(t,\alpha)$ reaction we only populate $M_1 = \pm \frac{1}{2}$ magnetic sublevels of ^{11}B, but in the $^{12}C(t,p)^{14}C$ reaction we populate both $M_1 = 0$, and $M_1 = \pm 1$ magnetic sublevels of ^{14}C. It is this restriction which is the power of the particle-gamma correlation technique: clearly it is desirable to study reactions where S_i, S_t, and S_e are all as low as possible.

Both the solid state annular counter and the neutron counter typically subtended $\theta_{LAB.} = \pm 10^{\circ}$ from the beam axis, so that it was possible to populate higher magnetic substates than allowed by equation 3.2a. The most important of these is $W(M_{max} + 1)$. It can be shown in various ways (Li 61; Po 64; Gi 68) that for small angles θ_{CM} (in radians)

$$W(M_{max} + 1) = C_{reaction} \cdot \theta_{CM}^2 \qquad (3.2b)$$

where $C_{reaction}$ depends on the detailed reaction mechanism

and though cases arise where it can be principle be evaluated, the calculation is exceedingly tedious. Approximations show however that $C_{reaction}$ is unlikely to be of order greater than unity (Po 64; Gi 68) and so $w(M_{max} + 1)$ will not normally exceed a few percent. The effect may be tested experimentally by observing the effect on the gamma ray correlation of changing θ (i.e., changing the particle counter distance). Or, during the correlation analysis, one can readily check the effect of including say 3% population of the $M_{max} + 1$ substate: it is generally not found to be critical (cf. sections 4.2. 2; 5.2. 2).

The effect of the finite size of the gamma detector can be dealt with precisely. Using a method due to Rose (Ro 53) it may be shown that for cylindrical γ detectors a true gamma ray angular distribution

$$W(\theta) = \sum_{n=0} A_n P_n (\cos\theta) \qquad (3.2c)$$

will be observed as

$$W(\theta) = \sum_{n=0} A_n Q_n P_n (\cos\theta) \qquad (3.2d)$$

where Q_n are the gamma distribution attenuation factors

defined by

$$Q_n = \frac{J_n}{J_o} \qquad (3.2e)$$

where $J_n = \int_o^\pi \epsilon(\psi) P_n(\cos\psi) \sin\psi \, d\psi$.

In this integral, $\epsilon(\psi)$ is the efficiency of the counter for a gamma ray propagating at an angle ψ to the counter axis.

Tables of Q_n for NaI(Tl) counters (Ru 59) and for Ge(Li) counters (Ha 66) were used.

3.2. 2 Data Reduction; Legendre Fits

Angular correlations for the (t,p) and (t,α) experiments were taken using NaI(Tl) counters. (Because only even-order Legendre polynomials enter equation 3.1e it was in general only necessary to measure the correlation in one quadrant: which was, in general, dependent on considerations of geometrical convenience.) All spectra from a particular gamma counter in coincidence with the particle group from a particular final-nucleus level were added together (after subtraction of randoms) and then stripped into component

gamma rays using suitable gamma source line-shapes obtained with the same counters, and supplemented by the published line-shapes of Jarczyk et al. (Ja 62).

When the gamma rays present had thus been established it was possible to strip the individual correlation spectra to obtain the angular correlation of each gamma ray (normalised to particle window counts). Errors on the points of these correlations arise both from counting statistics and from uncertainties in the line-shapes used to strip the spectra.

Least squares fits of Legendre polynomials to the observed distributions (Ha 66) gave the attenuated Legendre coefficients $A_n Q_n$ of equation 3.2d, and their errors, from which the true coefficients A_n could be determined. It is always these latter corrected values which are quoted in this work.

Decay branching ratios were obtained from the normalisations (A_o) of the individual Legendre fits using the photopeak efficiencies of Jarczyk et al. (Ja 62). For the 13 cm x 15 cm crystal these efficiencies had to be deduced from the data of (Ja 62) given for a 13 x 10 cm crystal. The extrapolation was performed assuming a constant photopeak-to-total ratio at a given energy and then

correcting for the different total efficiencies of the two crystals at this energy.

The procedure adopted to analyse the results of n-γ coincidence experiments was in most respects similar. Stripping and identification of gamma rays present was greatly simplified by the superior Ge(Li) counter resolution. Correlations and branching ratios were based only on photopeak counts: these were extracted by extrapolating observed background linearly beneath the peak (cf. section 3.3. 5). The Ge(Li) counter photopeak efficiencies of (An 68) and (La 67) were used.

For all angular correlations, measurement at each angle was repeated at least once, and in the case of disagreement, yet again. Monitoring of particle window rates, total particle (or neutron) and gamma rates, integrated beam current, etc. normally enabled one to trace the cause of any disagreement (e.g., channel setting drift, gain changes, or target deterioration). Corrective action would be taken and the erroneous correlation run discarded.

3.2. 3 Spin and Mixing Ratio Determination

From section 3.1 it is evident that the observed Legendre coefficients of an angular distribution are:

$$A_K Q_K = Q_K B_K(J_1) \frac{R_K(LLJ_1J_2) + 2\delta R_K(LL'J_1J_2) + \delta^2 R_K(L'L'J_1J_2)}{1+\delta^2} \qquad (3.2f)$$

In simple cases (e.g., if J_1 and J_2 are known, and if there is at most one free population parameter) it is often possible to determine δ directly from this equation. More generally however it is necessary to seek solutions over a range of J_1, J_2, δ and $w(M_1)$, and this is done using least squares fitting computer programs (Ha 66).

One computes

$$\frac{\chi^2}{\nu} = \frac{1}{\nu} \sum_i \left(\frac{Y(\theta_i) - N \sum_K A_K Q_K P_K(\cos\theta_i)}{E(\theta_i)} \right)^2 \qquad (3.2g)$$

where θ_i are the correlation angles, Y and E are yield and error of the gamma distribution, $A_K Q_K$ are computed from equation 3.2f, N is a normalisation constant, and ν is the number of degrees of freedom (= number of measurements less number of linearly optimised parameters such as N, $w(M_1)$, etc.).

χ^2 is quadratic in N and in the $w(M_1)$ so that these may be automatically optimised by requiring

$$\frac{\partial^2 (\chi^2)}{\partial N^2} = 0 \quad \text{or} \quad \frac{\partial^2 (\chi^2)}{\partial w^2} = 0 \quad \text{etc.}$$

If the $w(M_1)$ are optimised in this way one must include the conditions $0 \leqslant 2w(M_1) \leqslant 1 + \delta_{0,M_1}$: $\Sigma\, w(M_1) = 1$.

N was always optimised by the program.

The dependence of χ^2 on J_1, J_2 and δ is more complex (i.e., A_K is not a linear function of these variables) and the procedure adopted is to map χ^2/ν for $-\infty \leqslant \delta \leqslant \infty$ in convenient steps of δ, and for all reasonable values of J_1 and J_2. If the $w(M_1)$ are not optimised automatically then χ^2/ν is also mapped against these. If only the first two magnetic substates are populated it is convenient to define a population parameter p such that

$$w(M) = \frac{p}{2-\delta_{0,M}} \qquad \text{and} \qquad w(M+1) = \frac{1-p}{2}$$

where $M = 0$ or $\frac{1}{2}$, and $0 \leqslant p \leqslant 1$.

The value of χ^2/ν obtained for any combination of the parameters J_1, J_2, δ, p is a measure of the "goodness of fit" of the predicted to the observed correlation. For the true values of these parameters the expectation of χ^2/ν is unity. Larger values imply a poor fit.

Confidence limits on χ^2/ν as a function of ν are widely tabulated (e.g., (Wa 59)). In all the cases considered here, the final spin J_2 was known. If for a given initial spin J_1 no values of δ (or p, when variable) gave χ^2/ν less than that which corresponded to a certain confidence limit (usually 1%) then that initial spin value was considered excluded. χ^2/ν is the ratio of two quartics in δ. For each of the permitted initial spins J_1, it was usual to obtain two minima of χ^2/ν corresponding to "best" values of δ. These are the values quoted later. The question of how properly to assign an error to δ when it has been determined from a non-linear least squares fit of the above type has in the past been somewhat confused.

The Legendre fit errors on A_2 or A_4 are correct since the χ^2 fitting procedure in this case is linear. Some workers (Gi 68; Lo 67) substitute these into the correlation formula (3.2f) to estimate the errors on δ. This method is strictly proper only when the population is predetermined and when only one Legendre coefficient is sensitive to δ. Otherwise it ignores both the interplay of information on δ between the various Legendre coefficients, and also the ability of changes in population parameter to compensate for changes in δ.

It is clear that the depth of the minimum of the non-linear χ^2-fitting of the distribution to δ and p (i.e., the quality of the "best" fit) and the width (or "sharpness") of the minimum must reflect the precision with which δ is determined. On this basis some workers (e.g., An 68a) took errors on the mixing ratio δ from the points at which χ^2 rose to $4/3$ of its minimum value χ^2_{min}, reasoning (incorrectly) that this should correspond to $\pm$ 1 standard deviation by analogy with the Gaussian probability distribution; others (e.g., St 68) took errors as the points at which the probability of exceeding the χ^2 value fell to half the probability of exceeding χ^2_{min}; yet other methods have also been used (Br 63; Gl 63; Po 65). None of these is rigorously correct - for instance proper account is not taken of the number of independent degrees of freedom, which clearly influences the accuracy of determination of δ.

Recently Archer et al. (Ar 66) have shown that if $\delta = \delta_0$ corresponds to a minimum $\chi^2 = \chi^2_{min}$, then the values of δ for which $\chi^2 = \chi^2_{min}\,(1 + \frac{1}{\nu})$ correspond to $\pm$ one standard deviation away from δ_0. This statement is true if the minimum of χ^2 is sufficiently sharp that the theoretical correlation is <u>locally</u> a linear function of δ, i.e., the minimum must be parabolic in shape. Even if this

is not precisely so, one would still expect to obtain a good indication of the precision of δ_o.

One point arises regarding the interpretation of in these formulae. To evaluate the significance of the minima of χ^2, (i.e., "goodness of the fit"), then ν is as defined above:

i.e., ν = No. of measurements - No. of fitted parameters.

But clearly no number of measurements at a single angle alone will determine dependence on δ of the distribution and so we define

ν_e = No. of separate angles - No. of fitted parameters

and take the errors on δ from the points at which

$$\chi^2 = \chi^2_{min} \times \left(1 + \frac{1}{\nu_e}\right).$$

This procedure has been followed in the present work. In a check, it was found to give substantially the same errors on δ as those derived from equation (3.2f) and the measured A_2 for the specific case of the ^{11}B, 4.44 MeV $\rightarrow$ g.s. correlation where p = 1 and $A_4 = 0$ (since $J_{4.44} = 3/2$).

3.3 Doppler Shift Attenuation Lifetime Measurement

3.3. 1 Basic Principles

In many reactions, the final nucleus has a recoil velocity (v) which is an appreciable fraction of the speed of light (c). Thus $\beta = v/c$ is typically in the range 0.3% to 5%. Under this condition, gamma rays observed to be emitted from the nucleus will be subject to a Doppler shift in their energy. If E_γ is the normal (stationary source) gamma energy, and if ψ is the angle between the direction of travel of the nucleus and the direction of emission of the gamma ray, then

$$E_{obs} = E_\gamma + E_{DS} = E_\gamma (1 + \beta \cos \psi) \qquad (3.3a)$$

and for usual values of β no relativistic corrections are necessary. In a typical case $E_\gamma \sim 2$ MeV, $\beta \sim 1\%$, so that $E_{DS} \sim 20$ keV. A change in energy of this magnitude is well within the measurement capability of presently available Ge(Li) detectors.

Further, let us now suppose the nucleus to have been formed in a solid medium, so that it will be subject to a rapid slowing down. If the nuclear level mean life (τ) is

very short compared to some (yet to be) conveniently defined slowing down time, a, then all gamma rays will be emitted while β has its maximum value, and so

$$E_{DS} = E_\gamma \cdot \beta_{max} \cdot \cos\psi \qquad (\tau \ll a) \qquad (3.3b)$$

On the other hand if the lifetime is long, then all recoiling nuclei will have come to rest before gamma emission - no Doppler shift will be observed

$$E_{DS} = 0 \qquad (\tau \gg a) \qquad (3.3c)$$

Clearly the intermediate situation, where τ and a are comparable, provides a means of measuring the mean lifetimes of nuclear energy levels.

It is now appropriate to define the Doppler shift attenuation factor $F(\tau)$ such that

$$E_{DS} = E_\gamma \cdot \beta_{max} \cdot \cos\psi \cdot F(\tau) \qquad (3.3d)$$

Clearly $0 \leq F(\tau) \leq 1$ where the extremes correspond to $\tau = \infty$ and 0 respectively. The measurement of τ now separates into two parts (i) E_{DS}, E_γ, and $\cos\psi$ are

measured during an experiment, and β_{max} may be calculated from the reaction kinematics. (ii) The $F(\tau)$ value determined from step (i) must be related to τ by calculations based on known stopping process mechanisms. Part (i) will be discussed under the individual experiments; part (ii) will be considered in the next section.

3.3. 2 Stopping Processes and $F(\tau)$ calculations

Firstly let us recollect two useful results:

(A) The number of nuclei decaying from an initial number N_o, at time t after formation, is given by

$$dN = -d(N_o e^{-t/\tau}) = \frac{N_o}{\tau} \cdot e^{-t/\tau} \cdot dt = N \cdot \frac{dt}{\tau} \qquad (3.3e)$$

where τ is the mean life of the level.

(B) The mean Doppler shift observed when a collection of nuclei with velocities $\underset{\sim}{v}_i$ emit gamma rays with wave vector $\underset{\sim}{k}$ to a gamma detector is $\langle \hbar \underset{\sim}{k} \cdot \underset{\sim}{v}_i \rangle$. In a typical experiment the distribution of $\underset{\sim}{v}_i$ is symmetric with respect to the beam direction. Taking this as the z-axis both for Cartesian and spherical polar coordinate systems, and with an obvious notation,

$$\underset{\sim}{k} = k\ (0, \sin\theta_\gamma, \cos\theta_\gamma)$$

$$\underset{\sim}{v}_i = v_i\ (\sin\theta_i\cos\phi_i, \sin\theta_i\sin\phi_i, \cos\theta_i)$$

so that

$$\left\langle \hbar \underset{\sim}{k}\cdot\underset{\sim}{v}_i \right\rangle = \frac{E_\gamma}{c} \left\langle v_i(\sin\theta_\gamma\sin\theta_i\sin\phi_i + \cos\theta_\gamma\cos\theta_i) \right\rangle$$

$$= \frac{E_\gamma}{c} \cdot \cos\theta_\gamma \cdot \left\langle v_i\cdot\cos\theta_i \right\rangle \qquad (3.3f)$$

since $\left\langle v_i \sin\theta_i \sin\phi_i \right\rangle = 0$ by the axial symmetry.

Whilst an ion is slowing down it is influenced by two distinct processes, viz. multiple small angle scattering by electrons, and large angle scattering by atoms as a whole. At high velocities ($> 10^8$ cm/s) the moving nucleus is heavily ionized and frequently gains and loses electrons by interaction with passing atoms. Momentum transfers are small but frequent, resulting in a steady deceleration with insignificant net change in direction. Calculations for this electronic stopping process (Fi 59; Li 63) predict

$$\frac{dE}{dx} \propto E^{\frac{1}{2}} \propto v \qquad (3.3g)$$

provided $v < \frac{e^2}{\hbar} \cdot Z_{ion}^{2/3}$, $\sim 1.5 \times 10^9$ cm/s for ^{26}Si.

Experimental results suggest a similar law of the form

$$\frac{dE}{dx} \propto v^r \qquad (3.3h)$$

where r is different for various combinations of ion and stopper, but is typically in the range 0.8 → 1.0 (Wi 62; Or 63).

At lower velocities the ion is moving more slowly than the electrons in the outer orbitals of the stopping atoms. It is then normally neutral and can only lose energy by elastic collisions with the stopping atoms. These have a mass comparable to that of the moving nucleus, so that momentum transfers and direction changes are large. The latter attenuate rapidly the velocity component in the original direction of motion. Lindhard et al. (Lin 63) have published theoretical estimates of the electronic and nuclear stopping effects. These are quoted in terms of dimensionless range and energy parameters:

$$\rho = \frac{165\ A_1\ D}{(A_1+A_s)^2} \cdot R$$

$$\epsilon = \frac{32{,}520\ A_s}{Z_1 Z_s Z (A_1+A_s)} \cdot E$$

where $$Z^{2/3} = Z_1^{2/3} + Z_s^{2/3} \qquad (3.3i)$$

and R = range of ion in $\mu gm/cm^2$

E = ion energy in MeV

Z_i, Z_s = atomic number of ion, stopper

A_i, A_s = mass of ion, stopper in a.m.u.

D = density of stopper in gm/cc.

Then the electronic stopping power is

$$\left(\frac{d\epsilon}{d\rho}\right)_e = \frac{0.0793 \; Z_i^{2/3} \; Z_s^{1/2} \; (A_i+A_s)^{3/2}}{Z^{1/2} \cdot A_i^{3/2} \cdot A_s^{1/2}} \; \epsilon^{1/2} \qquad (3.3j)$$

Theoretical universal differential scattering and stopping cross-sections for quasi-elastic nuclear collisions have been calculated by Lindhard et al. for a Thomas-Fermi model of the colliding atoms. These universal cross-sections are presented in ρ- ϵ parameterisation as figures 1 and 2 of (Lin 63). It is a simple matter to fit those curves with empirical expressions to an accuracy adequate for computer calculations.

Combining equations (3.3d,e,f) we now obtain

$$F(\tau) = \int_0^\infty \frac{1}{v_o \cdot \tau} \cdot e^{-(t/\tau)} \left\langle v_i \cos\theta_i \right\rangle_t \; dt \qquad (3.3k)$$

where $v_o = \left\langle v_i \cdot \cos\theta_i \right\rangle_{t=0}$. Strictly, since energy

loss and direction change due to nuclear scattering are correlated, one should calculate $\langle v_i \cdot \cos\theta_i \rangle_t$ as a function of time. This turns out to be a difficult task and it is usual to make the approximations:

$$\langle v_i \cdot \cos\theta_i \rangle_t = \langle v_i \rangle_t \cdot \langle \cos\theta_i \rangle_t$$

$$\langle v_i \cdot \cos\theta_i \rangle_{t=0} = v_o$$

$$\langle \cos\theta_i \rangle_{t=0} = 1. \qquad (3.31)$$

The latter two approximations are justified by the observation that for most lifetime experiments the reaction kinematics restrict the recoiling nuclei to a narrow velocity range and angular spread. With these simplifications $\langle v_i \rangle_t$ is readily computed from the velocity-time curve obtained by numerical integration of

$$t = -\int_{v_o}^{v_i} \frac{m_i \, dv_i}{(\frac{dE}{dx})_e + (\frac{dE}{dx})_n} \qquad (3.3m)$$

where m_i is the ion mass, $(\frac{dE}{dx})_e$ is calculated from equations (3.3i,j), and $(\frac{dE}{dx})_n$ from equations (3.3i) and fig. 2 of (Lin 63).

Similarly $\langle \cos\theta_i \rangle_t$ may be computed by numerical integration of Lewis's relationships (Le 50):

$$\langle \cos\theta_i \rangle_t = \exp\left(-\int_0^x K(\theta_i)dx\right)$$

and

$$K(\theta_i) = N \oint_{\theta_i} (1-\cos\theta_i)d\sigma(\theta_i) \qquad (3.3n)$$

where N is the number of scattering centres per cc, $\sigma(\theta_i)$ is the laboratory system differential scattering cross-section, and x is the distance traversed in the stopping medium. The first integral can be rewritten in a form suitable for numerical integration:

$$\int_0^x K(\theta_i)dx = \int_{V_0}^{V_i} \frac{K(\theta_i)\, m_i v_i\, dv_i}{\left(\frac{dE}{dx}\right)_e + \left(\frac{dE}{dx}\right)_n} \qquad (3.3o)$$

Converting to the centre of mass system and writing $r = A_i/A_s$ one obtains also

$$K(\theta_i) = 2\pi N \int_0^{\pi} \left[1 - \frac{r + \cos a}{\sqrt{1+r^2 + 2r\cos a}} \right] \sigma(a)\sin a\, da \qquad (3.3p)$$

in which the differential scattering cross-section of fig. 1,

ref. (Lin 63) can be used. (An alternative treatment of the $\langle \cos\theta_i \rangle$ evaluation is given by Blaugrund (Bl 66)).

The equations of this subsection form the basis of a computer algorithm due to R.D. Gill which computes $F(\tau)$ values on the basis of the Lindhard $\frac{dE}{dx}$ predictions, and which was used in a slightly modified form for the analysis of the ^{26}Si lifetime measurements described in Chapter 5.

A final note: it is convenient often to consider only the effect of electronic stopping on $F(\tau)$ according to equation (3.3g). It is then a simple matter to derive $F(\tau)$ analytically:

$$F(\tau) = \frac{a}{a + \tau}$$

where
$$a = \left| \frac{m_i v_i}{\left(\frac{dE}{dx}\right)_e} \right| \qquad (3.3q)$$

The (velocity-independent) constant a is known as the "characteristic slowing down time" for the given ion in the given medium (Lin 63). For combinations of ion and stopper encountered experimentally, a usually lies in the range 0.3 to 3 picoseconds.

3.3. 3 $F(\gamma)$ Accuracy and Corrections

Many assumptions and approximations have been made in the preceding subsection in order to obtain tractable formulae for computation. Among the more important of these are:

(i) Retaining equations (3.3g) and (3.3j) for $(dE/dx)_e$ inspite of the known form (3.3h).

(ii) Ignoring correlations between nuclear energy loss and scattering angle by the approximations equations (3.31). Unhappily this correlation might be expected to be worst for just the case in which we are interested, where ion and stopper have similar masses.

(iii) Lindhard, Scharff and Schiøtt (Lin 63) make many approximations in deriving their electronic and nuclear stopping formulae. Thus correlations between electronic and nuclear energy loss are ignored although considerable ionization will occur in close collisions. Likewise the nuclear collisions are only quasi-elastic and cannot in detail be described by a potential between two heavy centres.

(iv) It is virtually impossible to directly verify the nuclear stopping formula of (Lin 63) in solids because of the low ion energies involved, the intrinsic importance of large

angle scattering, and the ever-present electronic stopping contribution.

It was therefore desirable to test these assumptions. Electronic stopping power measurements are sparse for low velocity ions ($\leqslant 2.10^8$ cm/s) such as those encountered in the ^{26}Si experiment. None could be found for the case of Si in Mg. The most similar data are those of Ormrod et al. (Or 65) who found that the electronic stopping powers for slow heavy ions in C and Al showed oscillatory Z_1-dependent fluctuations about the Lindhard estimates. These oscillations were in phase for C and Al stoppers, but relatively only half as great in magnitude in Al as in C. Stopping of ^{28}Si ions was measured only in C, and fell 12% below the Lindhard value. Thus, on the assumption that stopping in Mg is similar to that in Al, it was estimated that for ^{26}Si in ^{24}Mg

$$\left.\frac{dE}{dx}\right|_e^{\text{true}} = \left.\frac{dE}{dx}\right|_e^{\text{Lindhard}} \times 0.94 \qquad (3.3r)$$

leading to a characteristic electronic stopping time of $a = 1.07$ ps. An overall error of ± 10% was allowed on the electronic stopping power.

Blaugrund et al. (Bl 67) have investigated the

accuracy of the Lindhard nuclear stopping estimate by comparing calculated and measured ion ranges. They introduced correction factors f_e and f_n as multipliers of the Lindhard electronic and nuclear stopping powers, set f_e = 1.16 (an average over many measurements), and calculated the value of f_n to best fit published ranges. For various light ions (N, Ne, Na, and A) stopping in Be, B, C or Al they obtained f_n values of 0.6 to 1.1.

In order to eliminate the possibility that the variation in f_n was wholly or partly due to the incorrect assumption of a Z_i-independent f_e, the f_n calculations were repeated for six cases where the value of f_e at velocities of order 10^8 cm/s were known (Or 65) and where measured projected ranges (i.e., mean ion distance covered in original direction of travel) were available (Po 62; Po 63; Da 61). The Gill F(γ) program was modified to calculate the projected ranges from

$$R = \int_0^\infty \langle v_i \rangle \cdot \langle \cos\theta_i \rangle \, dt \qquad (3.3s)$$

for various values of f_n, and the latter was determined by comparison with experiment. The results are collected in table 3.3A. It is apparent that there is good internal

TABLE 3.3A

Nuclear Stopping Power Correction Factor

Ion	Stopper	f_e [a]	Initial Velocity ($\times 10^8$ cm/s			
			0.45	0.9	1.8	
			f_n	f_n	f_n	f_n [c]
^{14}N	^{12}C	1.48	0.5±0.35	0.68±0.15	0.68±0.23	1.1
^{20}Ne	^{12}C	1.0	1.0±0.4	0.82±0.09	0.94±0.14	0.7
^{40}Ar	^{12}C	1.35	0.75±0.13	0.80±0.07	0.85±0.18	1.1
^{14}N	^{27}Al	1.23	0.6±0.5	0.63±0.14	0.71±0.28	0.85
^{24}Na	^{27}Al	0.83	0.62±0.1	0.69±0.05	1.02±0.15	0.7
^{42}K	^{27}Al	1.14 [b]	0.78±0.3	0.68±0.11	-	0.7
		Mean =	0.68±0.07	0.73±0.04	0.88±0.08	
		χ^2/ν [d] =	0.34	0.69	0.50	
Adopted value =			0.75±0.1			

a) Ormrod et al (Or65)

b) Estimated from ^{12}C stopping data

c) Blaugrund et al(Bl66) initial velocity not quoted

d) χ^2 divided by the degrees of freedom (ν)

agreement, and some evidence that f_n increases with initial ion velocity.

Nuclear stopping is of greatest importance for the longer lifetimes. Combining equations (3.3k) and (3.31) we obtain

$$F(\tau) = \int_0^\infty \frac{1}{\tau v_o} \cdot e^{-t/\tau} \cdot \langle v_i \rangle \cdot \langle \cos\theta_i \rangle \cdot dt \qquad (3.3t)$$

which is for long lifetimes very similar to (3.3s), and thus the determination of f_n from H is germane.

For the present purpose it was assumed that ^{26}Si stopping in ^{24}Mg would not be too different to the cases examined and the value $f_n = 0.75 \pm 0.1$ was adopted.

3.3. 4 $F(\tau)$ for Cascade Gamma Rays

Lacking pre-selection of the state under study in these neutron experiments, it was not possible to distinguish decays of a state resulting from direct population and decays following population by cascade from higher states. If such a higher state has an appreciable lifetime the $F(\tau)$ observed for the lower one will be appreciably modified.

Consider the case where a number of states of lifetime τ_i (where $i \geqslant 2$) gamma decay to a state of lifetime

τ_1. Let the relative direct populations of these states be ν_i ($i \geq 1$) at t=0, and normalised to $\sum_i \nu_i = 1$.

Then it can readily be shown that the population of the lowest state at time t is

$$\nu_1(t) = \nu_1 e^{-t/\tau_1} + \sum_{i \geq 2} \frac{e^{-t/\tau_i} - e^{-t/\tau_1}}{\tau_i - \tau_1} \cdot \tau_i \nu_i \qquad (3.3u)$$

and the decay rate from state 1 is

$$\frac{\nu_1(t)}{\tau_1} \qquad (3.3v)$$

(from eq. 3.3e)

We recall the definition of $F(\tau)$ in eq. (3.3k), noting that $\frac{e^{-t/\tau}}{\tau}$ is the decay rate of the level in that case, and abbreviate $\langle v_i \cos\theta_i \rangle_t$ to $V_i(t)$ where "i" now denotes the level. $V_i(o)$ is then the initial velocity of ions populated at level "i"!

Then from (3.3k, u, v) we obtain

$$\overline{F(\tau_1)} = \int_0^\infty \frac{1}{V_i \tau_1} \left[\nu_1 e^{-t/\tau_1} . V_i(t) + \sum_{i \geq 2} \frac{e^{-t/\tau_i} - e^{-t/\tau_1}}{\tau_i - \tau_1} . \tau_i \nu_i V_i(t) \right] dt$$

$$= \nu_1 F_1(\tau_1) + \sum_{i \geq 2} \frac{\tau_i F_i(\tau_i) - \tau_1 F_1(\tau_1)}{\tau_i - \tau_1} \times \frac{\nu_i V_i(0)}{V_1(0)} \qquad (3.3w)$$

where $\overline{F(\tau_1)}$ is the apparent $F(\tau_1)$ observed, where (3.3v) has been substituted for $\frac{e^{-t/\tau}}{\tau}$ in (3.3k), and where $F_i(\tau) = F(V_i(0), \tau)$.

3.3.5 Centroid Determination and Error Formulae

When random counts (R_i) and linearly interpolated background counts (B_i) are subtracted from the real coincidence counts (N_i) in each channel (C_i), the centroid and its error may be obtained thus:

For the present assume no error on B_i, then (summing over i):

$$\text{Centroid Channel} = \overline{C} = \frac{\sum(N_i-R_i-B_i)C_i}{\sum(N_i-R_i-B_i)} \qquad (3.3x)$$

and Total Counts = $T = N-R-B = \sum(N_i-R_i-B_i)$.

$$\text{Now} \quad \frac{\partial\overline{C}}{\partial N_i} = \frac{C_i}{\sum(N_i-R_i-B_i)} - \frac{\sum(N_i-R_i-B_i)C_i}{(\sum(N_i-R_i-B_i))^2}$$

$$= \frac{C_i}{T} - \frac{\overline{C}}{T}$$

$$\text{and similarly} \quad \frac{\partial\overline{C}}{\partial R_i} = -\frac{C_i}{T} + \frac{\overline{C}}{T}$$

$$\text{then: variance } (\overline{C}) = \sum\left[\left(\frac{\partial\overline{C}}{\partial N_i}\right)^2 \cdot N_i + \left(\frac{\partial\overline{C}}{\partial R_i}\right)^2 \cdot R_i\right]$$

$$= \sum\left(\frac{C_i}{T} - \frac{\overline{C}}{T}\right)^2 \cdot (N_i+R_i)$$

where the facts have been used that variance $(N_i) = N_i$ etc., and that variances add.

Normally the background is determined as B_a counts and B_b counts in suitable channels C_a and C_b below and above the photopeak. One then uses

$$B_i = B_a + \frac{B_b - B_a}{C_b - C_a} \cdot (C_i - C_a) \qquad (3.3y)$$

to interpolate the background. If the errors on B_a and B_b are δ_a and δ_b, and if one writes $\overline{C}$ as a function of B_a and B_b

$$\overline{C} = \overline{C}\,(B_a, B_b),$$

then the simplest way to determine the full variance of $\overline{C}$ is to compute

$$\begin{aligned} \mathrm{var}(\overline{C}) &= \sum \left(\frac{C_i}{T} - \frac{\overline{C}}{T} \right)^2 \cdot (N_i + R_i) \\ &+ \left[\overline{C}\,(B_a+\delta_a, B_b) - \overline{C}(B_a, B_b) \right]^2 \\ &+ \left[\overline{C}\,(B_a, B_b+\delta_b) - \overline{C}(B_a, B_b) \right]^2 \end{aligned}$$

A suitable program was written for the PDP7 to compute centroids and errors according to equations 3.3x,y,z and was used for the lifetime analyses of Chapter 6.

Really, if the lower orders don't set us a good example, what is the use of them?

Oscar Wilde.

C H A P T E R 4

TRITIUM EXPERIMENT RESULTS: ^{11}B and ^{14}C ANGULAR CORRELATIONS

4.1 Introduction and Experimental Details

The favourable Q-values of (t,α) and (t,p) reactions make these very useful for particle-gamma correlation experiments. Furthermore the low particle spins involved, particularly in the (t,α) reaction, coupled with (coincident) particle detection along the beam axis, severely restrict the population of magnetic substates of excited levels of the residual nucleus (cf. equation 3.2a). This often enables unique spin assignments and determination of electromagnetic multipole mixing ratios.

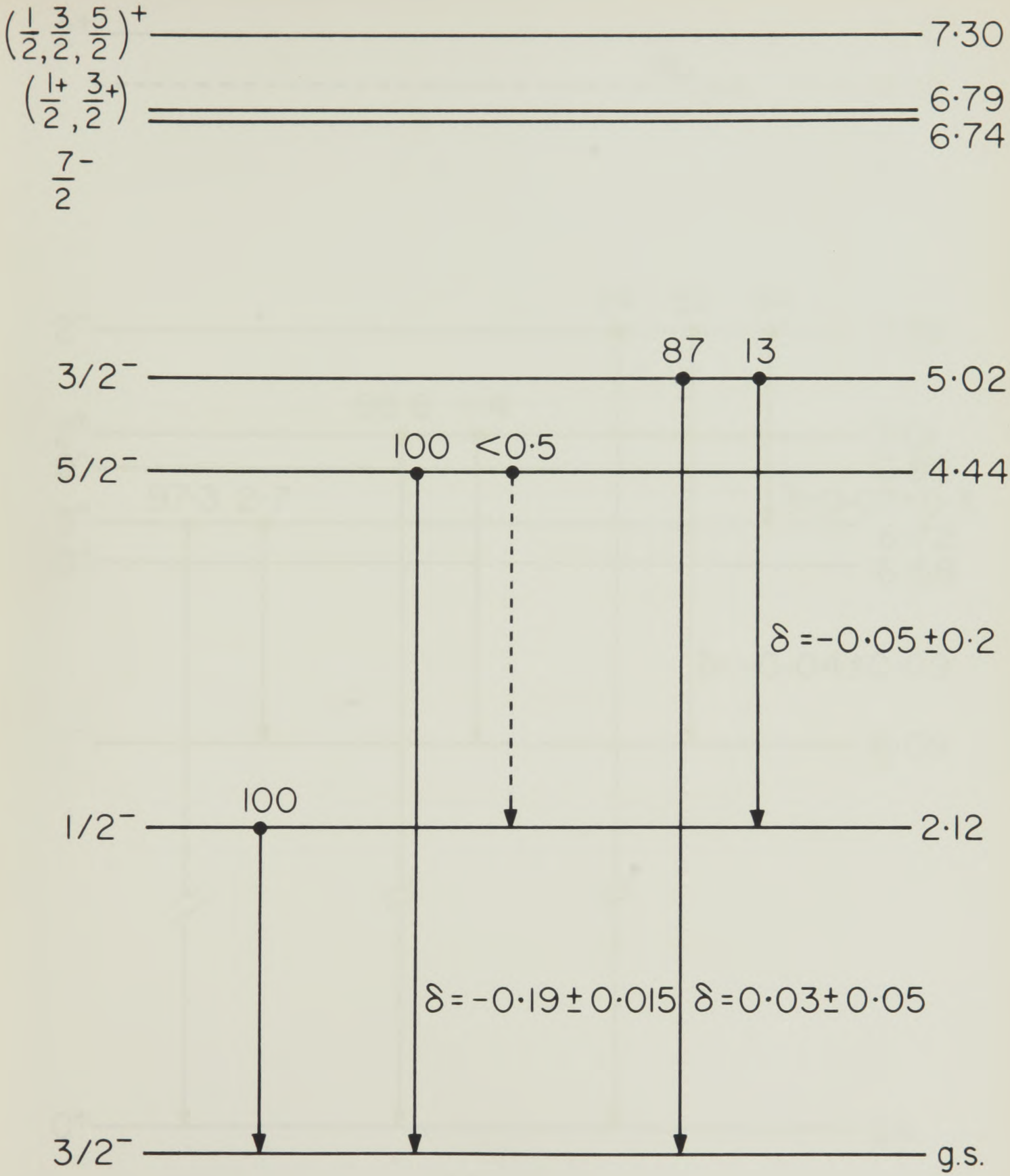
In the present instance the (t,α) and (t,p) reactions on the zero-spin ^{12}C nucleus have been used to study excited states of ^{11}B and ^{14}C. Despite intensive study in recent years (Ku 56; Ku 57; Co 65; Tr 63; Wa 60), many detailed properties of these nuclei are unknown. Simple shell-model treatments generally give satisfactory description of spins, parities, and energies. However, measurements of the decay modes and mixing ratios of the 4.44 and 5.02 MeV levels of ^{11}B and the 6.72, 7.01, and 7.35 MeV levels of ^{14}C should

provide a further, more refined, test of the wave-functions involved. Figures 4.1A and 4.1B show the lower levels of ^{11}B and ^{14}C and summarise the main results of this investigation.

The tritium beam used in the experiments to be described was provided by a Tandem van de Graaff Accelerator at A.W.R.E., Aldermaston. Many of the experimental details have already been given in section 2.1.

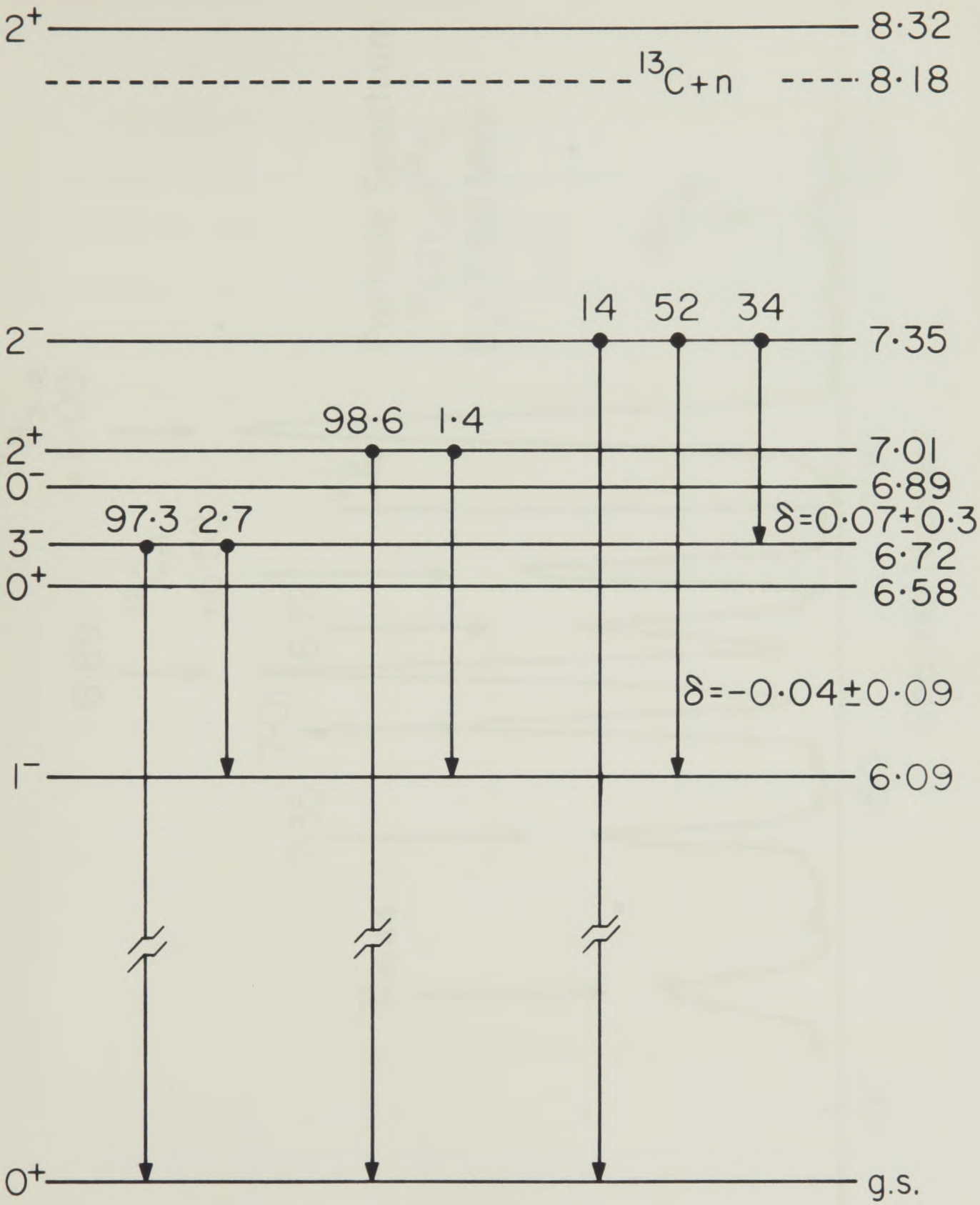
The $^{12}C(t,\alpha)^{11}B$ reaction (Q = 3.86 MeV) was used to populate the ^{11}B states. The beam energy was 7.48 MeV and the target was 80 $\mu gm/cm^2$, self-supporting, natural carbon. Particles emitted between 168° and 174° to the beam direction were fully stopped in the depleted region of a 7kΩ-cm surface-barrier counter, the bias on which was 100V. A typical digitally stabilised particle spectrum is shown in fig. 4.1C.

Detection of the alpha particles at nearly 180° to the beam direction meant that only $m = \pm \frac{1}{2}$ magnetic substates would be strongly populated (eq. 3.2a) and so the angular correlation analysis was greatly simplified. In practice higher substates might have been populated to a small extent due to the finite size of the particle counter (section 3.2.1) but the effect was unimportant even for the case of the $J = 3/2$, ^{11}B, 5.02 MeV level (cf. section 4.2.2) which



^{11}B

Figure 4·1A



^{14}C

Figure 4·1B

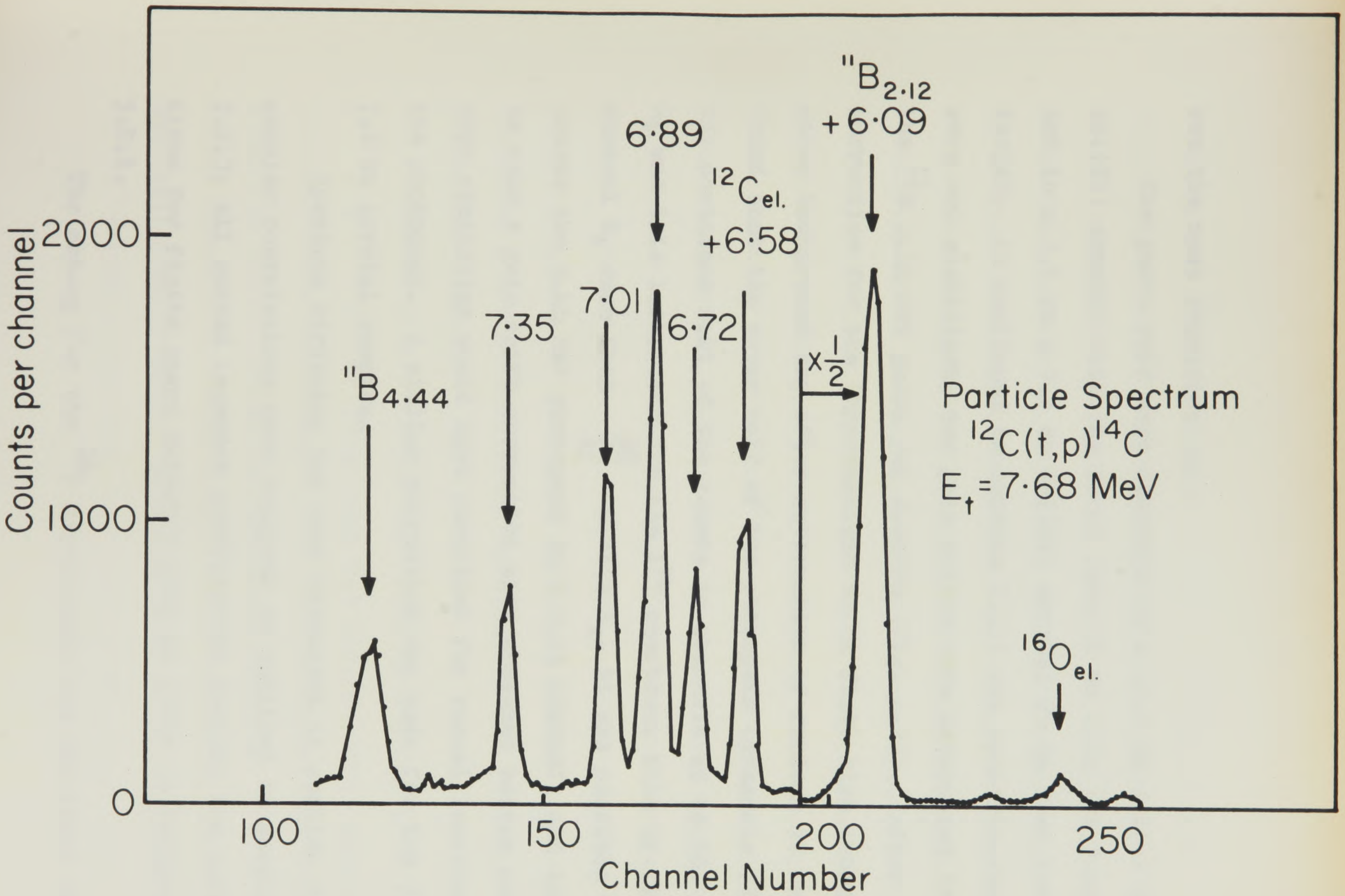

Counts per channel
2000
1000
0
100
150
200
250
Channel Number
$^{11}B_{4.44}$
7·35
7·01
6·89
$^{12}C_{el.}$
+6·58
6·72
$^{11}B_{2.12}$
+6·09
x 1/2
Particle Spectrum
$^{12}C(t,p)^{14}C$
E_t = 7·68 MeV
$^{16}O_{el.}$

Figure 4·1C

was the most sensitive one.

The gamma rays were detected in a 12.7 cm x 15.2 cm NaI(Tl) crystal with its front face 22 cm from the target, and in a 7.6 cm x 7.6 cm NaI(Tl) crystal 20 cm from the target. As mentioned in section 2.1.2 the spectrometers were not stabilised, and gain shifts were determined from the ^{11}B 4.44 MeV gamma ray spectra (fig. 4.2A). After correction for the (hypothesised to be flat) high energy gamma background and after subtraction of randoms it was found that the upper half of the photopeak (channels 77 to 88) contained 0.21 of the counts in channels 45 to 88. If N_i was this latter sum for the i^{th} spectrum, then by finding channel K_i such that $\sum_{K_i}^{88} = 0.21 \times N_i$, it was possible to locate the 4.44 MeV photopeak to $\pm$ 0.05 channel, and thence to make a gain shift correction with somewhat better accuracy than statistics would have permitted for visual location of the photopeak. A similar correction was made for the 7.6 x 7.6 cm crystal spectra.

Spectrum stripping has been discussed in section 3.2.2; angular correlations were analysed as outlined in section 3.2.3; all quoted Legendre coefficients include the corrections for finite gamma detector size as given in section 3.2.1.

The set-up for the ^{14}C experiments was identical to

that for the ^{11}B experiments except that levels were populated by the $^{12}C(t,p)^{14}C$ reaction (Q = 4.64 MeV) at a beam energy of 7.68 MeV, the 13 cm x 15 cm crystal was 21 cm from the target, and the 8 cm x 8 cm crystal was 23 cm from the target. With that arrangement the 13 cm x 15 cm crystal was efficient enough to obtain adequate statistics for a correlation on the various branches of the ^{14}C, 7.35 MeV level, whilst the 8 cm x 8 cm crystal was far enough from the target to not excessively attenuate the anticipated P_6 term in the ^{14}C, 6.72 MeV → ground state decay correlation. Gain shift corrections were determined in a fashion similar to that described for the ^{11}B experiments. One last point: in the (t,p) reaction magnetic substates with m = 0, ± 1 were populated and so the population parameter p was an additional variable in the fitting procedures (section 3.1).

Whenever both crystals were used in a study of a level of ^{11}B or ^{14}C it was found that the results were compatible. In these cases the mixing ratios and the values for the branching ratios quoted are weighted averages. The experimental results for spin, mixing ratios and decay modes have been collected in tables 4.1A and 4.1B. A representative χ^2/ν versus δ plot will be found in fig. 4.2E; this

Table 4.1A

Summary of Present Experimental Results for ^{11}B

Transition (Branch)	Legendre Analysis	Solutions for J, δ
4.44 → g. s.	$a_2 = 0.02 \pm 0.03$	$J = \frac{1}{2}$, δ undetermined
(> 97%)	$a_4 = -0.09 \pm 0.05$	$J = 3/2$, $\delta = 0.27 \pm 0.06$
		or $\lvert\delta\rvert > 15$
		$J = 5/2$, $\delta = -0.19 \pm 0.03$
5.02 → g. s.	$a_2 = 0.35 \pm 0.04$	$J = 3/2$, $\delta = 0.03 \pm 0.05$
		or -4^{+1}_{-2} *
(88 ± 2.5%)	$a_4 = 0.0 \pm 0.1$	$J = 5/2$, $\delta = -0.38 \pm 0.05$ *
5.02 → 2.12	$a_2 = -0.4 \pm 0.2$	$J = 3/2$, $\delta = -0.05 \pm 0.2$
		or $\delta = 2^{+1.7}_{-0.7}$
(12 ± 2.5%)	$a_4 = -0.1 \pm 0.3$	$J = \frac{1}{2}$, δ undetermined *

* These solutions are eliminated by arguments given in the text.

Table 4.1B

Summary of Present Experimental Results for ^{14}C

Transition (Branch)	Legendre Analysis	Solutions for J, δ, p
6.72 → g.s.	$a_2 = 0.81 \pm 0.03$	J = 3, p = 0.67 ± 0.07 (δ = 0)
(97.3 ± 1%)	$a_4 = 0.32 \pm 0.05$	
	$a_6 = -0.88 \pm 0.06$	
7.01 → g.s.	$a_2 = 0.62 \pm 0.02$	J = 2, p = 0.73 ± 0.04 (δ = 0)
(98.6 ± 0.7%)	$a_4 = -0.95 \pm 0.035$	
7.35 → g.s.	$a_2 = 0.51 \pm 0.14$	J = 2, p = 0.75 ± 0.20 (δ = 0)
(14 ± 4%)	$a_4 = -1.16 \pm 0.31$	
7.35 → 6.09	$a_2 = -0.33 \pm 0.05$	δ = -0.04 ± 0.09
(52 ± 5%)	$a_4 = 0.02 \pm 0.10$	
7.35 → 6.72	$a_2 = 0.00 \pm 0.09$	δ = 0.07 ± 0.3
(34 ± 4%)	$a_4 = 0.23 \pm 0.19$	

illustrates the main features of such plots and they have not been reproduced here for all analyses.

4.2 Experimental Results

4.2. 1 The 4.44 MeV Level of ^{11}B

A 13 x 15 cm crystal gamma ray spectrum is shown in fig. 4.2A. From this an upper limit of 3% is placed on a possible 4.44 → 2.12 MeV transition. The small high-energy background appeared in both crystals and was corrected for when extracting the correlations (fig. 4.2B). It probably arose from a small contamination of the particle window by particles feeding the 9.77 MeV level of ^{15}N via the $^{16}O(t,\alpha)^{15}N$ reaction. (The small peak near channel 240 of fig. 4.1C indicated the presence of a slight amount of oxygen in the target). The Legendre coefficients and the extracted mixing ratios and allowed spin values are collected in table 4.1A.

4.2. 2 The 5.02 MeV Level of ^{11}B

A 13 x 15 cm crystal gamma ray spectrum is shown in fig. 4.2C. The ^{11}B, 5.02 MeV level was found to decay (12 ± 2.5)% to the 2.12 MeV level, and (88 ± 2.5)% to ground.

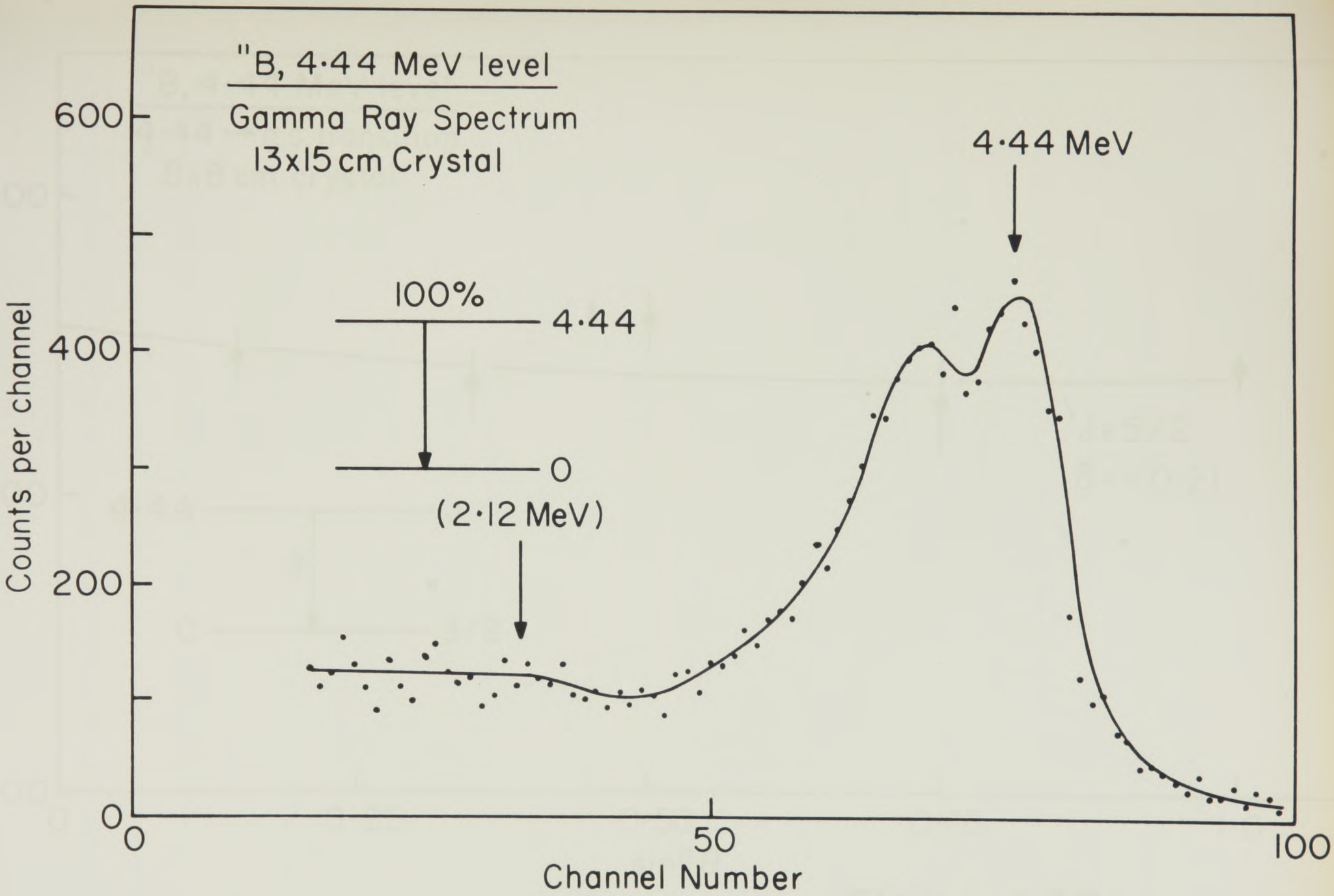

"B, 4·44 MeV level
Gamma Ray Spectrum
13x15 cm Crystal
4·44 MeV
100%
4·44
0
(2·12 MeV)
600
400
200
0
Counts per channel
0
50
100
Channel Number

Figure 4·2A

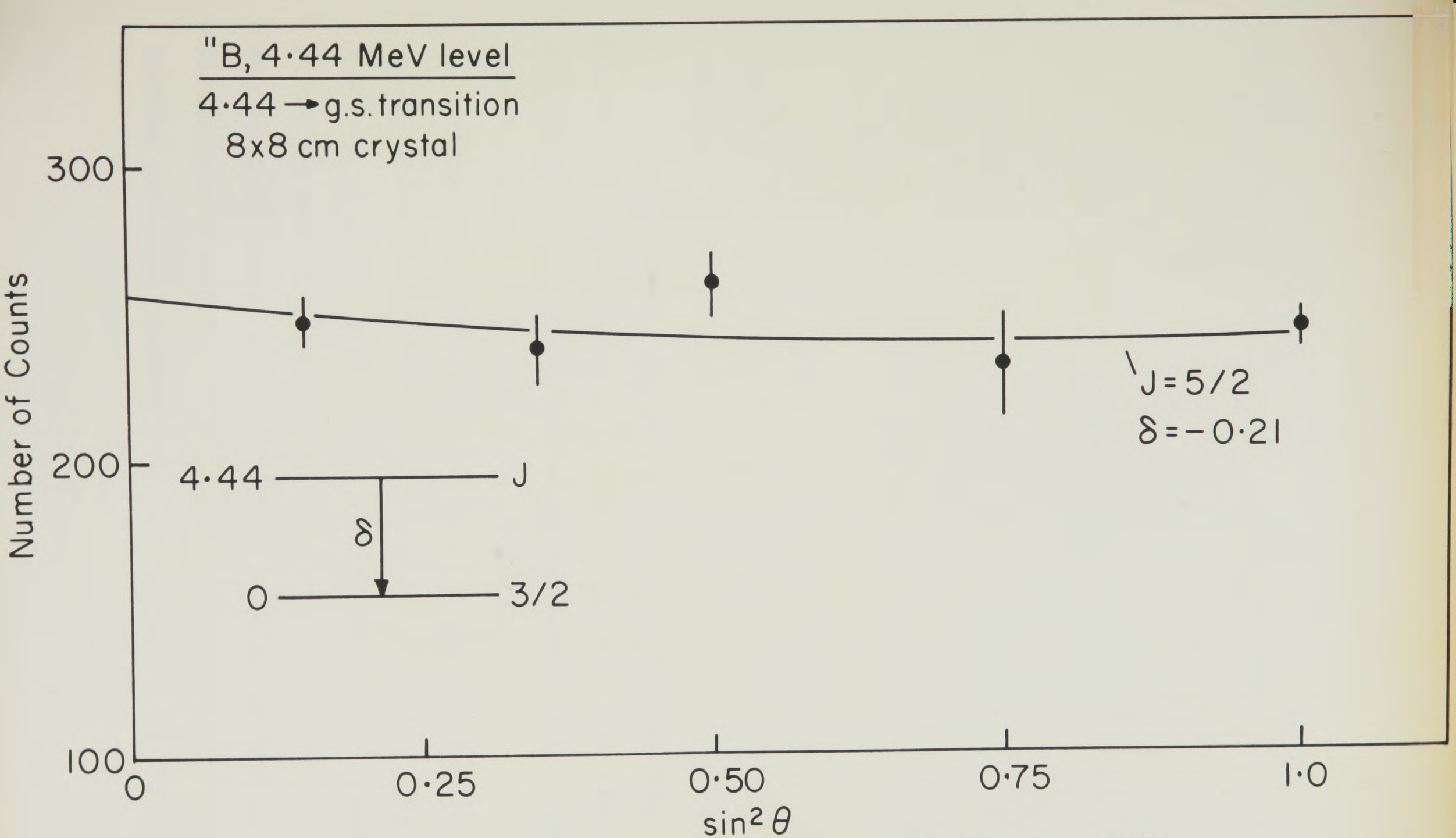

"B, 4·44 MeV level
4·44 → g.s. transition
8x8 cm crystal
Number of Counts
300
200
100
4·44
J
δ
0
3/2
J=5/2
δ=−0·21
0
0·25
0·50
0·75
1·0
sin² θ

Figure 4·2B

The correlation (fig. 4.2D) of the 5.02 MeV transition to the $J = 3/2$ ground state eliminated all spins other than $3/2$ and $5/2$ (Fig. 4.2E, table 4.1A). There is convincing evidence (Aj 68; Ol 65; Do 61; Blk 67) that the 2.12 MeV level has $j = \frac{1}{2}$. Accepting this, the 5.02 → 2.12 MeV correlation (fig. 4.2F) eliminated the $J = 5/2$ solution (table 4.1A) to give $J = 3/2$ for the 5.02 MeV level. The 2.12 MeV → g.s. cascade correlation was compatible with this result.

As a test of the sensitivity of the 5.02 MeV → g.s. transition mixing ratio to contamination by the $m = \pm 3/2$ substate, the χ^2 curves were computed for $p = 1.0$ and $p = 0.97$, the latter representing a 3% contamination. As can be seen from figure 4.2E the change in δ was well within its error. This test was always performed, but in all other cases the effect was even smaller.

Background high energy gamma rays can arise from coincidences with particles feeding the ^{15}N, 10.07 MeV and the ^{18}O, 7.84 MeV (via $^{16}O(t,p)^{18}O$) states. The former state has spin $3/2$ and decays primarily to ground (Ph 67): the spin and decay modes of the latter are not known. Assuming a 5% contamination by each (in rough accord with general particle spectrum background height) and the worst

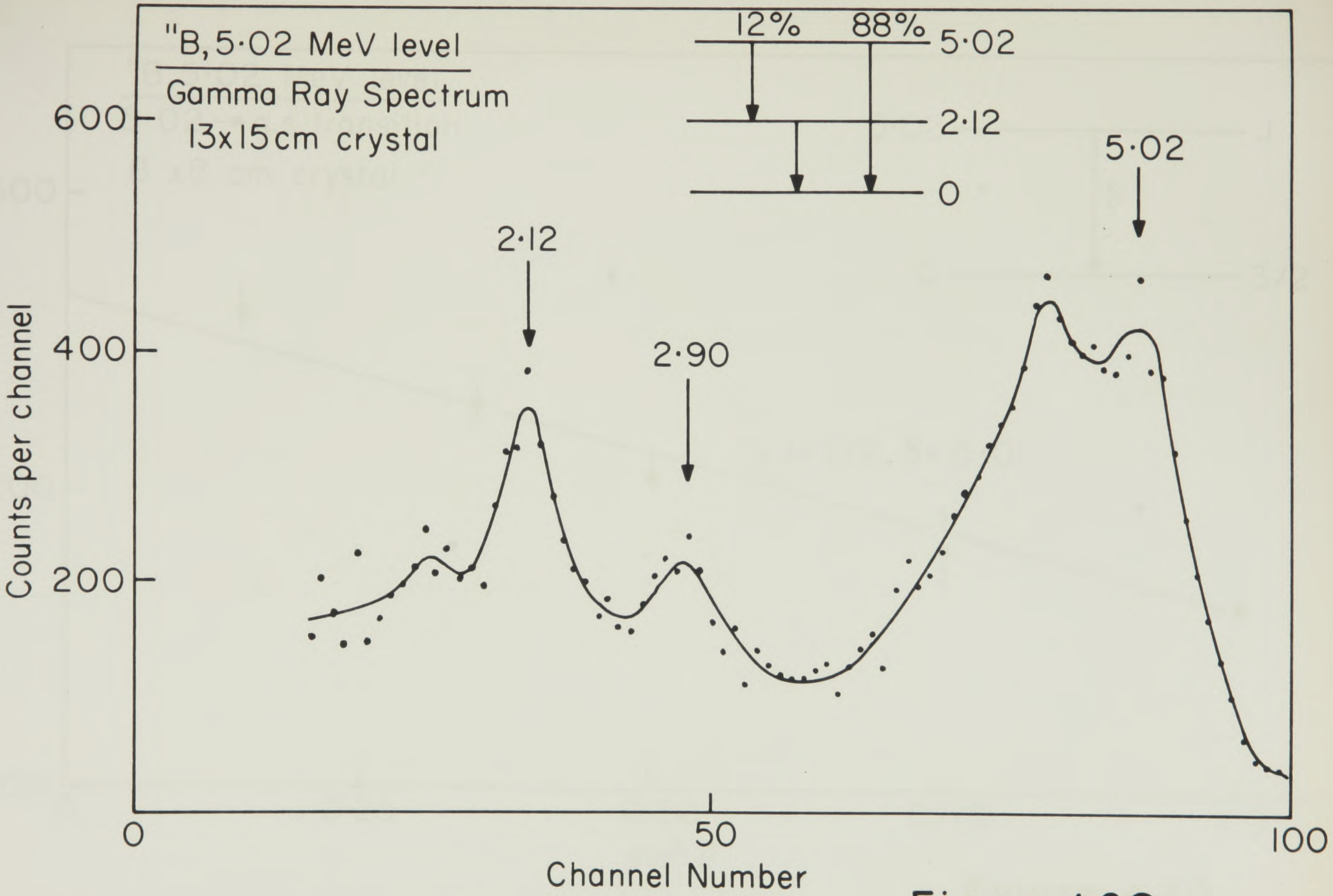

"B, 5·02 MeV level
Gamma Ray Spectrum
13x15cm crystal
12%
88%
5·02
2·12
0
2·12
2·90
5·02
600
400
200
Counts per channel
0
50
100
Channel Number

Figure 4·2C

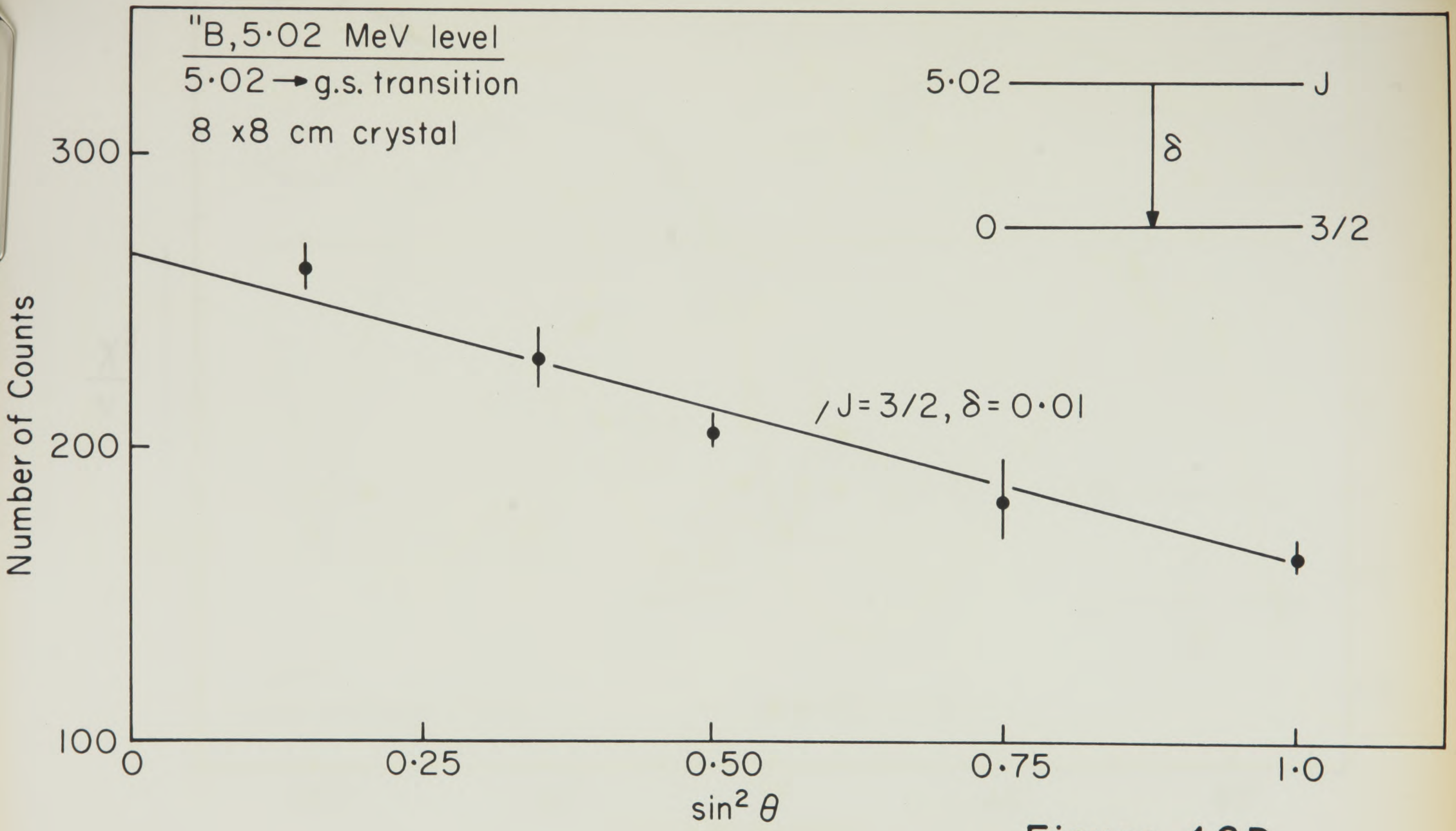

"B, 5·02 MeV level
5·02 → g.s. transition
8 x8 cm crystal
5·02
J
δ
0
3/2
J=3/2, δ=0·01
Number of Counts
300
200
100
0
0·25
0·50
0·75
1·0
sin² θ

Figure 4·2D

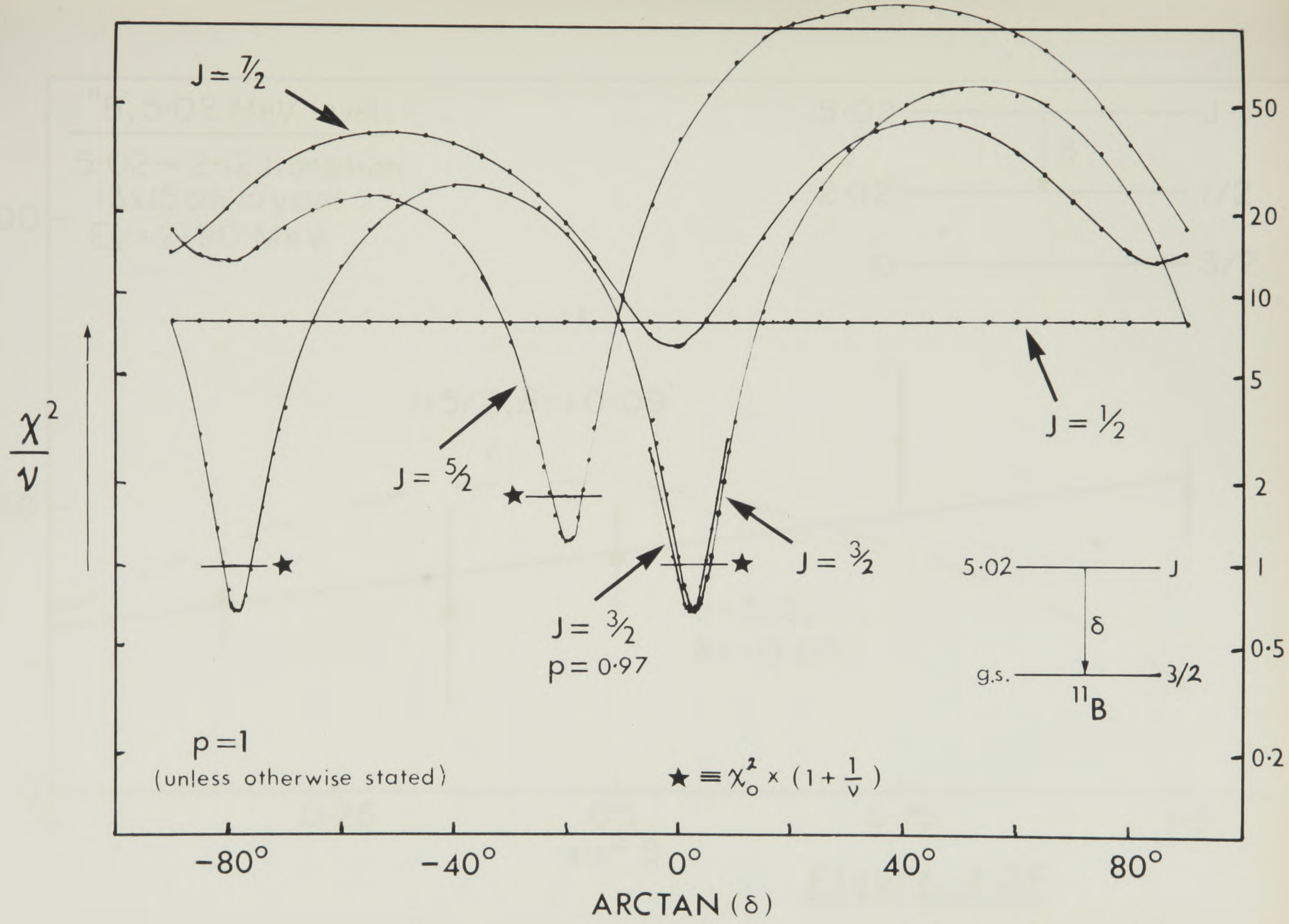

J = 7/2
J = 5/2
J = 1/2
J = 3/2
J = 3/2
p = 0·97
p = 1
(unless otherwise stated)
★ ≡ χ²₀ × (1 + 1/ν)
χ²/ν
50
20
10
5
2
1
0·5
0·2
5·02
J
δ
g.s.
3/2
11B
−80°
−40°
0°
40°
80°
ARCTAN (δ)

Figure 4·2E

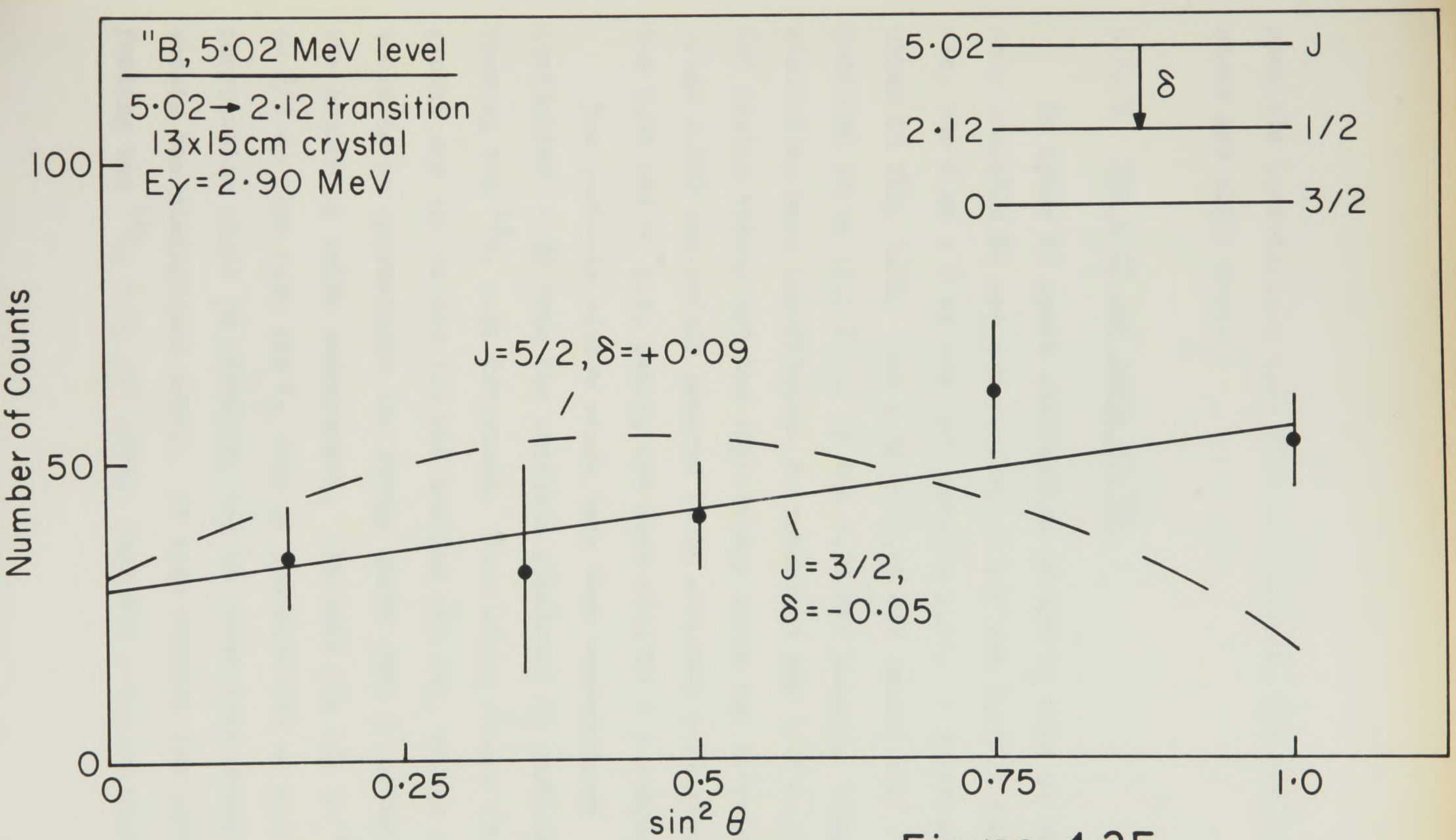

"B, 5·02 MeV level
5·02→2·12 transition
13x15 cm crystal
Eγ=2·90 MeV
5·02
2·12
0
J
δ
1/2
3/2
J=5/2, δ=+0·09
J=3/2,
δ=-0·05
Number of Counts
100
50
0
0
0·25
0·5
0·75
1·0
sin² θ

Figure 4·2F

possible interference with the correlations, the conclusions above are still valid.

4.2. 3 The 6.72 MeV level of ^{14}C

In order to avoid attenuation of the P_6 term it was only possible to use the smaller of the two NaI(Tl) crystals, viz. the 8 cm x 8 cm one (cf. section 4.1). A spectrum is shown in fig. 4.2G. The 6.72 → 6.09 MeV branch was measured to be (2.7 ± 1)% of the 6.72 MeV decays. Consequently statistics were insufficient to determine the 6.72 → 6.09 MeV mixing ratio, but the high-energy gamma ray correlation (fig. 4.2H) was safely assumed to be entirely determined by the 6.72 MeV → g.s. decay, and gave J(6.72) = 3 uniquely.

The particle window could have been contaminated (estimated $< 5\%$ from the particle spectrum) by particles feeding the ^{15}N, 8.31 MeV state. This state decays 79% to ground and 11% to the 5.3 MeV doublet (Ph 67), and so there would be no appreciable low energy gamma rays to affect the branching ratio measurement. Its spin (Wa 65) is $^1/_2$ or $^3/_2$ so that only the P_2 term of the 6.72 MeV → g.s. correlation might be affected, but at worst this would be within the statistical error. Of more concern are particles feeding the ^{18}O, 6.39 MeV level: that the particle window

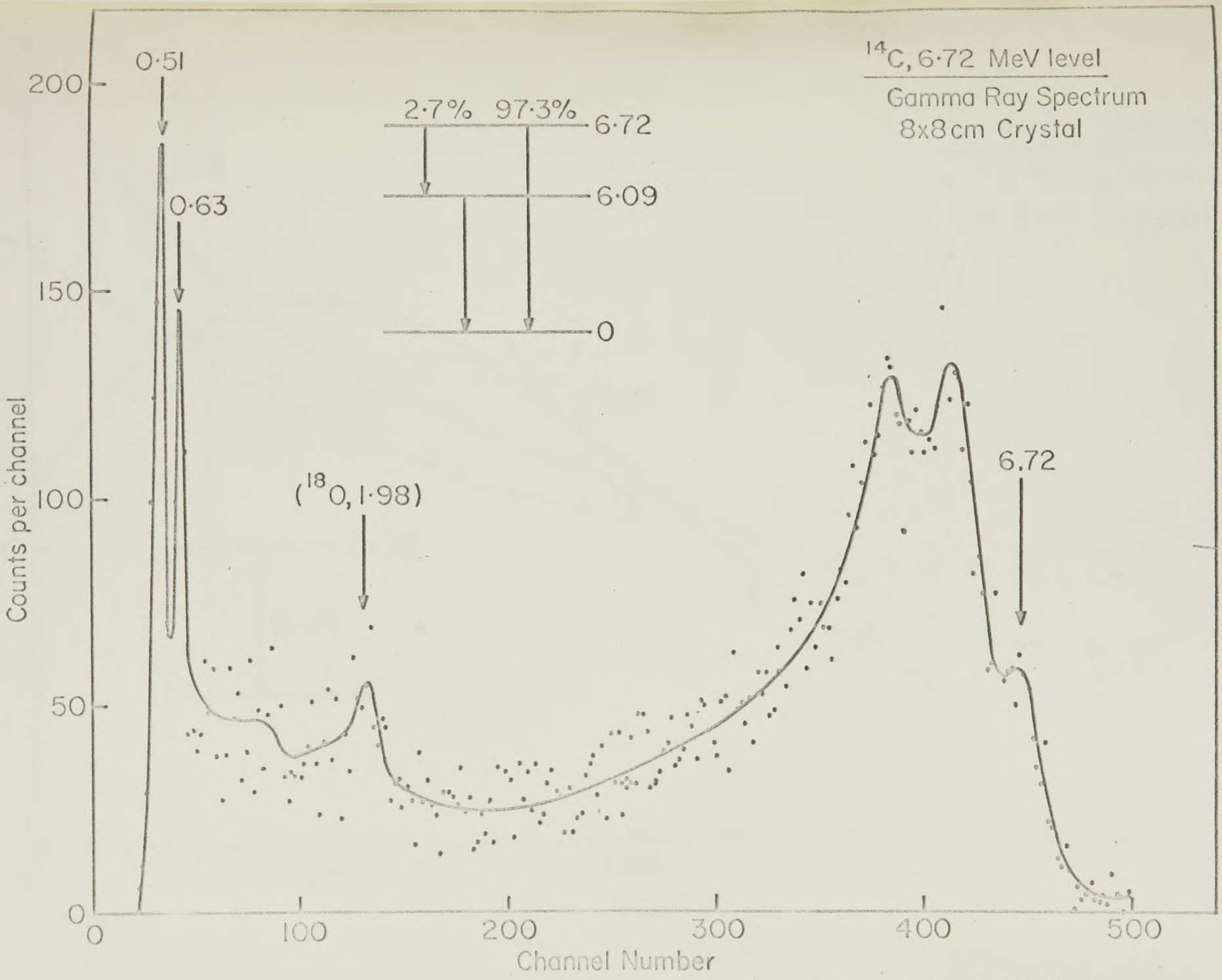

^{14}C, 6·72 MeV level
Gamma Ray Spectrum
8x8 cm Crystal
0·51
0·63
2·7% 97·3%
6·72
6·09
0
(^{18}O, 1·98)
6.72
Counts per channel
Channel Number
0
50
100
150
200
0
100
200
300
400
500

Figure 4·2G

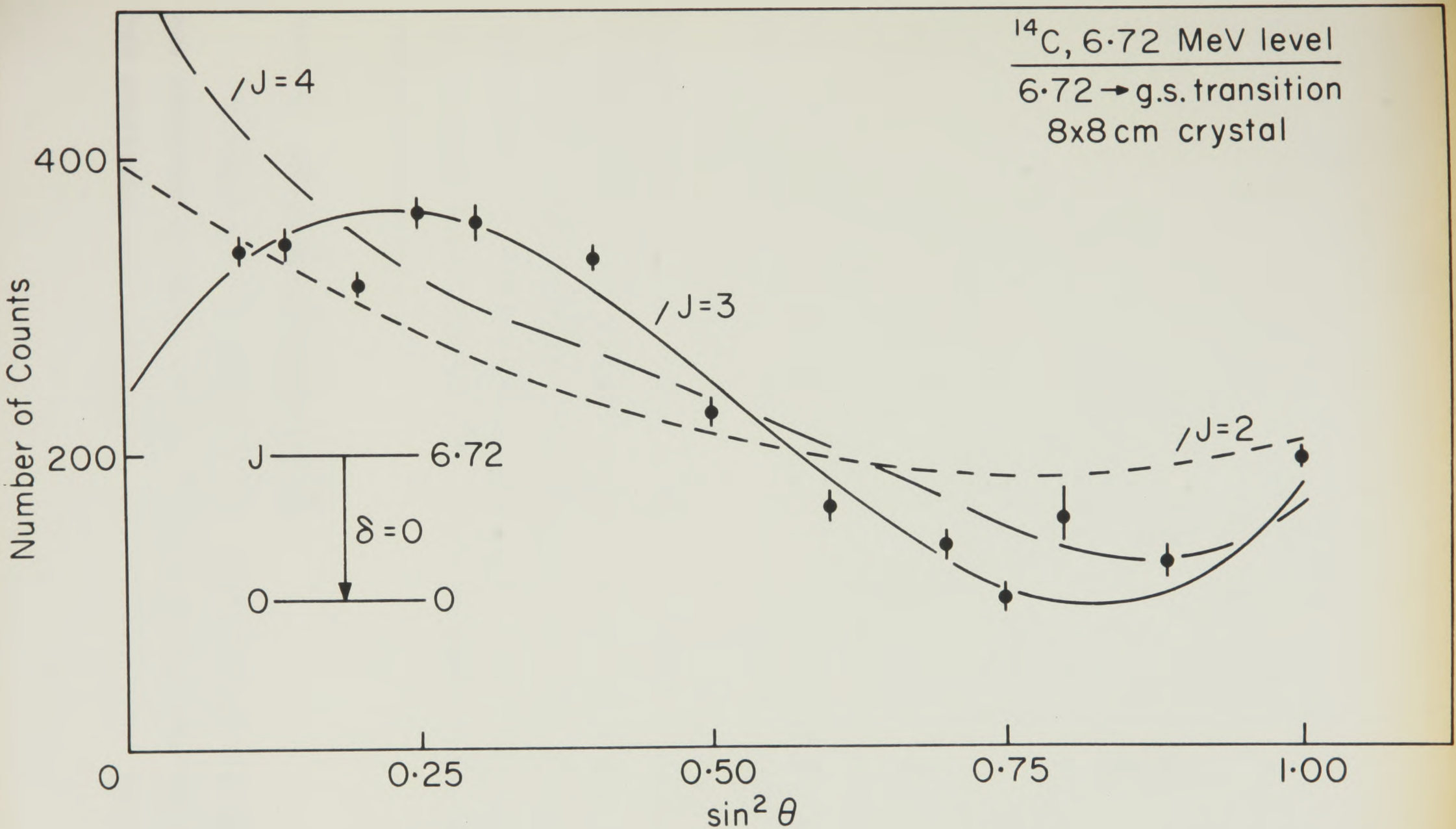

^{14}C, 6·72 MeV level
6·72 → g.s. transition
8x8 cm crystal
J=4
J=3
J=2
400
200
Number of Counts
J
6·72
δ=0
0
0
0
0·25
0·50
0·75
1·00
sin² θ

Figure 4·2H

has thus been contaminated is evidenced by the 1.98 MeV gamma ray appearing in the spectrum (fig. 4.2G) with an intensity of ~3% of the ^{14}C, 6.72 MeV → g.s. decays. The properties of the ^{18}O, 6.39 MeV level are not known, but so far as the ^{14}C branching ratio measurement is concerned, it is known (Lo 66) that no strong transitions below 5.52 MeV in ^{18}O have energies near 0.63 MeV: the only possible one remaining is the 6.19 → 5.52 MeV transition which, if it occurs, must be preceded by a transition of less than 0.2 MeV from the 6.39 MeV level, and would therefore be very weak. Thus the ^{14}C, 6.72 → 6.09 MeV branch is established.

The 6.72 MeV correlation is a striking example of a large P_6 term ($a_6 = -0.88 \pm 0.06$). The worst possible contamination effect arises if the ^{18}O, 6.39 MeV level has $J = 3$ and decays primarily to ground. Then, for 10% contamination, it would contribute an $A_6 = -0.2$. This leaves $A_6 < -0.68 \pm 0.06$ for the ^{14}C, 6.72 MeV level, which still uniquely gives $J = 3$.

4.2.4 The 7.01 MeV level of ^{14}C

In the 8 x 8 cm crystal (fig. 4.2I) the 0.92 MeV gamma ray indicates a branch of (1.4 ± 0.7)% to the 6.09 MeV level, but statistics were inadequate for a correlation. The high-

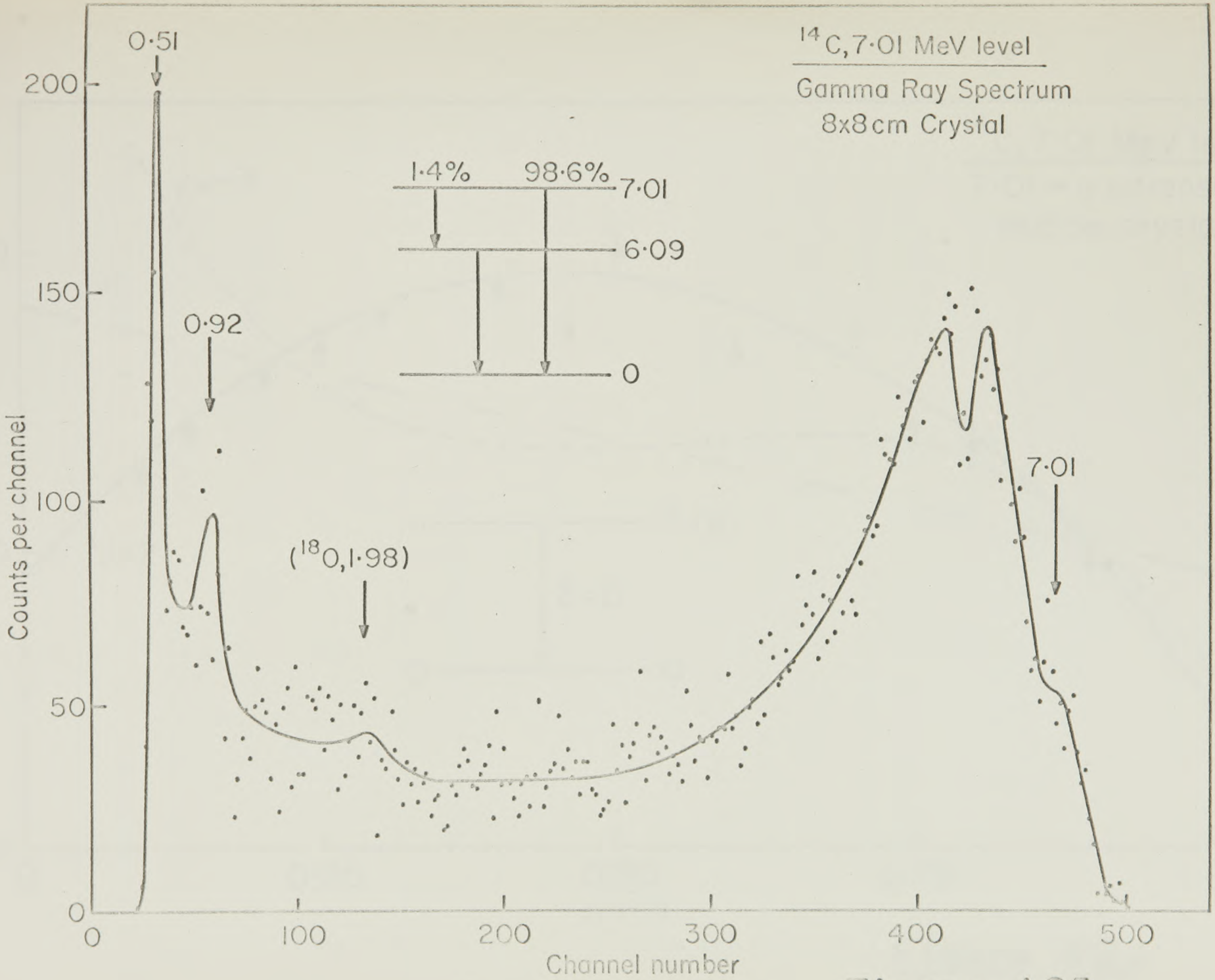

^{14}C, 7·01 MeV level
Gamma Ray Spectrum
8x8 cm Crystal
0·51
0·92
(^{18}O, 1·98)
7·01
1·4%
98·6%
7·01
6·09
0
Counts per channel
Channel number
0
50
100
150
200
0
100
200
300
400
500

Figure 4·21

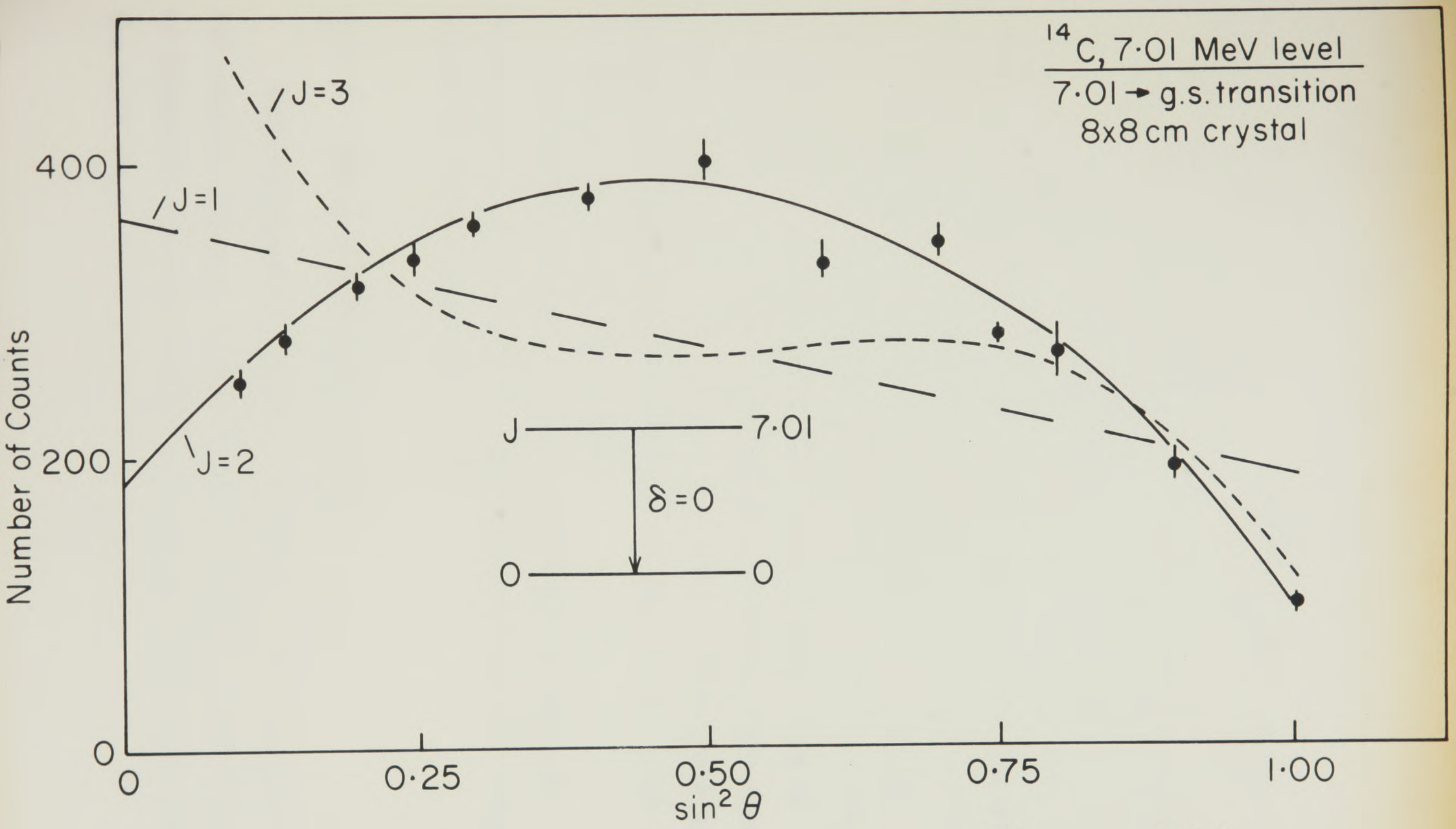

^{14}C, 7·01 MeV level
7·01 → g.s. transition
8x8 cm crystal
J=3
J=1
J=2
400
200
0
Number of Counts
J
7·01
δ=0
0
0
0
0·25
0·50
0·75
1·00
sin² θ

Figure 4·2J

energy 7.01 MeV → g.s. correlation (fig. 4.2J) uniquely determined J = 2.

The ^{18}O, 1.98 MeV gamma ray appears (~2% of the ^{14}C, 7.01 MeV → g.s. intensity) in the spectrum shown in fig. 4.2I. The nearest ^{18}O level which might appear in the particle spectrum is that at 6.86 MeV, the properties of which are unknown. The only known ^{18}O gamma ray of ~0.9 MeV originating below 5.52 MeV is from the 5.33 → 4.45 MeV (E_γ = 0.88 MeV) transition (Lo 66). Since decays of the 5.33 MeV state produce four times as many gamma rays of 1.98 MeV as of 0.88 MeV, the observed 2% intensity of the former puts an upper limit of 0.5% on the latter. This possible contamination has been allowed for in the ^{14}C, 0.92 MeV branching ratio, and its error.

The measured A_4 = - 0.95 is sufficiently large to guarantee J = 2 for the ^{14}C, 7.01 level despite any likely degree of contamination from ^{18}O.

4.2. 5 The 7.35 MeV level of ^{14}C

Both crystals were used. In the 8 x 8 cm crystal with 256 channel dispersion (fig. 4.2K) statistics were inadequate to determine the full-energy 7.35 MeV photopeak area, but the 0.63 (7.35 → 6.72) MeV to 1.26 (7.35 → 6.09) MeV

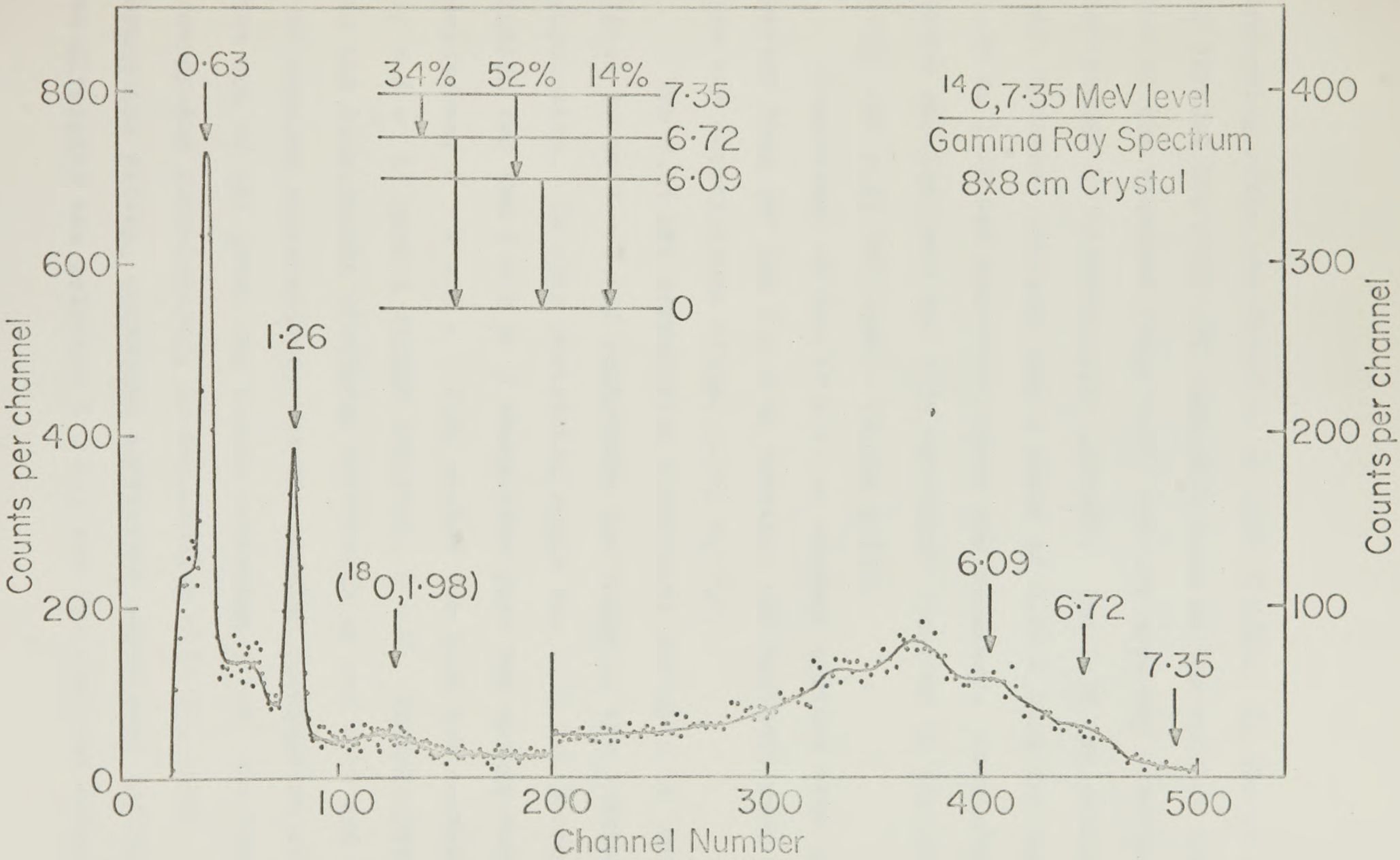

0·63
1·26
(18O,1·98)
6·09
6·72
7·35
34%
52%
14%
7·35
6·72
6·09
0
14C, 7·35 MeV level
Gamma Ray Spectrum
8x8 cm Crystal
Counts per channel
Channel Number
0
100
200
300
400
500
800
600
400
200
0
400
300
200
100

Figure 4·2K

branching ratio was found to be 0.66 ± 0.03. In the 13 x 15 cm crystal the 0.63 MeV photopeak came at the extreme lower end of the spectrum (fig. 4.2L) and its area may have been influenced by discriminator cut-off. The 7.35 MeV photopeak was, however, distinct and a value of 0.28 ± 0.04 for the 7.35 to 1.26 MeV branching ratio was obtained. Combining these results gave the 7.35 MeV level branches to the ground, 6.09, and 6.72 MeV levels (table 4.1B).

Statistics of the 13 x 15 cm crystal spectra were much better than for the 8 x 8 cm crystal, and so these were used for the correlations (figs. 4.2M, N, O,P).

The 7.35 MeV correlation determined the spin of this level to be J = 2 and restricted the range of the substate population. In this restricted range the 0.63 MeV correlation for the J = 2 → 3 transition gave two mixing ratio solutions, $\delta \sim 0$ and $\delta > 2.5$, whilst the 1.26 MeV correlation (J = 2 → 1) gave a single solution, $\delta \sim 0$. Uncertainties in the line-shapes precluded extraction of the 6.09 and 6.72 MeV cascade correlations, but the angular correlation of the sum of all gamma ray counts exceeding 3 MeV (the high-energy-sum correlation), in conjunction with the known branching ratios, contained sufficient additional information to eliminate the solution $\delta > 2.5$ for the 0.63 MeV transition.

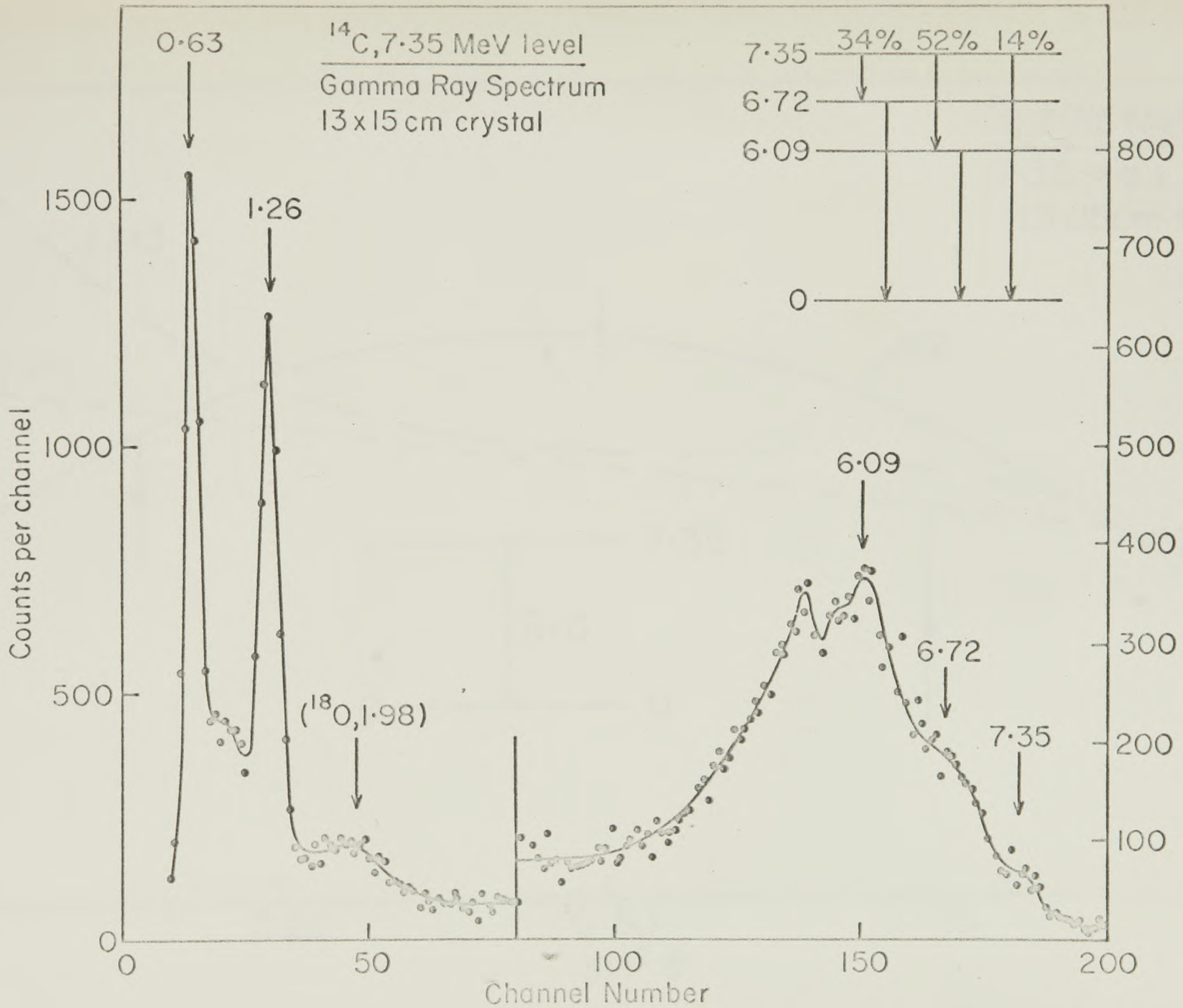

0·63
^{14}C, 7·35 MeV level
Gamma Ray Spectrum
13 x 15 cm crystal
7·35
6·72
6·09
0
34% 52% 14%
1·26
6·09
6·72
7·35
(^{18}O, 1·98)
Counts per channel
Channel Number
0
500
1000
1500
100
200
300
400
500
600
700
800
50
150

Figure 4·2L

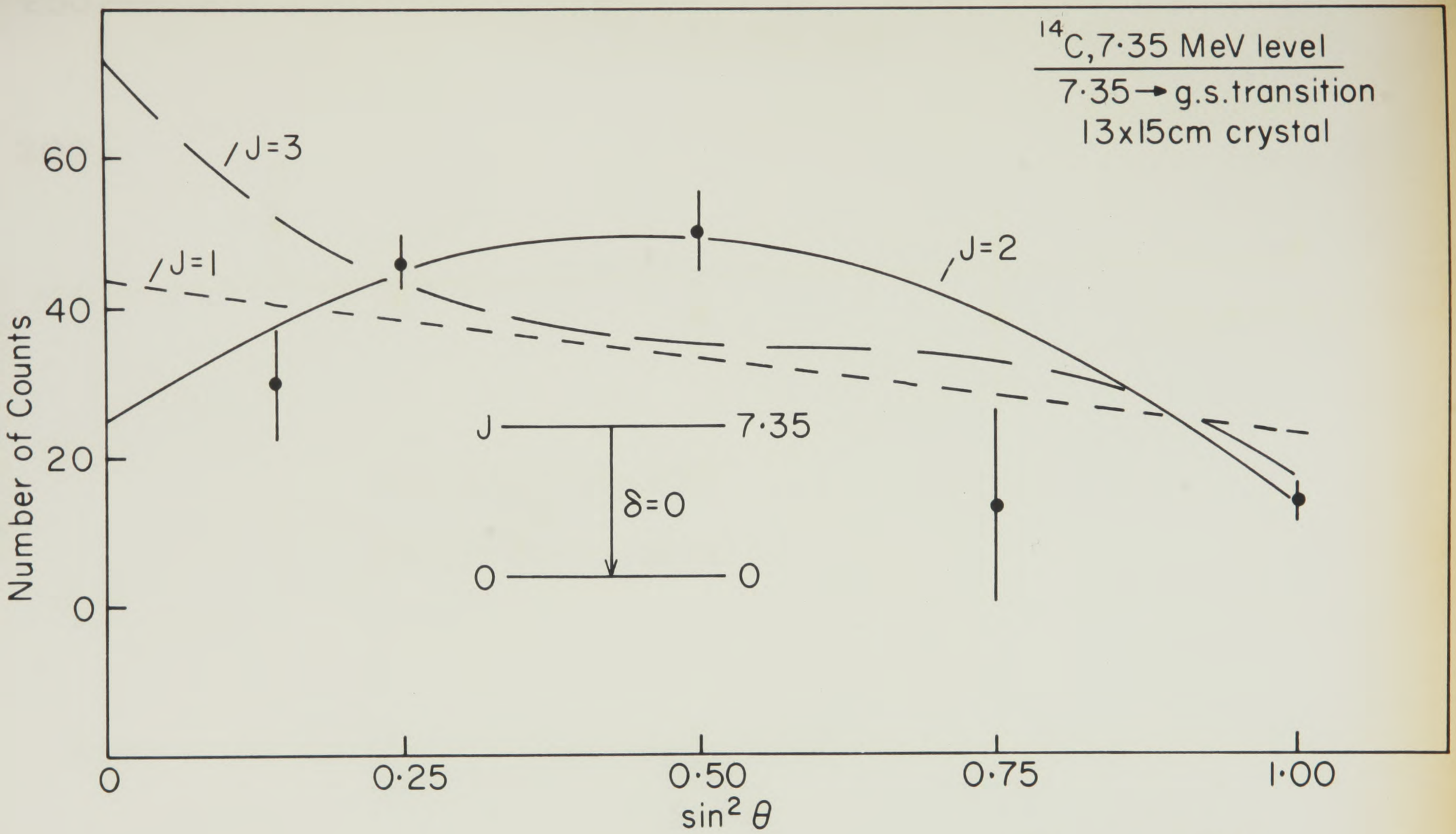

^{14}C, 7·35 MeV level
7·35 → g.s. transition
13x15cm crystal
J=3
J=1
J=2
J
7·35
δ=0
0
0
Number of Counts
60
40
20
0
0
0·25
0·50
0·75
1·00
sin² θ

Figure 4·2M

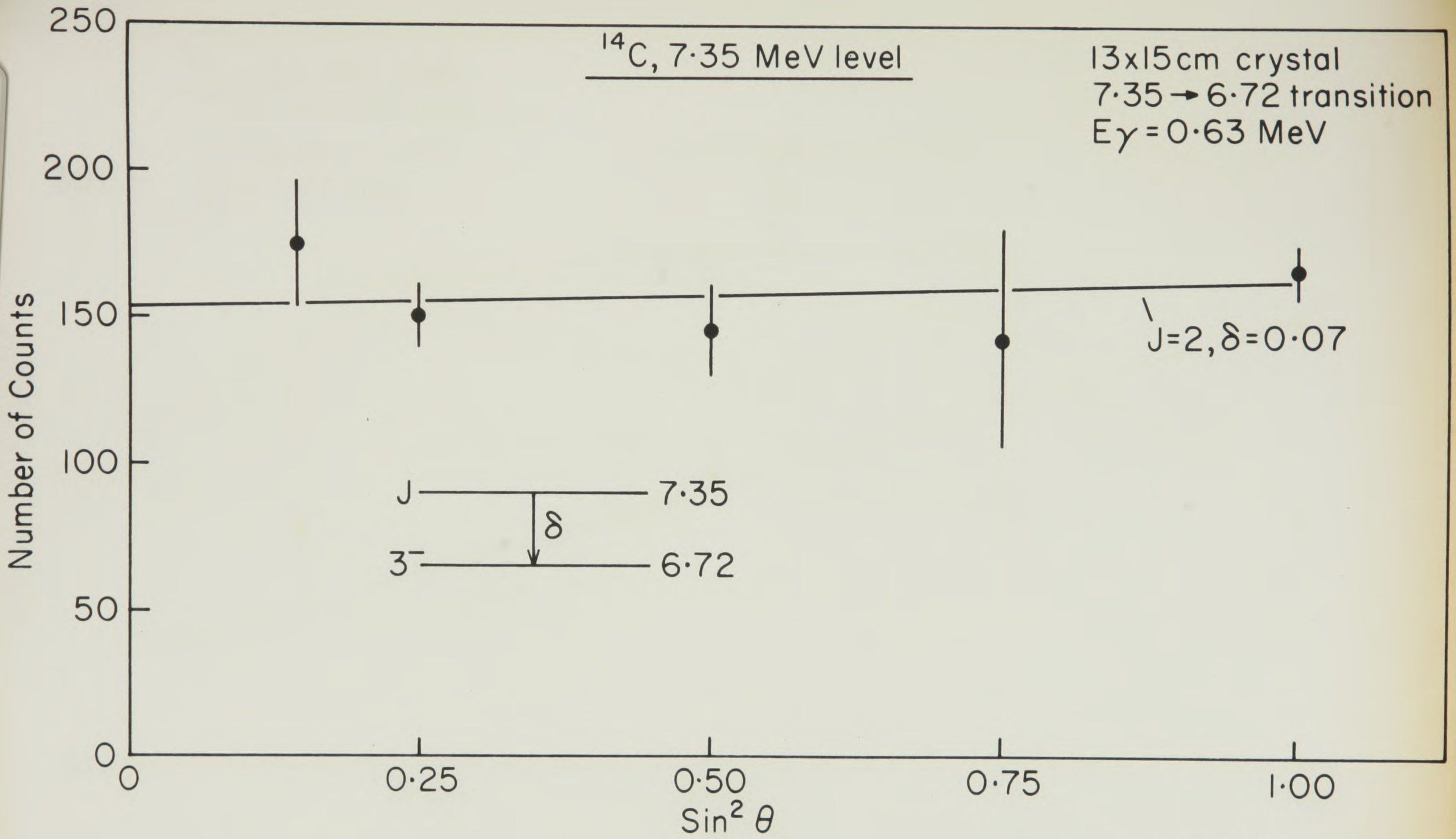

^{14}C, 7·35 MeV level
13x15cm crystal
7·35 → 6·72 transition
Eγ = 0·63 MeV
J=2, δ=0·07
J
7·35
δ
3⁻
6·72
Number of Counts
250
200
150
100
50
0
0
0·25
0·50
0·75
1·00
Sin² θ

Figure 4·2N

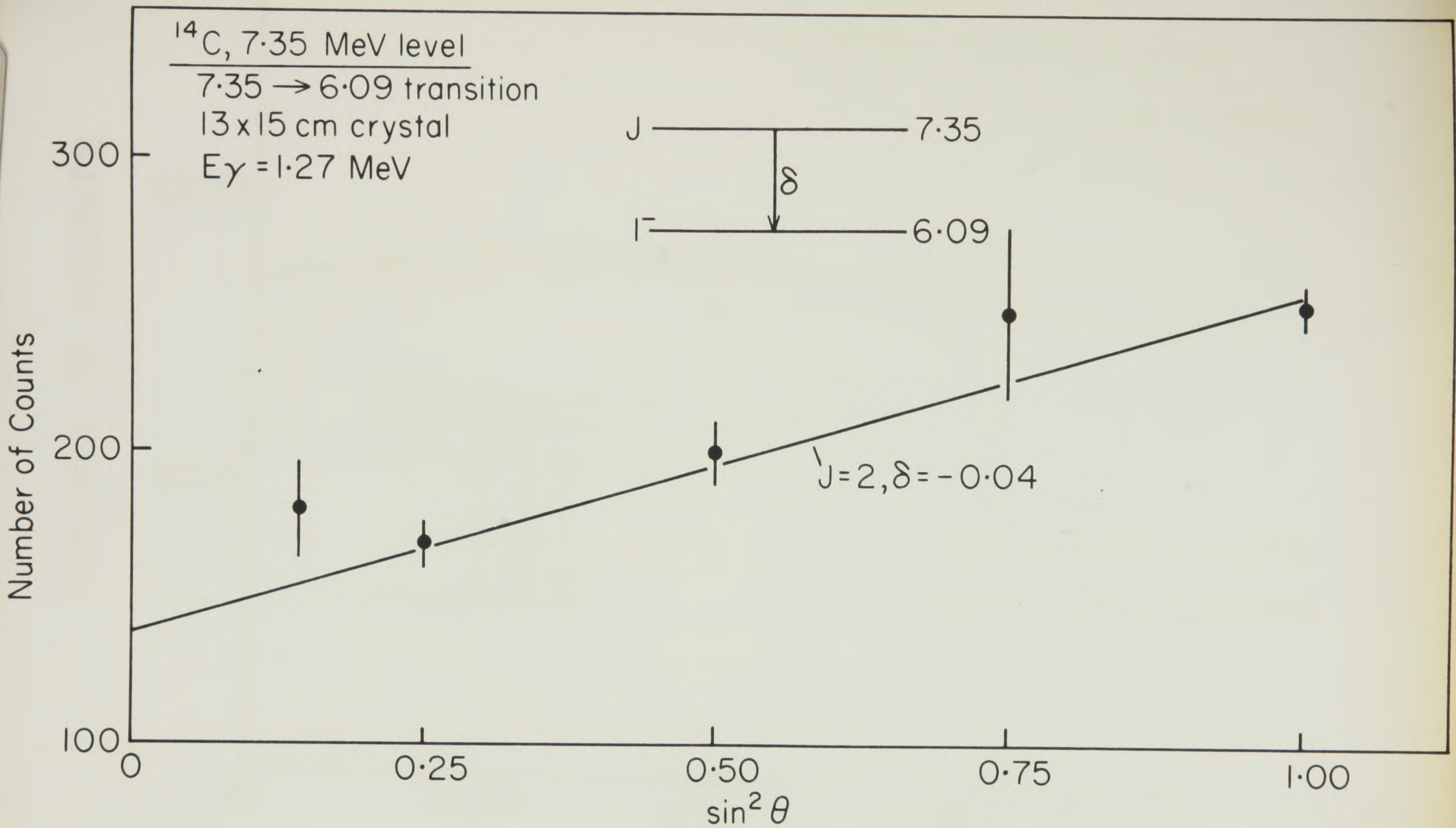

^{14}C, 7·35 MeV level
7·35 → 6·09 transition
13 x 15 cm crystal
Eγ = 1·27 MeV
J
7·35
δ
1⁻
6·09
J=2, δ=-0·04
Number of Counts
300
200
100
0
0·25
0·50
0·75
1·00
sin² θ

Figure 4·2 O

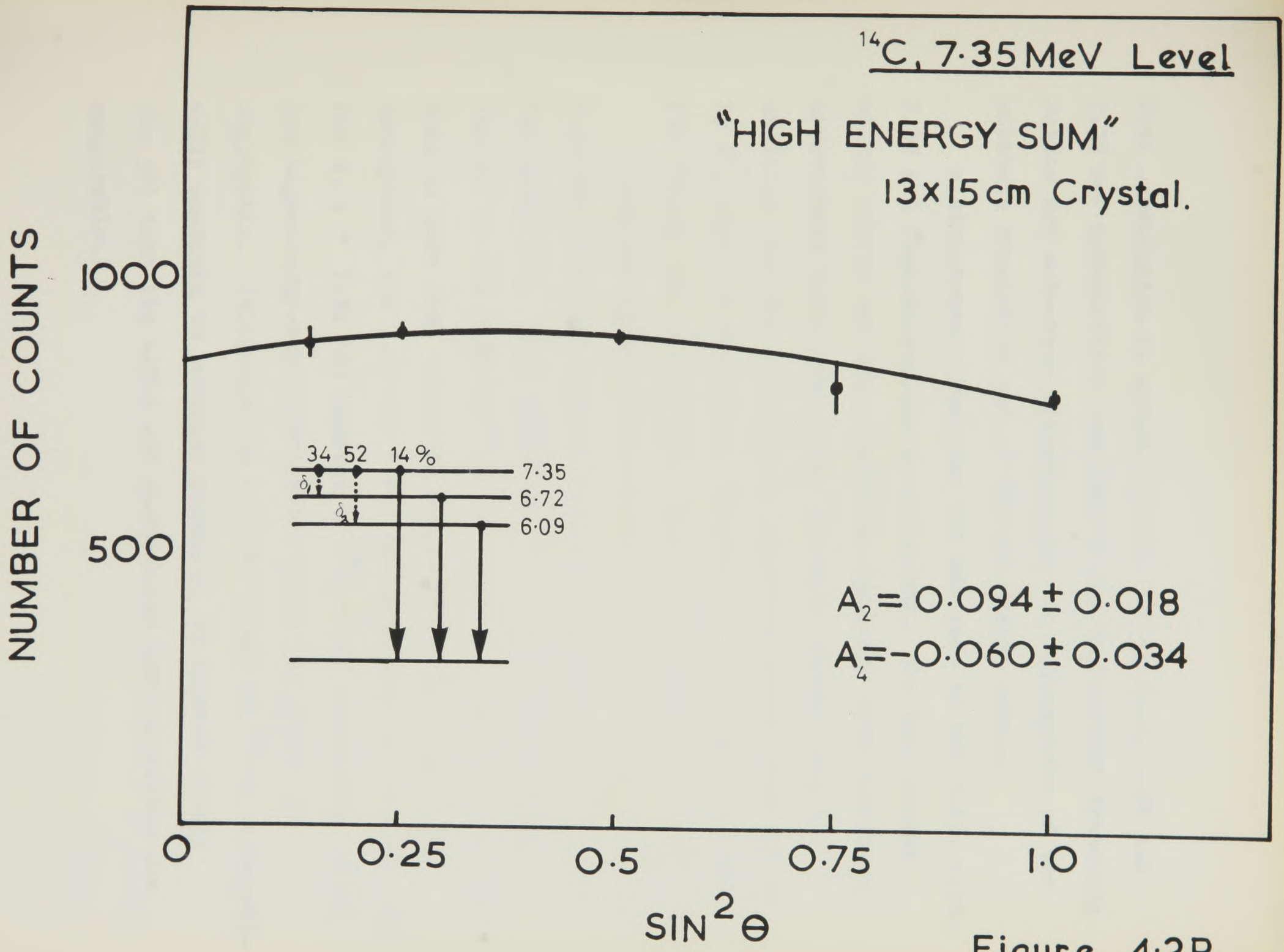

^{14}C, 7·35 MeV Level
"HIGH ENERGY SUM"
13×15 cm Crystal.
NUMBER OF COUNTS
1000
500
0
0·25
0·5
0·75
1·0
SIN$^2\theta$
34 52 14 %
7·35
6·72
6·09
$A_2 = 0.094 \pm 0.018$
$A_4 = -0.060 \pm 0.034$

Figure 4·2P

This correlation is simply the sum of the 6.09, 6.72 and 7.35 MeV correlations weighted by the appropriate branching ratios and detection efficiencies. It is a function of the substate population and of the two mixing ratios.

A simultaneous computer fit was made to the 0.63, 1.26, 7.35 and high-energy-sum correlations. The two unknown mixing ratios and the population parameter were varied in appropriate steps over their physical ranges, and, in addition, the two independent branching ratios were varied by ± 1 standard deviation. The minimum χ^2 was obtained for δ(0.63 MeV) = 0.07 ± 0.3, and δ(1.26 MeV) = -0.04 ± 0.09.

Particle window contamination of about 7% by the ^{18}O, 7.13 MeV level was deduced from the appearance of the 1.98 MeV gamma ray. This level has J = 4 and decays equally (Go 59) to the 3.55 and 1.98 MeV states. Low-energy correlations have been corrected for higher energy gamma ray background, the 7.35 MeV level is unaffected by it, and only the 7.13 → 1.98 MeV cascade in ^{18}O could appreciably enter the high-energy-sum correlation, where its effect is negligible. (Although the 7.13 MeV level of ^{18}O is energetically unstable to particle emission, it appears likely (Go 59) that its alpha and gamma decay partial widths are comparable.)

"Now, what I want is, Facts . . . Facts alone are wanted in life."

Charles Dickens.

CHAPTER 5

NEUTRON-GAMMA ANGULAR CORRELATIONS : ^{18}Ne and ^{19}Ne

5.1 Introduction

The nucleus ^{18}Ne was chosen for study using the neutron-gamma coincidence technique for two reasons. (i) There has recently been some success in explaining the observed properties of ^{18}O with the shell model, by including intrinsic deformed states in the wavefunctions (Sh 68), so that a comparative study of the mirror nucleus ^{18}Ne appeared worthwhile. (ii) The first and higher excited states of ^{18}Ne are sufficiently well separated for it to be possible by choice of beam energy to study initially the first state alone, and then at a higher beam energy the higher states. The negative reaction Q-value (Q = - 3.199 MeV) (Tow 61) assisted this discrimination, and the instability of ^{18}Ne to proton emission at an excitation of 3.921 MeV made it unlikely that population of the states at 3.4 - 3.6 MeV excitation by cascades from higher levels would be a problem. The level schemes of ^{18}O and ^{18}Ne are shown in fig. 5.2A. Information on ^{18}O is from references (Lo 66; Ol 65a; La 68)

The nucleus ^{19}F has received wide experimental and

theoretical attention, and there has been considerable success in understanding its properties (e.g., see Th 66). So, as with ^{18}Ne, the mirror nucleus ^{19}Ne should provide a further check on the theoretical picture. The lifetimes of the fourth, fifth, sixth and seventh ^{19}Ne states have (Ba 70) recently been measured using the ^{19}F(p,mγ)^{19}Ne and ^{16}O(α,mγ)^{19}Ne reactions and it appeared a useful extension of the neutron-gamma coincidence technique to study the decay schemes and angular distributions of the ^{19}Ne gamma rays.

5.2 ^{18}Ne Results

5.2. 1 Level Positions and Decay Schemes

Bound states of ^{18}Ne at 1.88, 3.36 and 3.61 MeV were established using the neutron threshold technique by Towle and Macefield (Tow 61), while further unbound levels have more recently been identified at 4.59 and 5.1 MeV (Tow 68; Bry 64; L'Ec 69). That the ground and first excited states have $J^{\pi} = 0^+$ and 2^+ respectively has been established from (^{3}He,n) double stripping angular distributions (Kr 66; Tow 68). This is in agreement with the mirror nucleus ^{18}O (fig. 5.2A). To further the latter analogy, one would expect a triad of states near 3.5 MeV (the mirror states of

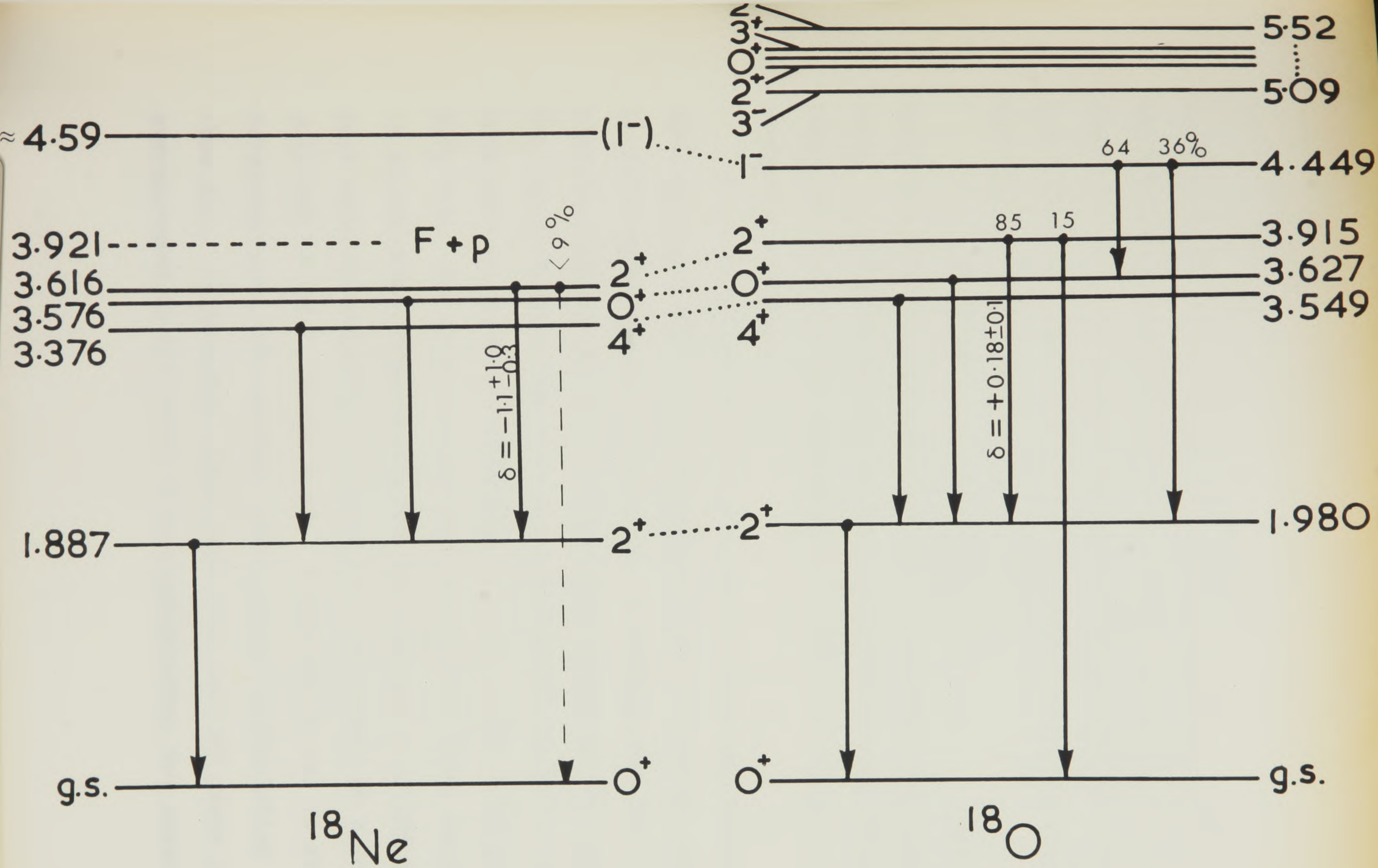

≈ 4·59
(1⁻)
3·921
F + p
3·616
3·576
3·376
2⁺
0⁺
4⁺
< 9 %
δ = −1·1 +1·9 −0·3
1·887
2⁺
g.s.
0⁺
18Ne
3⁺
0⁺
2⁺
3⁻
5·52
5·09
1⁻
64
36%
4·449
2⁺
85
15
3·915
0⁺
3·627
4⁺
3·549
δ = +0·18±0·1
2⁺
1·980
0⁺
g.s.
18O

Figure 5·2A

the 4^+, 0^+, 2^+ levels at 3.55, 3.33 and 3.92 MeV in ^{18}O) and a 1^- level near 4.5 MeV (the mirror of the ^{18}O, 4.45 MeV state). Two of the mirror triad in ^{18}Ne will be the 3.36 and 3.61 MeV states, and it appears that the 4.59 MeV state has indeed $J^\pi = 1^-$ (L'Ec 69; Tow 68).

The existence of the third member of the $\sim$ 3.5 MeV triad was not established in neutron time-of-flight experiments, suggesting that it is weakly excited in the (^3He,n) reaction and/or lies close (within 50 keV say) to one of the other two members.

Neutron-coincident Ge(Li) detector gamma ray spectra were accumulated to good statistics under conditions similar to those described in section 4.2. 4, except that the neutron detector was 18.4 cm from the target (at 0^o) and the Ge(Li) counter was 8 cm from the target (at 90^o). Gamma rays were observed with energies of 1.49, 1.69, 1.73 and 1.89 MeV. The last of these was clearly the first excited to ground state transition, and the 1.49 and 1.73 MeV gamma rays were identified as transitions from levels at 3.38 and 3.62 MeV to the 1.89 MeV level. These values are in good agreement with the previous level energy determination (Tow 61). It appeared likely that the 1.69 MeV gamma ray corresponded to the decay of the anticipated, but missing,

third member of the triad, which would then have an energy of 3.58 MeV.

Four tests were carried out to ensure that the 1.69 MeV gamma ray was not an ^{18}F gamma ray (from $^{16}O(^{3}He,p)^{18}F$) of the same energy, resulting from cascade decay of the ^{18}F, 3.79 MeV level, which might appear in the spectrum through possibly incomplete gamma rejection in the pulse shape discrimination circuits. (These tests were carried out in collaboration with B.C. Robertson (Ro 69) during the lifetime experiments.)

(i) An ^{88}Y source was placed near to the target and was strong enough for its 1.84 MeV line to be much higher than the 1.69 MeV line in the singles spectrum. Within the neutron detector's energy resolution the ^{88}Y source has a similar cascade decay to that of the ^{18}F level. Since the ^{88}Y, 1.84 MeV gamma ray did not appear in the neutron-gamma coincidence spectrum, although the 1.69 MeV line did, it was concluded that the latter was in true coincidence with neutrons.

(ii) Neutron-gamma coincidence spectra at 9, 10, 11 and 12 MeV, normalised to total charge, showed similar

excitation functions for the presumed ^{18}Ne triad at 3.38, 3.58 and 3.62 MeV (yield increasing with energy). On the contrary the intensity of the singles spectrum 1.69 MeV line decreased with increasing energy, suggesting a different origin for the major part of this line.

(iii) At a beam energy of 12 MeV neutrons from the 1.48 MeV state have an energy of $\sim$ 4.5 MeV. The neutron detector discrimination threshold was raised to $\sim$4.5 MeV (using the Compton electron edge of the ^{88}Y, 1.84 MeV gamma ray) whereupon the 1.48, 1.69 and 1.73 MeV gamma rays disappeared together from the neutron-coincident Ge(Li) spectrum, though the 1.89 MeV line remained.

(iv) A neutron-gamma-gamma triple coincidence experiment was attempted with the following geometry: Ge(Li) counter 2.5 cm from the target, at 90°; 7.6 cm x 7.6 cm NaI(Tl) counter opposite at 95° and 3 cm from the target; and the neutron counter 4.4 cm from the target, at 0°. A narrow window on the NaI(Tl) spectrum just encompassed the 1.89 MeV photopeak region. Figure 5.2B shows the triple-coincidence Ge(Li) spectrum (minus randoms) after 36 hours accumulation with a 1mA beam of 12 MeV $^{3}He^{++}$ on the

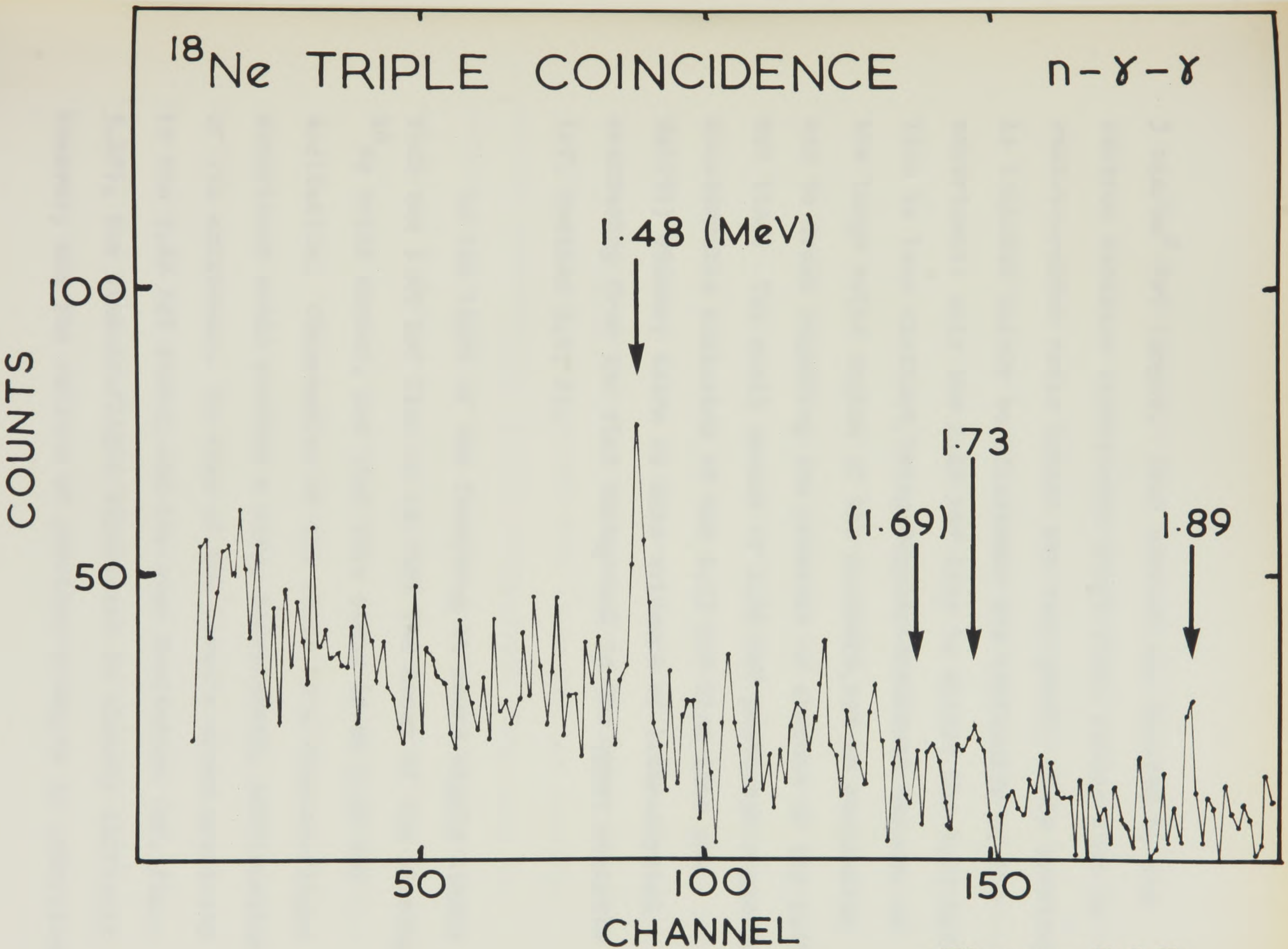

^{18}Ne TRIPLE COINCIDENCE
n-γ-γ
1.48 (MeV)
1.73
(1.69)
1.89
100
50
COUNTS
50
100
150
CHANNEL

Figure 5·2B

3 mgm/cm^2 SrO target. Beam current was limited by the neutron detector electronics count rate, rather than by real-to-random ratio (which was very good). This spectrum is included mainly to illustrate the difficulty of the experiment: only the 1.48 MeV line is clear; the 1.73 MeV line is less distinct, being Doppler-broadened because of the large solid angles of the counters, and no conclusion can be drawn regarding the presence or absence of the 1.69 MeV line. The small amount of 1.88 MeV photopeak suggests considerable inclusion of the 1.73 MeV line into the NaI(Tl) window; there is also evidence of inter-crystal scattering from the flat background in the upper channels (cf. section 5.2. 2).

In the light of the foregoing it seems highly likely that the 1.69 MeV line is in fact the decay of the missing ^{18}Ne triad member, and that this state is at 3.58 MeV excitation. Observation of the state in a time-of-flight experiment would provide a nice, independent, confirmation of its existence. In view of the level's close proximity to the 3.62 MeV state, and its weak excitation (cf. fig. 5.2F), the time-of-flight experiment is clearly difficult however, and the failure of previous attempts is understood.

It was of considerable interest to determine which levels, if any, of the ^{18}Ne triad decayed also to the ground state. Observation of that branch would identify the $J^{\pi} = 2_2^+$ member since only that would decay to the 0_1^+ ground state ($0_2^+ \rightarrow 0_1^+$ impossible, and $4_1^+ \rightarrow 0_1^+$ too slow to compete with $4_1^+ \rightarrow 2_1^+$). A neutron-gamma coincidence spectrum was accumulated in a 7.6 cm x 7.6 cm NaI(Tl) crystal placed 8 cm from the target at an angle of 55°. The beam energy was 12 MeV. The 3.38 and 3.62 MeV levels were seen to decay exclusively to the 1.89 MeV first excited state. From the NaI(Tl) spectrum (fig. 5.2C) an upper limit of 4% was placed on the ground state transition of the 3.38 MeV level. No attempt was made to correct this limit for the possible angular distribution of the (unobserved) gamma ray: the choice of $\theta = 55°$ for the NaI(Tl) crystal eliminated the effect of the P_2 term in the distribution since $P_2 \sim 0$ at this angle. After determining the relative intensities of the 1.49, 1.69, 1.73 and 1.89 MeV lines from a Ge(Li) spectrum simultaneously accumulated (also with this counter at 55°), upper limits of 17% and 9% could be placed on the ground state transitions from the 3.58 and 3.62 MeV levels, respectively. Ge(Li) and NaI(Tl) counter photopeak efficiencies were taken from (La 67; Ja 62; An 68).

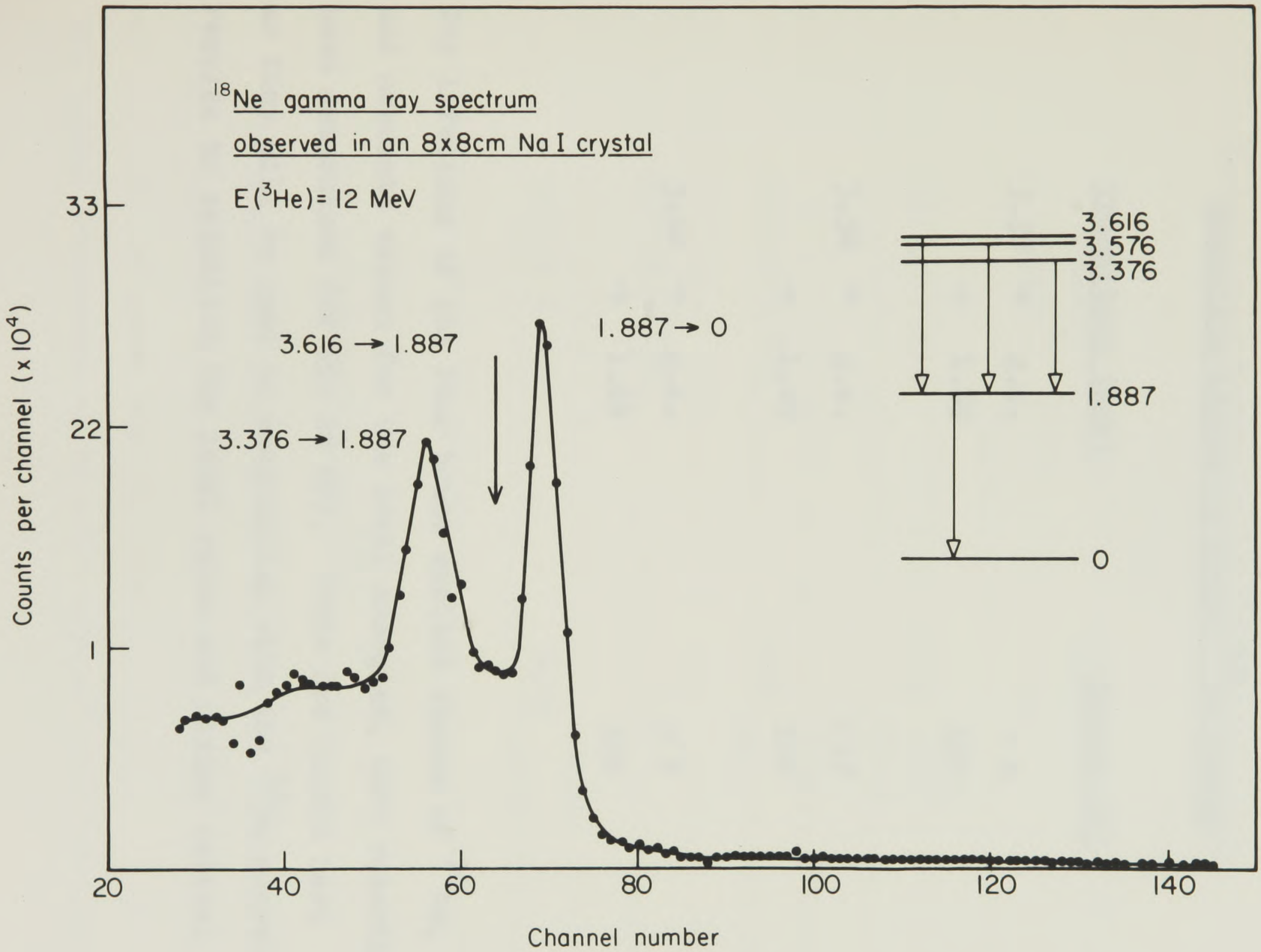

18Ne gamma ray spectrum
observed in an 8x8cm Na I crystal
E(3He)= 12 MeV
3.616 → 1.887
1.887 → 0
3.376 → 1.887
3.616
3.576
3.376
1.887
0
Counts per channel (x 10^4)
33
22
1
20
40
60
80
100
120
140
Channel number

Figure 5·2C

TABLE 5.2A

Branching Limits of Bound ^{18}Ne States

Transition (MeV)			Branch (%)
3.38	→	g.s.	< 4
	→	1.89	100
3.58	→	g.s.	< 17
	→	1.89	100
3.62	→	g.s.	< 9
	→	1.89	100

The lifetimes of the four bound excited states of ^{18}Ne, and accurate values for the level energies, have recently been determined (Gi 68; Ro 69). These are quoted here as they will be used in conjunction with the ^{18}Ne correlation results to establish the level spins and mixing ratios:

TABLE 5.2B

Energies and Lifetimes of ^{18}Ne Bound States

Energy (MeV)	Lifetime (ps)
1887.3 ± 0.2	$0.49^{+0.17}_{-0.09}$
3376.2 ± 0.4	$1.90^{+0.7}_{-0.4}$
3576.3 ± 2.0	> 2
3616.4 ± 0.6	$0.06^{+0.03}_{-0.02}$

5.2. 2 The 1.89 MeV level of ^{18}Ne

The experimental and electronic set up has been broadly described in section 2.2. The angular distribution of the 1.89 MeV gamma ray was measured using a $\sim$ 200 μgm/cm^2 WO_3 target evaporated on to a 100 mgm/cm^2 gold backing, which

also served as a beam stop. The $\sim$ 50 nA, $^3He^{++}$ beam at 8.50 MeV was provided by a Van de Graaff accelerator at A.W.R.E. Harwell. The reaction kinematics and neutron detector energy threshold were such that only direct-population 1.89 MeV level gamma rays would be seen in coincidence at this beam energy.

A 7.6 cm x 7.6 cm NaI(Tl) crystal was used as gamma detector at a distance of 17 cm from the target, with the 13 cm x 15 cm NE213 neutron detector 30 cm from the target at 0^o. Real and random neutron-gamma coincidence spectra were stored in the two halves of the kicksorter, the random coincidences being later subtracted appropriately. Each spectrum was normalised to the total number of neutrons detected during that run. As all neutrons above the ($\sim$ 1.5 MeV) energy threshold were indistinguishable, the number of neutrons associated with the 1.89 MeV state could not be directly measured. Therefore the ratio of total gamma yield to total neutron yield, and the total neutron yield per unit beam charge, were also recorded to monitor possible contamination build-up, possible changes in the target yield, and possible changes in the ratio of ground to first excited state neutron detection efficiency. Both measured quantities remained constant during the experiment

indicating that it was reliable to normalise the spectra to total neutrons.

The sum of the correlation spectra is shown in fig. 5.2D. The flat high energy background was evident only in those runs for which the NaI(Tl) crystal was close to the neutron detector. It was probably largely due to the excitation of the ^{12}C, 4.44 MeV state by inelastic scattering of fast neutrons in the NE213 scintillation. This background was subtracted from the 1.89 MeV peak by linear extrapolation. Some runs were taken at backward angles: they were free from the background and confirmed the forward-angle correlation.

The suggestion of a double photopeak at $\sim$ 0.95 and $\sim$ 1.05 MeV was probably due to cascade gamma rays from the 0.94 and 1.05 MeV levels of ^{18}F, produced by the $^{16}O(^{3}He,p\gamma)^{18}F$ reaction, and entering the NaI(Tl) crystal in coincidence with gamma rays cascading from higher levels. In this early experiment the neutron-gamma discrimination was not as efficient as for the other experiments described here. However examination of the ^{18}F decay scheme (Po 65) shows no cascade gamma rays of between 1.70 and 2.09 MeV energy from states below 3.4 MeV so that the ^{18}Ne, 1.89 MeV photopeak would be free from contamination, and counts in this

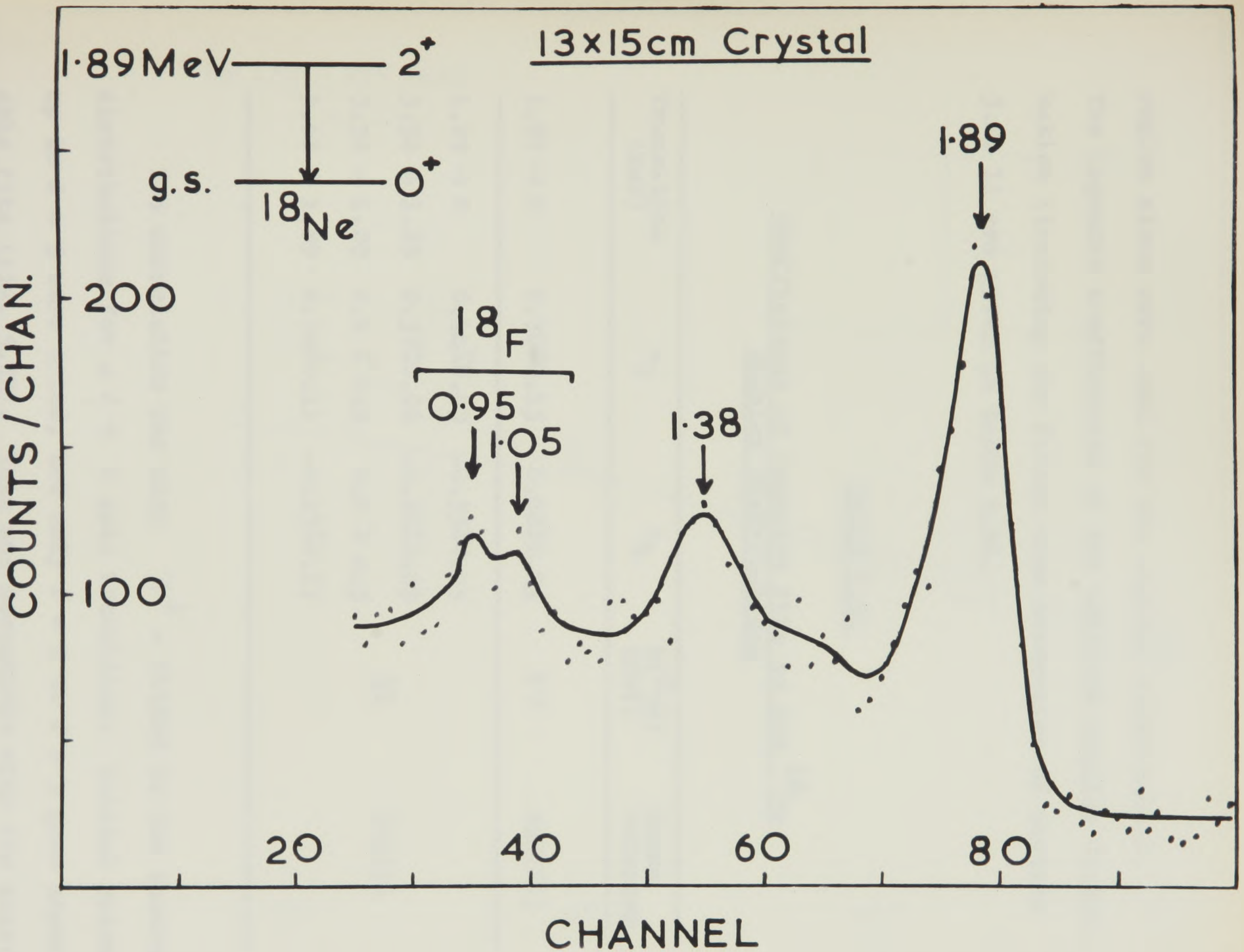

13x15cm Crystal
1·89MeV
2⁺
g.s.
0⁺
18Ne
1·89
18F
0·95
1·05
1·38
200
100
COUNTS / CHAN.
20
40
60
80
CHANNEL

Figure 5·2D

region alone were used for the angular distribution. The Legendre coefficients of the measured angular distribution (including the finite size correction of section 3.2. 1) are given in table 5.2C.

TABLE 5.2C

Coefficients of Legendre fits to the ^{18}Ne Angular Distributions

Transition (MeV)	A_2	A_4	$E(^3He)$ (MeV)	Gamma Detector
1.89 → 0	0.70±0.15	0.02±0.25	8·5	NaI(Tl)
1.89 → 0	0.44±0.03	-0.33±0.05	12	Ge(Li)
3.38 → 1.89	0.37±0.06	-0.28±0.09		
3.58 → 1.89	0.0 ± 0.3	0.0 ± 0.5		
3.62 → 1.89	0.74±0.11	-0.13±0.17		

The correlation was also χ^2 - fitted to the theoretical distributions for a J → 0 spin transition. Initial spins of up to J = 5 were tried, but only J = 2 or J = 3 gave acceptable fits (fig. 5.2E). This was compatible with the existing

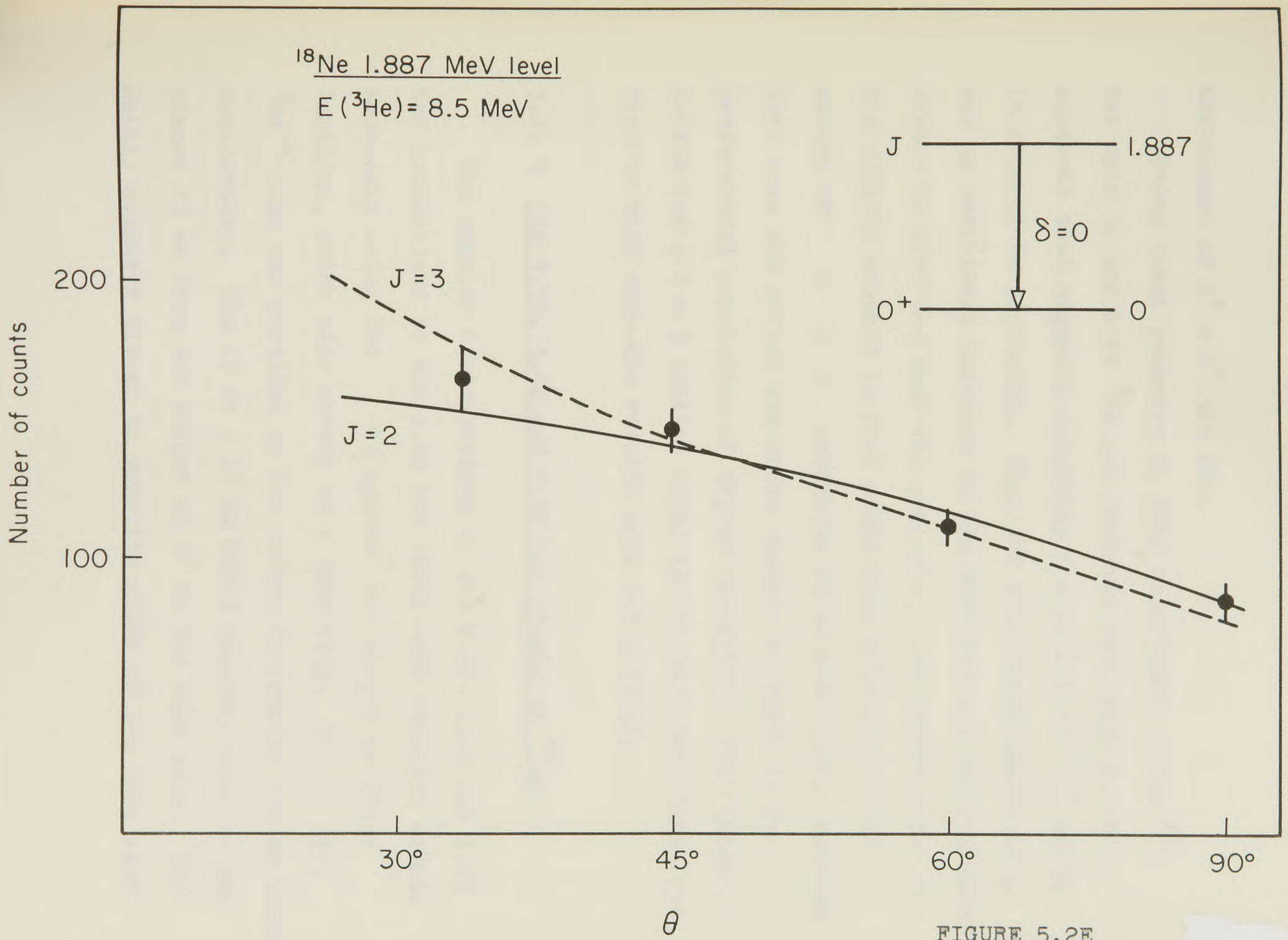

^{18}Ne 1.887 MeV level
E (^{3}He) = 8.5 MeV
J
1.887
δ = 0
0^{+}
0
J = 3
J = 2
200
100
Number of counts
30°
45°
60°
90°
θ

FIGURE 5.2E

assignment of $J^{\pi} = 2^{+}$ (Kr 66).

Using ideal geometry in this experiment, since ^{16}O has spin 0, and both ^{3}He and neutrons have spin $\frac{1}{2}$, it is apparent that magnetic substates m = 0, $\pm$ 1 of ^{18}Ne would in general be populated. Thus the population parameter p was an additional variable in the analysis and was optimised always to give the best fit possible. The finite size of the neutron counter in fact would have allowed a small amount of $m \geqslant 2$ substates to be populated. However this does not affect the above results if there is no preferential population of higher substates. The distribution for a J = 3 initial state is the most sensitive, but even in that case the results were not altered.

5.2. 3 The 3.38, 3.58 and 3.62 MeV Levels of ^{18}Ne

The angular distributions of the 1.49, 1.69 and 1.73 MeV transitions to the 1.89 MeV level were measured simultaneously using the ~ 3 mgm/cm^2 SrO target on thick Tantalum, which also served as a beam stop. The 12 MeV, $^{3}He^{++}$ beam was provided by the Oxford University Van de Graaff Accelerator. The 13 cm x 15 cm NE213 neutron detector was placed 23 cm from the target at 0^{o} to the beam axis. Two Ge(Li) counters placed on opposite sides of the beam line

7 cm from the target were used independently, each accumulating real and random spectra. Photopeak counts were extracted from the randoms-corrected spectra using a linear background subtraction. Normalisation was carried out as described in section 5.2. 2 for the 1.89 MeV level, and two independent angular distributions were measured in this way (the two counters were usually placed at different angles for each run to help remove any bias arising from beam fluctuations, count rate effects, beam focus conditions, etc.). A third angular distribution was measured, keeping one of the Ge(Li) counters in a fixed position and using the 1.89 MeV photopeak counts in that spectrum to normalise the counts in the other spectrum. A typical summed correlation Ge(Li) spectrum is shown in fig. 5.2F.

For each level all three measured correlations agreed well within their errors. Error-weighted averages of the distributions were fitted to Legendre polynomials (fig. 5.2G), and the resulting A_2 and A_4 coefficients (Table 5.2C) were corrected for the finite Ge(Li) counter size (section 3.2. 1). χ^2-fits to the theoretical distributions were carried out assuming the spin of the 1.89 MeV level to be J = 2. In this manner the spin of the 3.38 MeV level was established to be either J = 2 or 4, the spin of the 3.58 MeV level was

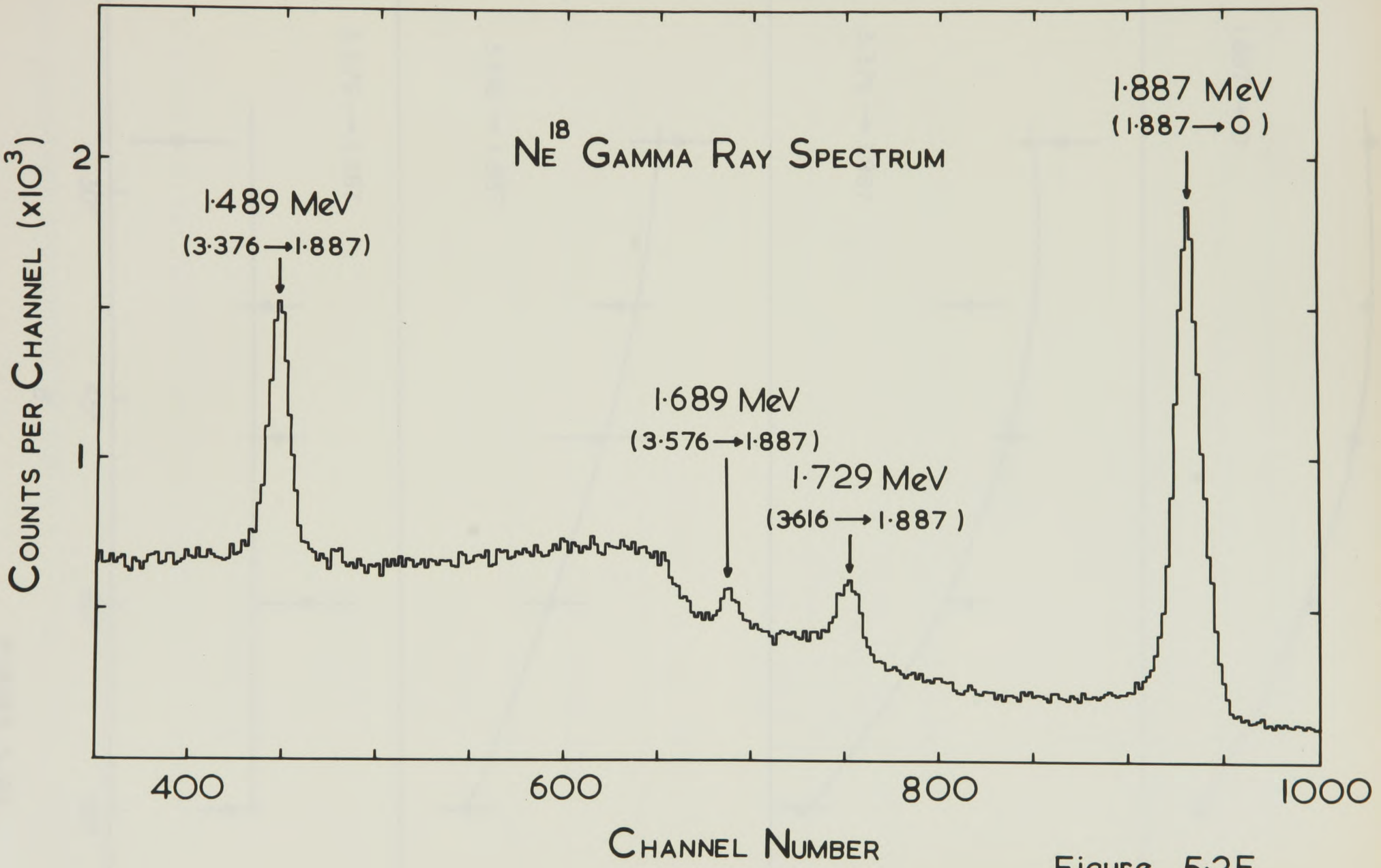

Ne18 Gamma Ray Spectrum
1·887 MeV
(1·887 → 0)
1·489 MeV
(3·376 → 1·887)
1·689 MeV
(3·576 → 1·887)
1·729 MeV
(3616 → 1·887)
Counts per Channel (x10^3)
2
1
400
600
800
1000
Channel Number

Figure 5·2F

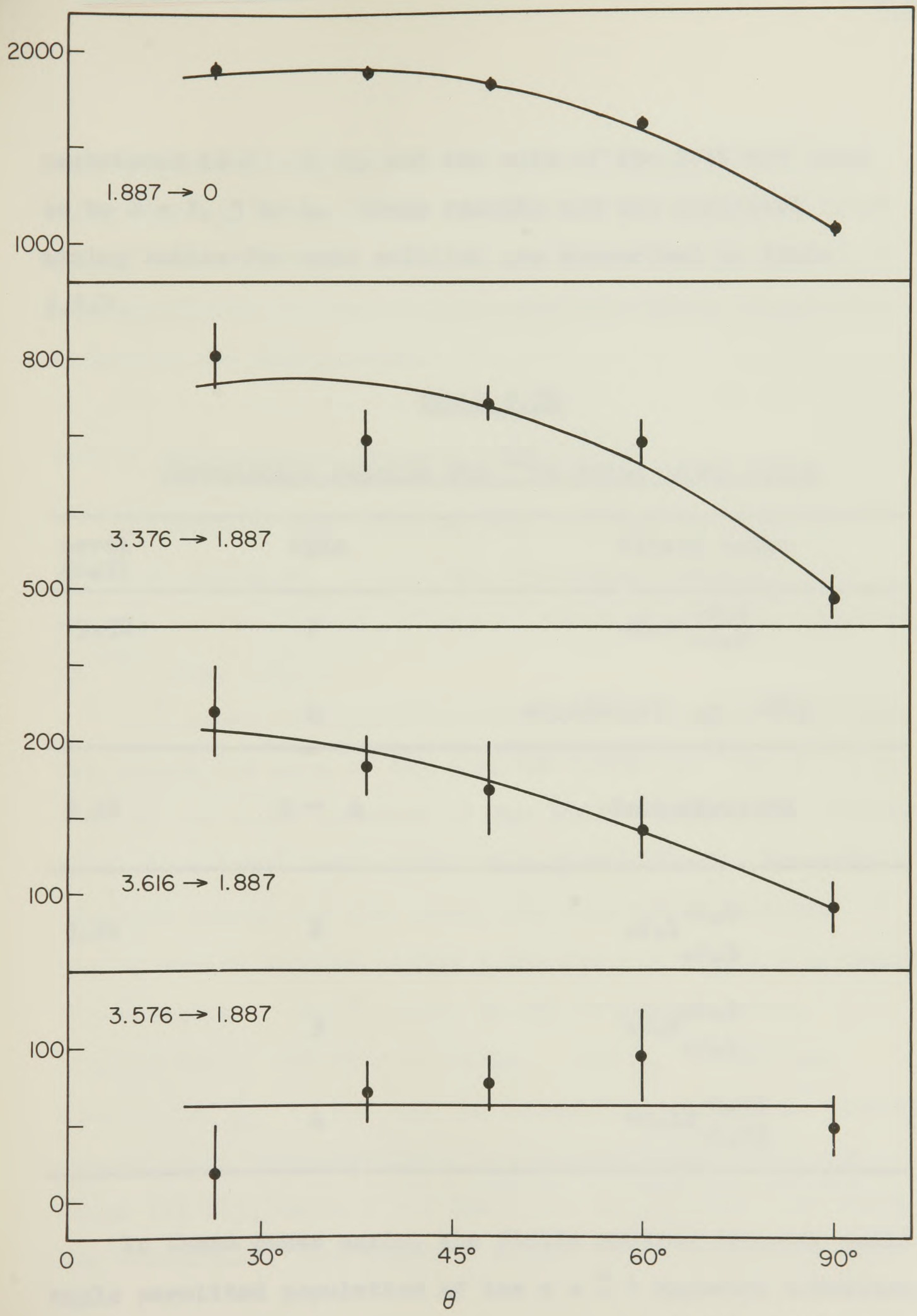

2000
1000
1.887 → 0
800
500
3.376 → 1.887
200
100
3.616 → 1.887
100
0
3.576 → 1.887
0
30°
45°
60°
90°
θ
Number of counts
Number of counts

FIGURE 5.2G

restricted to $J \leq 4$, and the spin of the 3.62 MeV level to be J = 2, 3 or 4. These results and the permitted mixing ratios for each solution are summarised in table 5.2.D.

TABLE 5.2D

Correlation Results for ^{18}Ne triad Level Spins

Level (MeV)	Spin	Mixing Ratio
3.38	2	$-2.6^{+0.9}_{-0.2}$
	4	$+0.06 \pm 0.07$ or $+8 \pm 3$
3.58	$0 \rightarrow 4$	Unconstrained
3.62	2	$-1.1^{+1.0}_{-0.3}$
	3	$-0.9^{+0.2}_{-0.1}$
	4	$+0.12^{+0.07}_{-0.03}$

In these cases again, the finite neutron detector solid angle permitted population of the $m = \pm 2$ magnetic substates.

However the optimisation of the population parameter p makes the χ^2 fits rather insensitive to higher substates (i.e., some compensation is obtained) and it was found that a 5% population of the m = ± 2 substates had no significant effect on the conclusions.

5.2. 4 Experimental Conclusions for ^{18}Ne

In section 5.2. 1 it has been pointed out that the triad of states at ~ 3.5 MeV are almost certainly the analogs to the $J^\pi = 4^+$, 0^+ and 2^+ triad at a similar excitation in ^{18}O (fig. 5.2A).

The measured angular distribution of the 1.73 MeV gamma ray limits the spin of the 3.62 MeV level in ^{18}Ne to J = 2, 3 or 4; the known lifetime of the level (table 5.2B) corresponds to a total decay width of 1.05×10^{-2} eV. Assuming positive parity for the level, the 1.73 MeV transition mixing ratios implied (table 5.2D) for J = 3 or J = 4 require E2 strengths $|M|^2 = 115$ or 295 Weisskopf units, respectively. But if J = 2 then $|M|^2_{E2} < 190$ and $0.03 < |M|^2_{M1} < 0.1$ are the transition strengths. The E2 enhancements necessary for J = 3 or 4 violate the E2 sum rules (Wi 60), hence J = 2 and $\delta = -1.1^{+1.0}_{-0.3}$ for this level and transition. The measured ground state transition limit

(table 5.2A) is compatible with this assignment.

The two remaining ^{18}Ne states must then be $J^{\pi} = 4^+$ and 0^+ (from the mirror arguments). The information from the lifetime measurements (table 5.2B) does not, even when combined with the angular correlation results, enable one to place any restrictions on the J and δ of these two levels, beyond the conclusions of table 5.2D. From this table however it is clear that the 3.38 MeV level does not have J = 0, but may have J = 4, whilst the 3.58 MeV level may have J = 0. Thus we conclude that the 3.58 MeV level has $J^{\pi} = 0^+$ and that the 3.38 MeV level has $J^{\pi} = 4^+$ and $\delta = 0.06 \pm 0.07$ or $\delta = +8 \pm 3$. This latter value may be excluded (Sk 66) since, with the measured lifetime, it would imply a rather extravagant M3 strength ($M^2_{M3} \sim 10^4$). These spin assignments give the same level sequence as is found in ^{18}O, and justify the dotted lines connecting mirror levels of the two nuclei in fig. 5.2A.

5.3 The ^{19}Ne Results

5.3.1 Introduction

The energies and lifetimes of ^{19}Ne states below 2.8 MeV have recently been determined (Bl 69; Ol 67; Gu 68; Ba 70) and are given in table 5.3A.

TABLE 5.3A

Level Positions and Lifetimes in ^{19}Ne

J^{π}	Energy (keV)	Mean Lifetime (ps)	Width (μeV)
$1/2^+$	0.0	-	-
$5/2^+$	238.2 ± 0.2	$(26\pm1) \times 10^3$	-
$1/2^-$	274.9 ± 0.1	< 450	-
$5/2^-$	1507.5 ± 0.2	$4.1^{+3.5}_{-1.4}$	160^{+110}_{-80}
$3/2^+$	1535.7 ± 0.3	$0.028^{+0.015}_{-0.015}$	$(23^{+27}_{-8}) \times 10^3$
$3/2^-$	1614.9 ± 0.2	$0.18^{+0.06}_{-0.05}$	3700^{+1400}_{-1000}
$9/2^+$	2794 ± 1.5	$0.33^{+0.10}_{-0.09}$	2000^{+700}_{-500}

For angular distribution studies of these levels the $^{16}O(\alpha,n\gamma)^{19}Ne$ reaction would be most satisfactory as only $m = \pm 1/2$ magnetic substates would be populated. However the Q-value of this reaction is - 12.16 MeV and even at the highest alpha beam energy available ($\sim$ 19 MeV) the neutron yield was too low for satisfactory correlation studies. Figure 5.3A shows a typical n-γ pulse-shape discriminator time converter output spectrum for this reaction. The target was 500 $\mu gm/cm^2$ WO_3 on a 100 mgm/cm^2 lead backing. It is note-worthy that at this energy roughly 40% of the neutrons came from the lead backing, as was shown by reversing the target.

The $^{19}F(p,n\gamma)^{19}Ne$ reaction, for which Q = - 4.04 MeV, was found to give an adequate yield for the correlation experiments. The ground state of ^{19}F has spin $J = 1/2$ so that ^{19}Ne magnetic substates $m = \pm 1/2, \pm 3/2$ could be populated strongly. The experimental set-up was in all respects very similar to that described already in section 5.2 for the ^{18}Ne correlations.

The ^{19}Ne level scheme is shown in fig. 5.3F. For the study of the $\sim$ 1.5 MeV triplet the proton beam energy was 8.75 MeV, and the target was $\sim$ 10 mgm/cm^2 polytetrafluorethylene on a 200 mgm/cm^2 gold backing, which also served

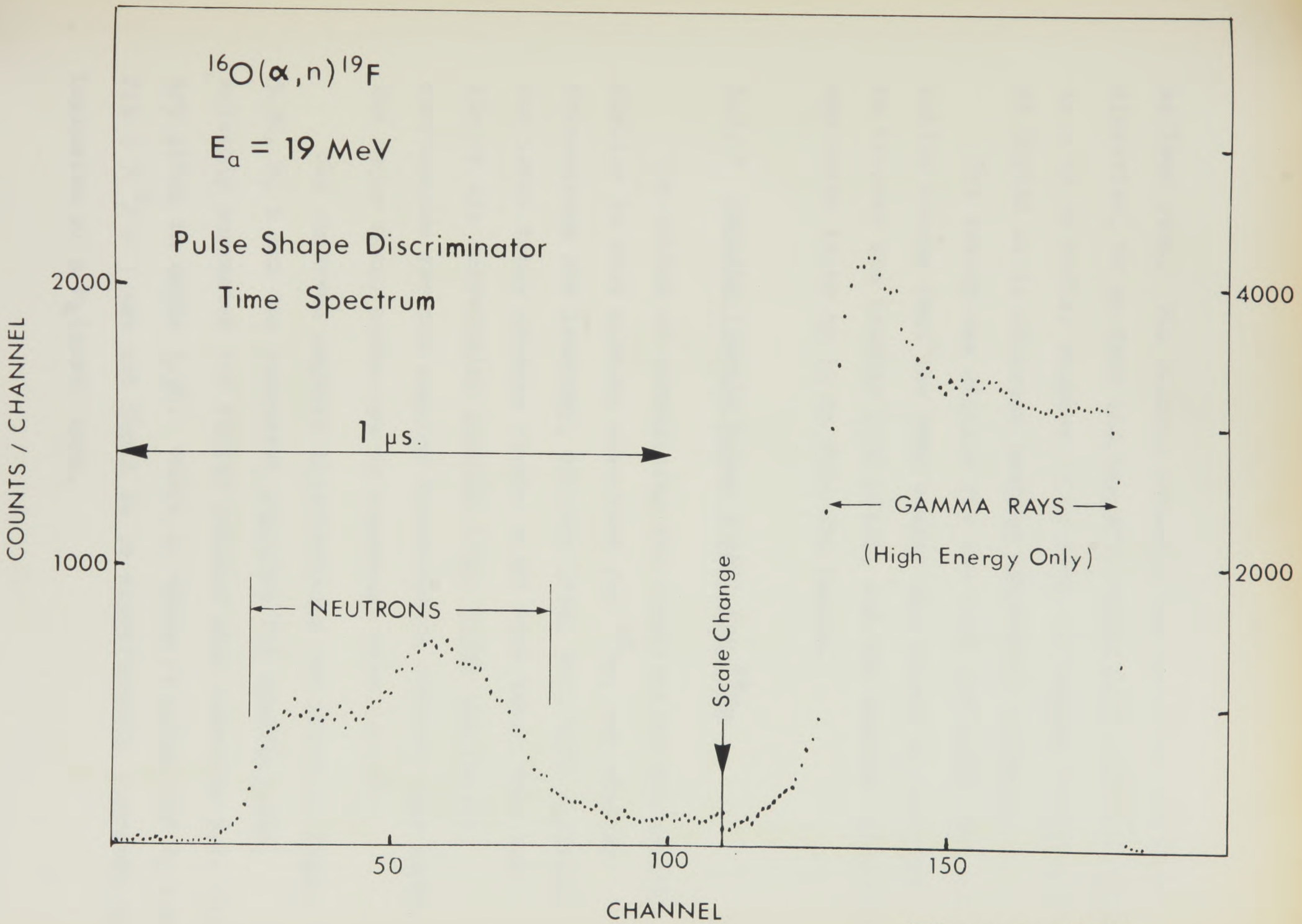

$^{16}O(\alpha,n)^{19}F$
E_a = 19 MeV
Pulse Shape Discriminator
Time Spectrum
2000
1000
4000
2000
COUNTS / CHANNEL
1 μs.
GAMMA RAYS
(High Energy Only)
NEUTRONS
Scale Change
50
100
150
CHANNEL

Figure 5·3A

as beam stop. The neutron detector was at 0^{o} to the beam direction, 20 cm from the target. Gamma rays were detected in a 45 cc Ge(Li) counter, 7 cm from the target (which was so angled as to minimise backing absorption effects).

The set-up was similar for the 2.79 MeV level correlation except that the beam energy was raised to 10.4 MeV to improve the (rather low) yield, and the neutron detector was moved in to be 14 cm from the target.

5.3. 2 Results (Levels below 3 MeV) for ^{19}Ne

The method of normalising the correlations was exactly similar to that already described for ^{18}Ne, and similar corrections for isotropy, counter size, etc. were applied. The level decay schemes (table 5.3B) were taken from the sum of all correlation spectra (fig. 5.3B) and (small) corrections for the angular distribution effects were made. The major decay modes are in agreement with (01 67).

The observed angular distributions are shown in figs. 5.3C, D, E and the extracted Legendre fit coefficients, suitably corrected for finite counter size (section 3.2. 1), are given in table 5.3C. Where no value is given for A_4 the fit (χ^2/ν) was not found to be significantly improved by inclusion of a $P_4(\cos\theta)$ term.

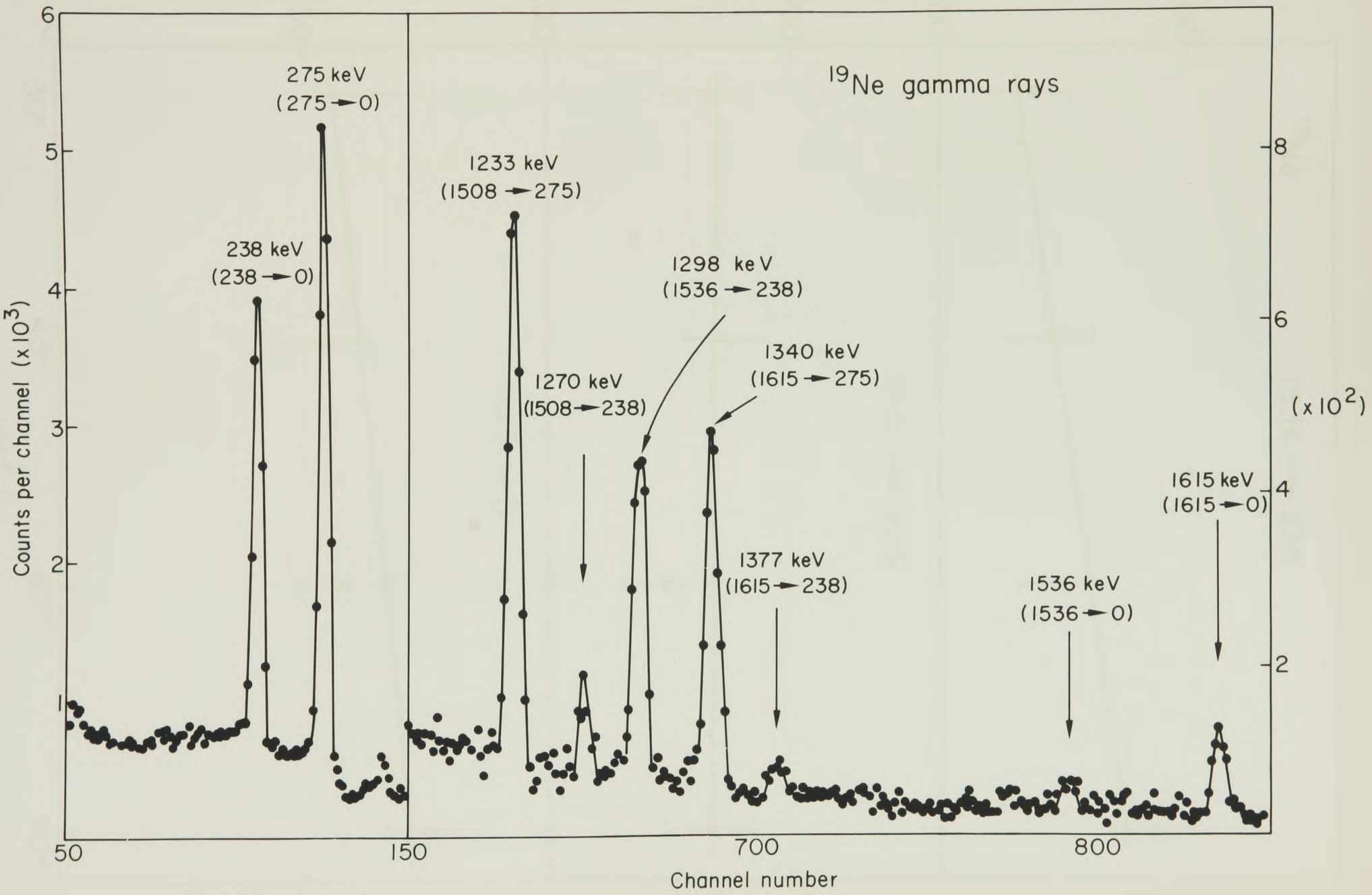

^{19}Ne gamma rays
275 keV
(275 → 0)
238 keV
(238 → 0)
1233 keV
(1508 → 275)
1298 keV
(1536 → 238)
1340 keV
(1615 → 275)
1270 keV
(1508 → 238)
1615 keV
(1615 → 0)
1377 keV
(1615 → 238)
1536 keV
(1536 → 0)
Counts per channel (x10^3)
(x10^2)
Channel number
50
150
700
800
1
2
3
4
5
6
8

FIGURE 5.3B

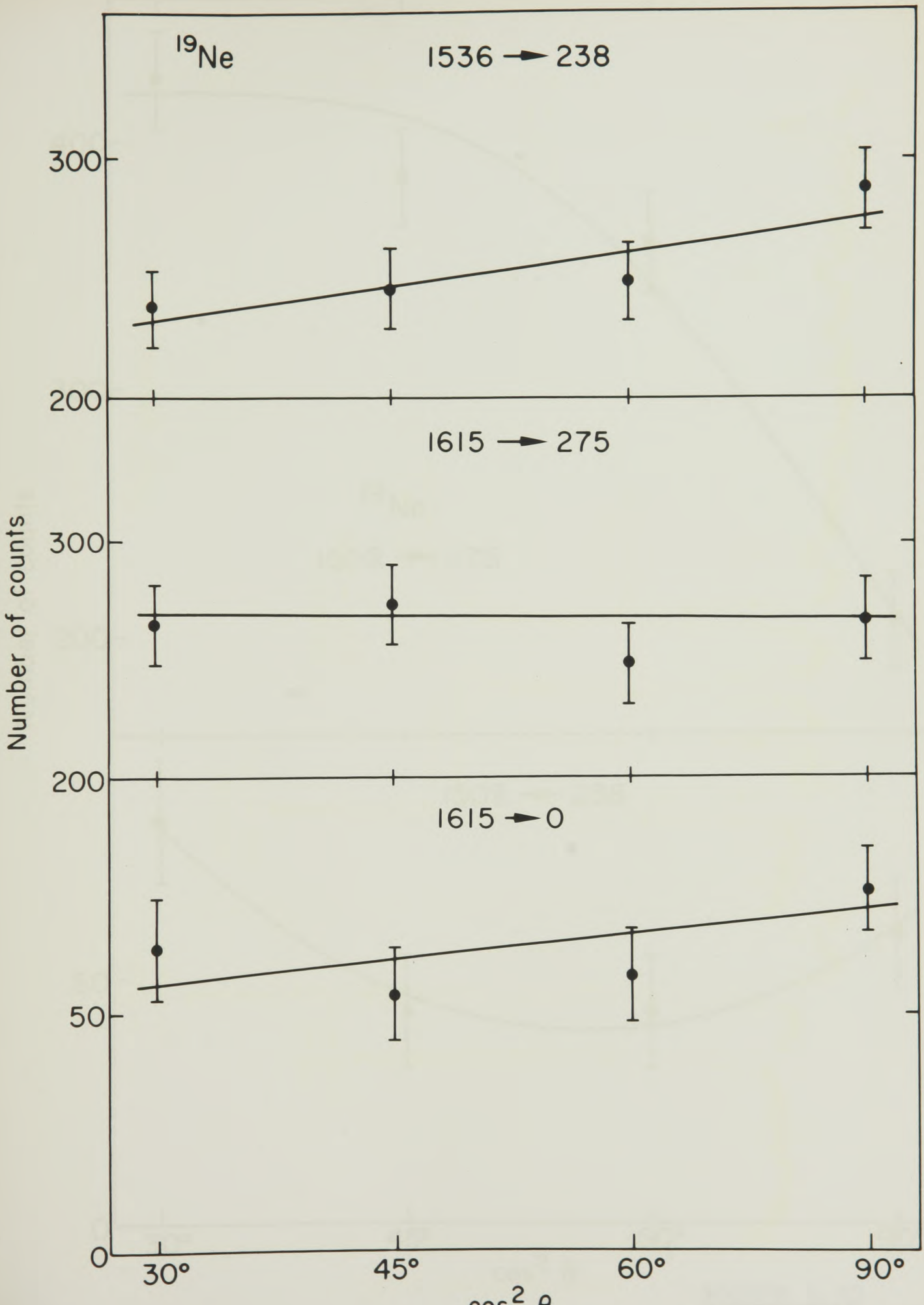

^{19}Ne
1536 → 238
300
200
1615 → 275
300
200
1615 → 0
50
0
Number of counts
30°
45°
60°
90°
cos^2 θ

FIGURE 5.3

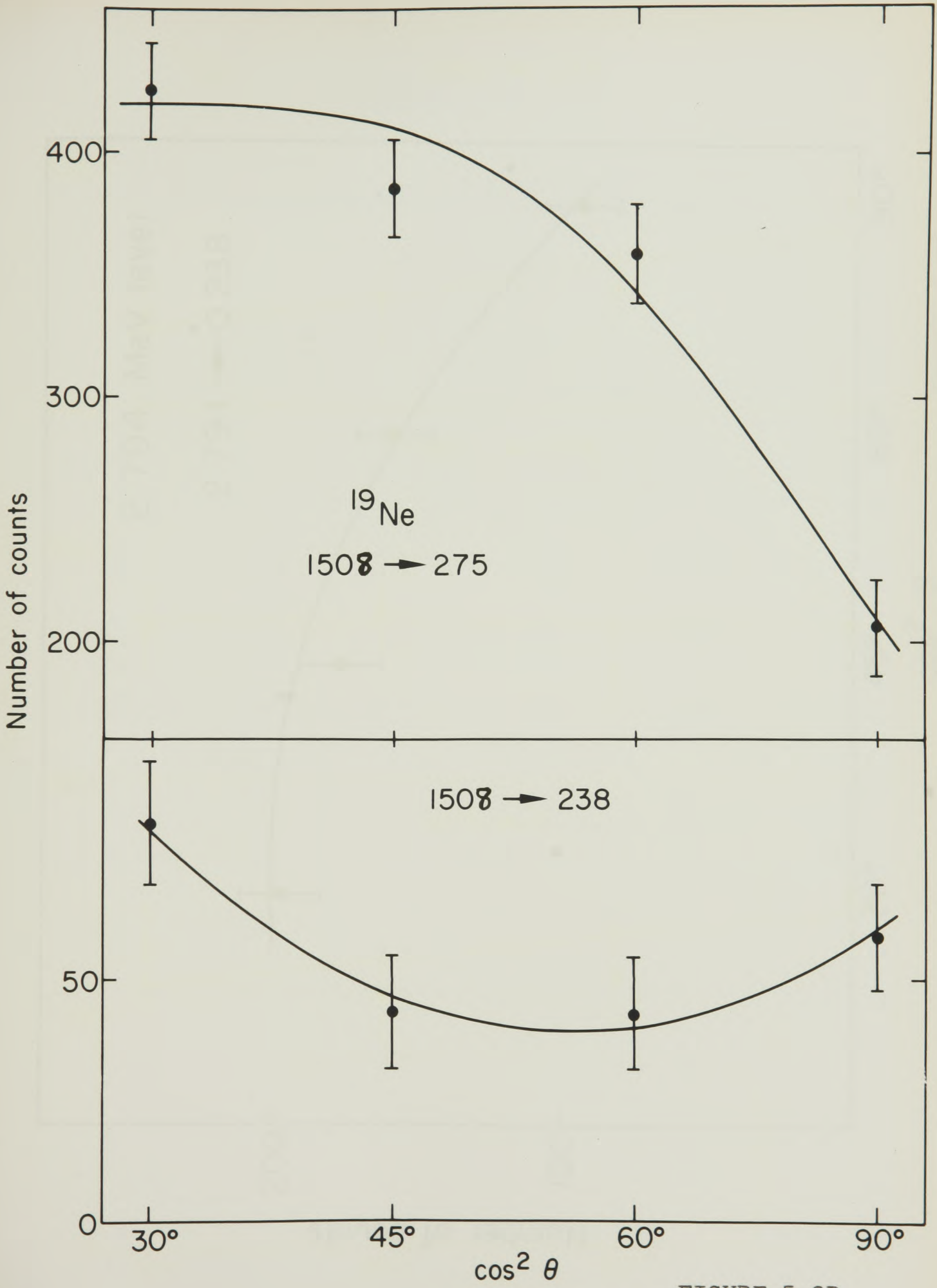

400
300
200
0
50
Number of counts
^{19}Ne
1508 → 275
1508 → 238
30°
45°
60°
90°
cos^2 θ

FIGURE 5.3D

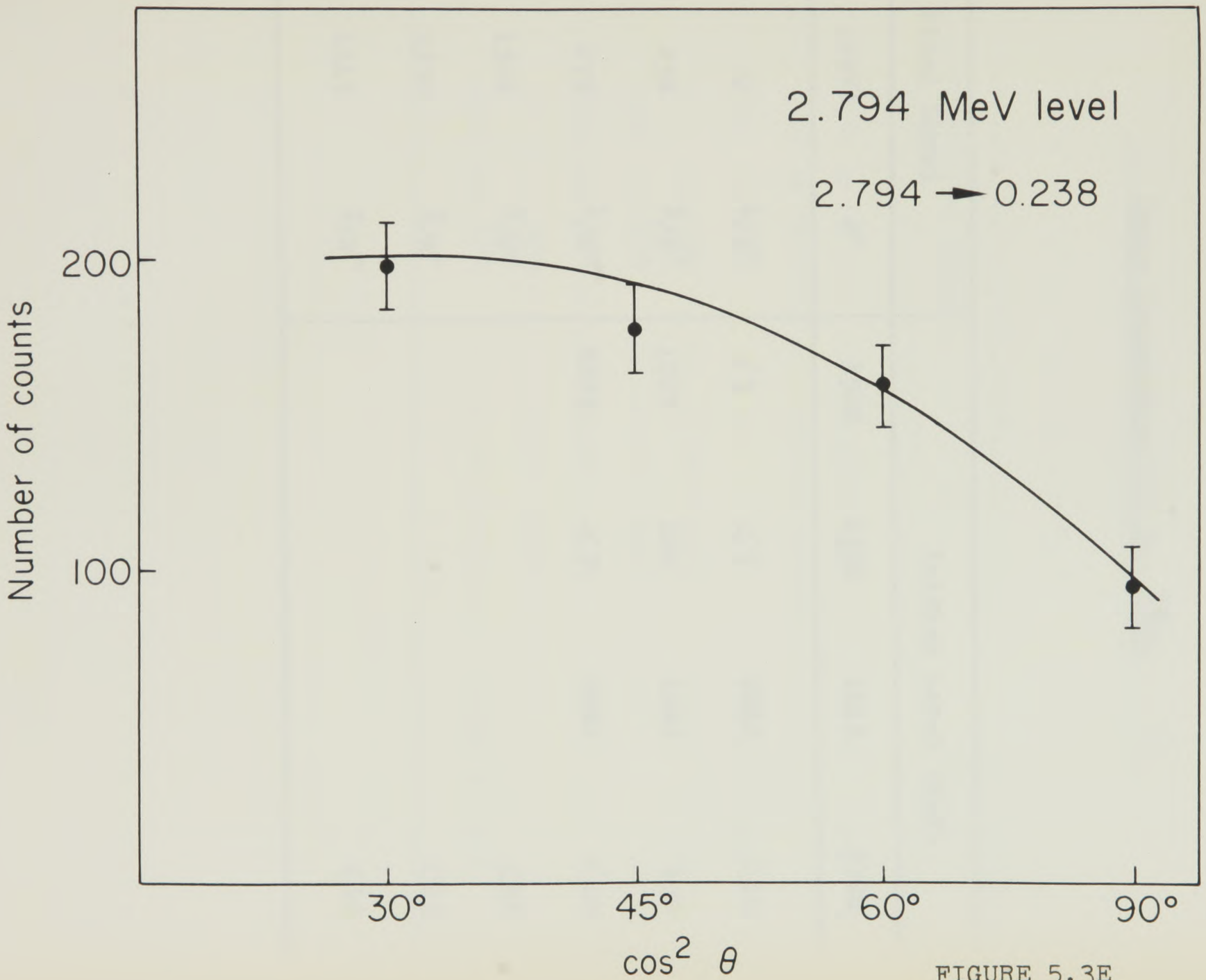

2.794 MeV level
2.794 → 0.238
200
100
Number of counts
30°
45°
60°
90°
cos² θ

FIGURE 5.3E

TABLE 5.3B

Decay Branchings (%) in ^{19}Ne

Final Level		Initial Level (keV)			
(keV)	J^{π}	1508	1536	1615	2794
0	$1/2^+$	<3	<7	20±2	<10
238	$5/2^+$	12±7	100	10±2	100
275	$1/2^-$	88±3	<7	70±2	<10
1508	$5/2^-$				<12
1536	$3/2^+$				<10
1615	$3/2^-$				<10

TABLE 5.3C

Summary of Legendre Coefficients for ^{19}Ne

Transition (keV)	A_2	A_4
238 → 0	0.43 ± 0.04	-0.12 ± 0.05
275 → 0	0.0 ± 0.03	-
1507 → 238	0.5 ± 0.3	+0.85 ± 0.45
→ 275	0.48 ± 0.08	-0.36 ± 0.12
1536 → 238	-0.15 ± 0.08	-
1615 → 0	-0.22 ± 0.20	-
→ 275	0.0 ± 0.08	-
2794 → 238	0.52 ± 0.13	-0.30 ± 0.19

5.3. 3 Conclusions for ^{19}Ne

The energy levels of ^{19}Ne and ^{19}F are shown in fig. 5.3F. Information on ^{19}F is taken from (Ol 66; Th 66; To 68). As was the case for ^{18}Ne, it was found that the angular correlation data alone (even with the lifetimes) did not enable one to directly establish spins and mixing ratios for the levels, and so it has been necessary to lean heavily on mirror level arguments. Fortunately the levels studied fell into distinct energy groups so that the analogies were clear.

The isotropy of the 275 keV level decay was in agreement with the known $J^{\pi} = 1/2^-$ (Bl 69; and further refs. therein) and usefully confirmed the correctness of anisotropy corrections to the other distributions.

The observed A_2 and A_4 coefficients in the decay of the 238keV level were compatible with the known spin-parity ($J^{\pi} = 5/2^+$). No attempt was made to analyse the distribution further as the level was strongly populated by cascade radiation, and also since in view of its long lifetime the correlation may well have been perturbed (Bl 69).

The $\sim$1.5 MeV triplet in ^{19}F have $J^{\pi} = 5/2^-$, $3/2^-$ and $3/2^+$. Only the 1.507 MeV level of ^{19}Ne showed non-zero A_4 coefficients in (both) its decays and this must be the

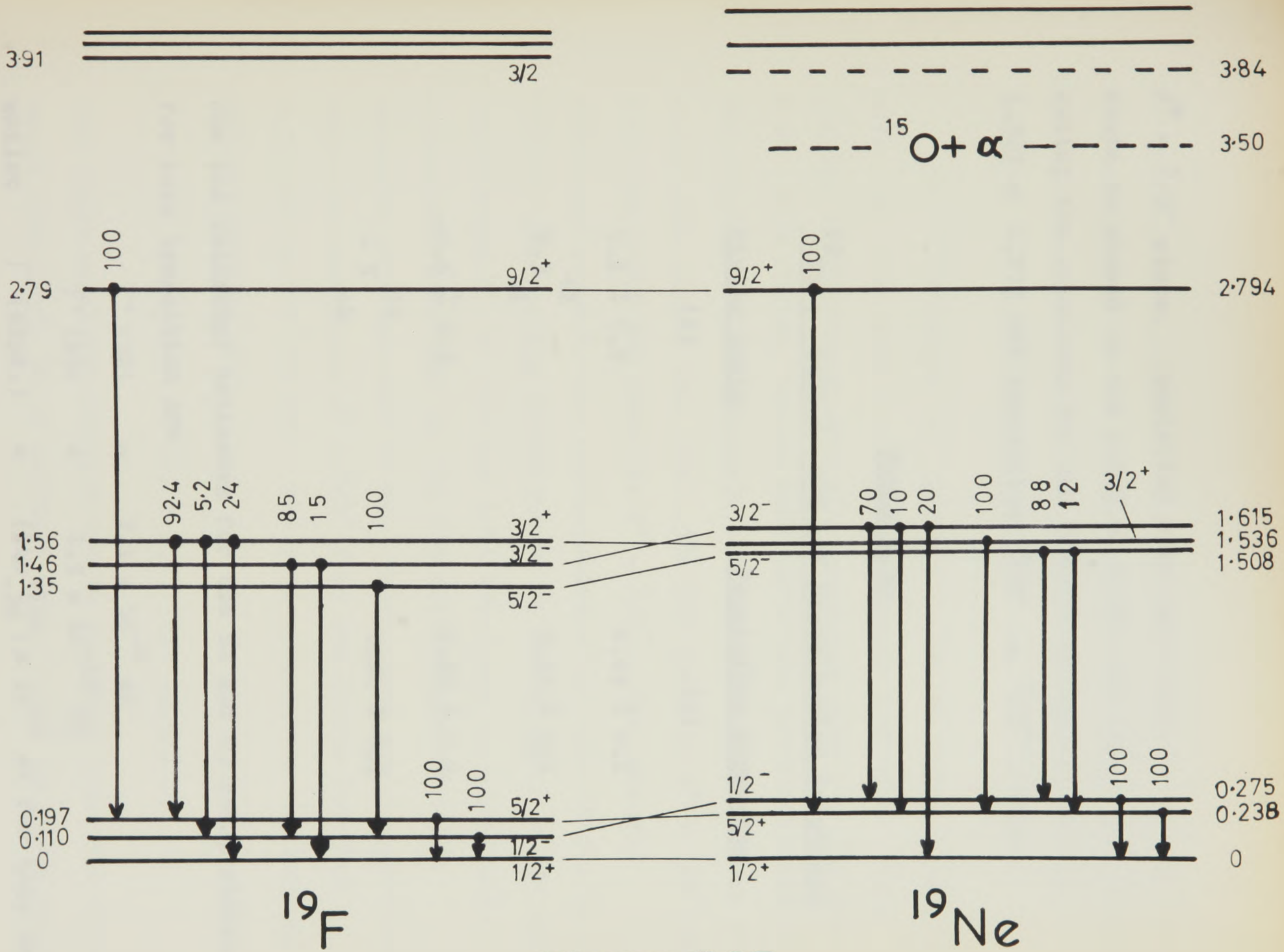

3·91
3/2
3·84
15O+α
3·50
2·79
100
9/2+
9/2+
100
2·794
92·4
5·2
2·4
85
15
100
3/2+
3/2−
5/2−
1·56
1·46
1·35
3/2−
70
10
20
100
88
12
3/2+
1·615
1·536
1·508
5/2−
100
100
5/2+
1/2−
1/2+
0·197
0·110
0
1/2−
5/2+
1/2+
100
100
0·275
0·238
0
19F
19Ne

Figure 5·3F

$J^{\pi} = 5/2^-$ state. Statistics were such that no restriction could be placed on the 1.507 → 0.238 MeV transition mixing ratio; the solutions for the (M3/E2) mixing ratio of the 1.507 → 0.275 MeV transition ($5/2^- \rightarrow 1/2^-$) were :

TABLE 5.3D

^{19}Ne : 1507 → 275 keV Distribution Solutions

Mixing Ratio (δ)	Population Parameter (p)
0.1 ± 0.2	0.85 ± 0.1
2.3^{+2}_{-1}	0.85 ± 0.1
-0.6 ± 0.2	0.28 ± 0.1
-5^{+2}_{-4}	0.28 ± 0.1

Now the Weisskopf estimates for the E2 and M3 decay widths for this transition are

$$\Gamma(E2) = 7.1 \times 10^{-6} \text{ eV}$$

$$\Gamma(M3) = 1.5 \times 10^{-12} \text{ eV}$$

whilst $\Gamma(\text{expt.}) = (140^{+100}_{-70}) \times 10^{-6}$ eV for this branch.

M3 transition strengths rarely exceed 10 W.U. (Sk 66) so that clearly $\delta \sim 0$ is the correct solution. The E2 strength is then $|M|^2 = 20^{+9}_{-8}$ W.U., and is strongly enhanced, as in ^{19}F (La 68).

The ^{19}Ne levels at 1.536 and 1.615 MeV must, by analogy with ^{19}F, both have $J = 3/2$ and opposite parities. The angular correlations were all compatible with $J = 3/2$ for both these states, but no information on the mixing ratio was obtained. By comparison with the ^{19}F decay schemes it would seem likely that the 1.536 MeV level is $J^\pi = 3/2^+$ and that the 1.615 MeV level is $J^\pi = 3/2^-$. The measured lifetimes support this correspondence (Li 63a; Bh 70; La 68). Lastly, the angular distribution of the 2.794 → 0.238 MeV decay shows $J \geqslant 5/2$ for this level and an appreciable quadrupole component in the radiation which from the measured lifetime must be E2. These facts are in agreement with the assignment $J^\pi = 9/2^+$ from the mirror level at 2.79 MeV in ^{19}F (To 68). For this spin-parity the mixing ratio solutions are

$$\delta\,(M3/E2) = 0.0 \pm 0.1 \quad \text{or} \quad -5.6 \pm 2$$

The large negative solution can be excluded since the lifetime would then imply an M3 strength of $\sim 10^7$ Weisskopf units.

The theoretical implications of these ^{19}Ne results will be discussed elsewhere (Ba 70).

'Let's fight till six, and then have dinner',

said Tweedledum.

Lewis Carroll.

CHAPTER 6

NEUTRON-GAMMA COINCIDENCE LIFETIME MEASUREMENTS IN ^{26}Si

6.1 Introduction

^{26}Si is an example of a nucleus easily formed using the (^{3}He,n) reaction, but not so readily reached in other ways. Thus the ^{28}Si(p,t)^{26}Si reaction has Q = - 22.0 MeV and is unsuited to Van der Graaff work, whilst for ^{24}Mg(^{3}He,n)^{26}Si, Q = + 0.095 MeV. Most previous work on the ^{26}Si nucleus has used this latter reaction. Ground state Q-values and excited state energies have been established by time-of-flight (Mc 67; Ha 68; Ad 68), by nuclear emulsion work (Aj 60), from gamma decay data (Ro 68), and by using a Ge(Li) counter as a fast neutron spectrometer (Ni 67). There has been some disagreement as to whether one (Ha 68; Ro 68), or rather two (Mc 67) states exist near 3.8 MeV excitation in ^{26}Si.

Neutron angular distributions imply $J^{\pi} = 0^{+}$ and 2^{+} for the ground and first excited states respectively (Mc 67; Aj 60). Gamma ray angular distributions show J = 2, 2 and 0 for the first three excited states (Ro 68). The above work, and further references to the ^{24}Mg(^{3}He,n)^{26}Si

reaction, have recently been reviewed in greater detail (Ro 68).

Davies et al. (Da 67; Sk 67) studied the reaction $^{28}Si(p,t)^{26}Si$ and observed triton angular distributions from several states (table 6.3A). They assigned $J^{\pi} = 0^+$, 2^+ and 2^+ to the 0, 1.80, and 2.78 MeV levels, and further tentatively assigned $J^{\pi} = 2^+$ to levels at 3.745 and 4.425 MeV.

The mirror nucleus ^{26}Mg has been extensively studied. In a recent paper, where much of the previous literature is reviewed, many lifetime measurements for ^{26}Mg levels are reported (Haü 68).

In the present work, level positions, lifetimes, and decay schemes of ^{26}Si levels are measured, as a further example of the neutron-gamma coincidence technique. A particular benefit of the $^{24}Mg(^3He,n\gamma)^{26}Si$ reaction was that a thick self-supporting isotopically pure ^{24}Mg target could be used, and in the lifetime experiments doubled also as the stopping material. Thus one had high yield and well understood stopping conditions.

Presently available information on ^{26}Mg and ^{26}Si is reviewed in fig. 6.1A (Ha 68; Br 69; Hi 65; Mc 67; Haü 68; Ad 68; Aj 60; Ro 68; Da 67; Sk 67, and this work).

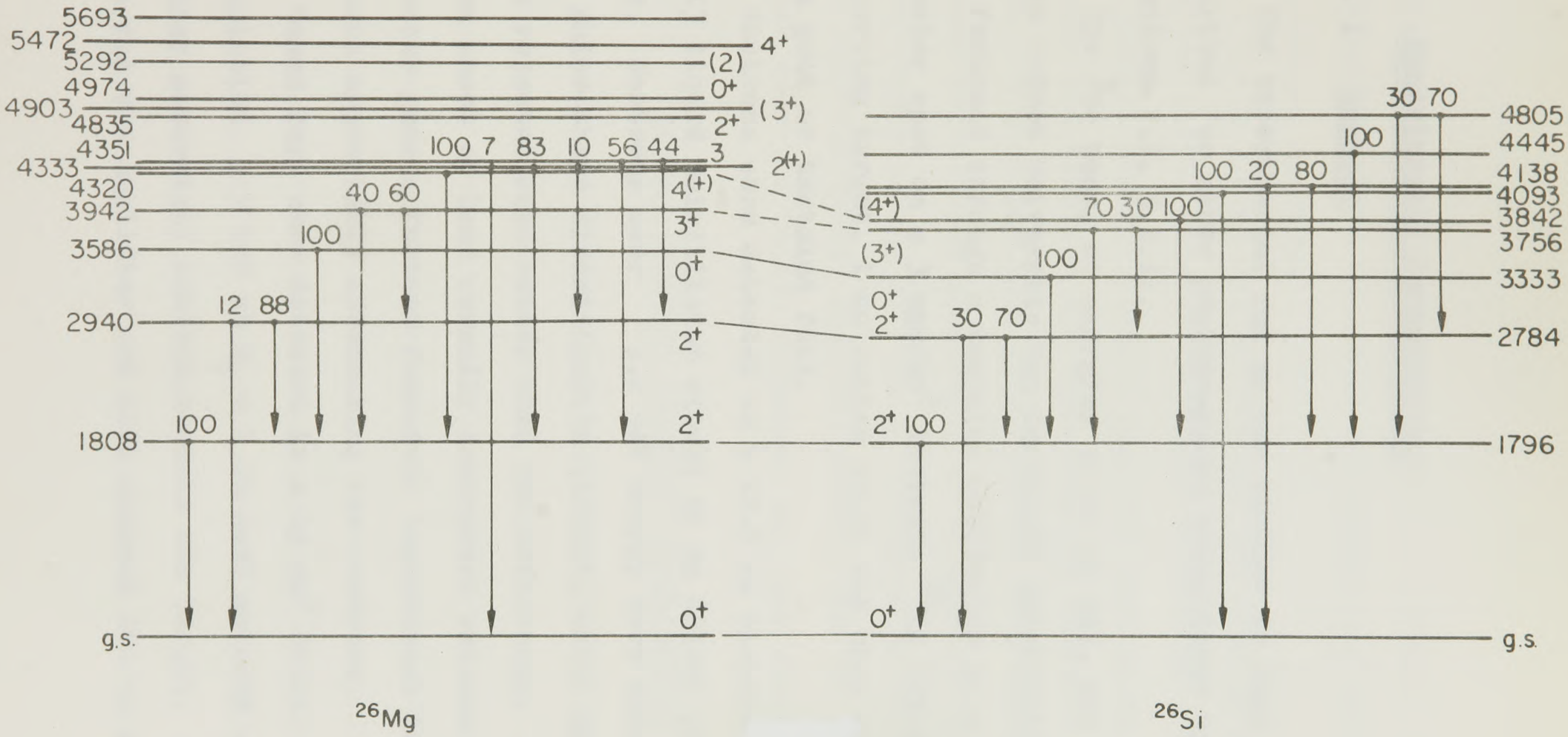

5693
5472
5292
4974
4903
4835
4351
4333
4320
3942
3586
2940
1808
g.s.
4+
(2)
0+
(3+)
2+
2(+)
4(+)
3+
0+
2+
2+
0+
100 7 83 10 56 44 3
40 60
100
12 88
100
^{26}Mg
4805
4445
4138
4093
3842
3756
3333
2784
1796
g.s.
(4+)
(3+)
0+
2+
2+
0+
30 70
100
100 20 80
70 30 100
100
30 70
2+ 100
^{26}Si

Figure 6·1A

6.2 Experimental Arrangements

6.2.1 General

The experimental set up was similar to that already described for other neutron-gamma coincidence experiments (sections 2.2, 5.2.1).

The ^{3}He beam, at energies up to 10 MeV, was supplied by an Oxford University Van der Graaff accelerator, and was focussed through a tantalum collimator to a 3 mm diameter spot on a 3 mgm/cm^2 isotopic ^{24}Mg (99.8%) self-supporting target, 1 mm behind which the beam was stopped in a gold or tantalum foil.

Neutrons were detected in a 12.7 cm diameter by 15.2 cm NE213 liquid scintillator viewed by an XP1040 photomultiplier tube. Neutrons over $\sim$1.2 MeV energy were accepted by the pulse-shape discrimination circuit, while gamma rays were rejected with better than 99% efficiency. A 2.5 cm thick sheet of lead normally interposed between target and detector gave a further four-fold improvement in γ-rejection without appreciably attenuating the neutrons.

Gamma rays were detected in a 45 cm^3 Ge(Li) counter (resolution $\sim$9 keV at E_γ = 1.84 MeV) mounted on a rotating trolley accurately centred beneath the target. Signals were fed via amplifier and 1024 channel ADC to a PDP-7

on-line computer, routed and gated by standard logic circuitry to store both real and random n-γ and/or γ-γ coincidence spectra.

A 7.6 x 7.6 cm NaI(Tl) crystal was used in coincidence with the Ge(Li) counter variously to provide a continuous calibration during lifetime runs (by placing an ^{88}Y source between the counters and observing the 898.04 ± 0.04 and 1836.13 ± 0.04 keV photopeaks (Ma 68) in a routed Ge(Li) counter coincidence spectrum), or to examine γ-cascades in the decay scheme of ^{26}Si as discussed in section 6.2.3. When used for Ge(Li) gain calibration the NaI crystal was placed near the Ge(Li) detector, but away from the target.

6.2. 2 Distant Geometry Lifetime Measurements

For the measurements of the lifetimes of the 1.80, 2.78, 3.33 and 4.14 MeV states (sections 6.3.1 and 6.3.2), the neutron detector was fixed at 0° to the beam with its front face 16 cm from the target, whilst the Ge(Li) detector front face was 10 cm from the target. The observed Doppler shift attenuations and the unshifted gamma ray energies were calculated from photopeak centroids in Ge(Li) spectra accumulated at 36°, 90° and 140°.

Figure 6.2A shows the neutron-coincident gamma rays

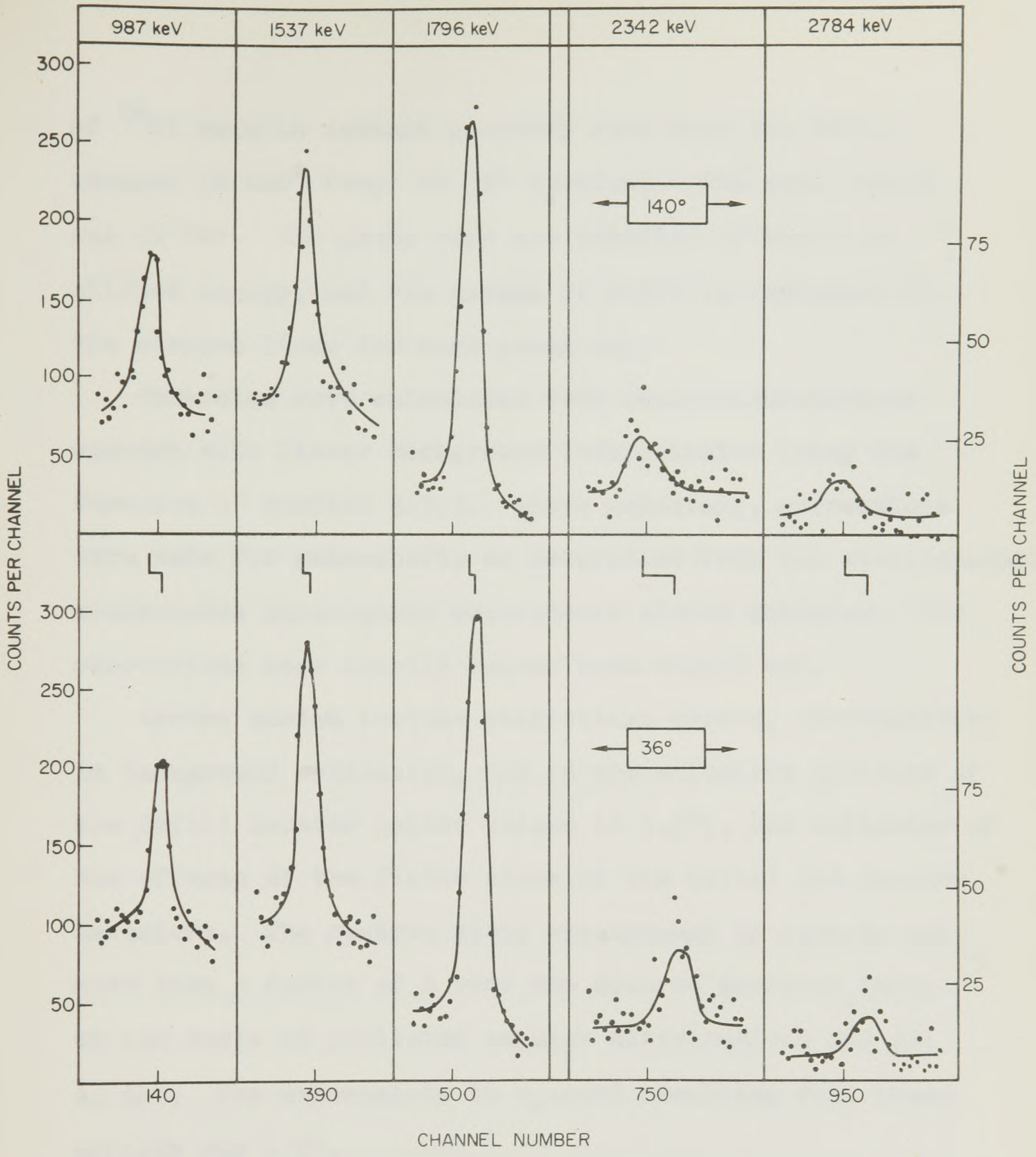

987 keV
1537 keV
1796 keV
2342 keV
2784 keV
140°
36°
COUNTS PER CHANNEL
COUNTS PER CHANNEL
CHANNEL NUMBER
140
390
500
750
950

FIGURE 6.2A

of ^{26}Si seen in distant geometry runs with the Ge(Li) counter at 140° (top) or 36° (bottom). The beam energy was 10 MeV. The gamma rays are labelled by their unshifted energy, and the amount of shift is indicated by the stepped lines for each gamma ray.

Centroids were calculated from reals-minus-randoms spectra with linear background interpolation using the formulae of section 3.3.5. Where necessary, corrections were made for gain-shifts as determined from the simultaneously accumulated gamma-gamma coincidence source spectrum. The corrections were usually rather less than 1 keV.

Errors quoted include statistical errors, uncertainties in background estimation, and in the effective position of the Ge(Li) counter active volume (± 1.5°), and estimates of the effects of the finite sizes of the Ge(Li) and neutron detectors. The neutron yield was assumed to vary by not more than a factor of 2 over the neutron detector face, on the basis of published angular distributions (Mc 67; Aj 60). The uncertainty in $v_o \cdot \cos\theta$ resulting from these effects was ± 2%.

For the various photopeaks a least-squares fit of the quantity $E + \Delta E. \cos\theta$ to the centroids of the measurements, including repeated 36° and 140° runs, gave χ^2/ν values

of order unity. This indicated properly consistent data, and, in particular, effective correction for gain shifts. E is then the unshifted gamma-ray energy, and ΔE is the effective observed $90^\circ \rightarrow 0^\circ$ energy shift from which $F(\tau)$ was calculated (tables 6.3A and 6.3B).

The ADC calibration and linearity were checked with sources (Ma 68) and found to be better than $\pm$ 0.1 keV over the range of interest.

The attenuation, $F(\tau)$, of the Doppler shift of a gamma ray due to the mean lifetime, τ, of the decaying state was calculated using the formula (cf. eq. 3.3k)

$$F(\tau) = \frac{1}{v_o \tau} \int_0^\infty v(t) . \overline{\cos\phi(t)} . e^{-t/\tau} . dt$$

where v_o and $v(t)$ are the initial and instantaneous speeds of the recoiling nucleus, and ϕ is the angle between the initial and instantaneous recoil directions. The method of numerical integration of this formula has been discussed in section 3.3; it suffices to recollect here that both electronic and nuclear stopping powers enter into the calculation of $v(t)$, and that $\overline{\cos\phi(t)}$ estimates the effect of large angle scattering of the recoiling ions.

The reaction yield was assumed to be uniform throughout the target. As the (^{3}He,n) reaction was expected to be mainly direct at these energies the yield was unlikely to vary sharply. If there were appreciable resonances, the target was thick enough to average over them efficiently.

Figure 6.2B shows a typical F(τ) curve, and the errors associated with uncertainties in the nuclear and electronic stopping power correction factors (cf. section 3.3.3) can be clearly appreciated.

In the case of long life-times, allowance has been made in the calculated F(τ) curves for nuclear recoils into vacuum from the back of the (finite-thickness) target. For the longest lifetime studied (the 3.33 MeV level) this correction was 10%.

These errors in the F(τ) curves have been included in the final lifetime errors.

6.2. 3 Close Geometry Lifetime and Decay Measurements

To study the decay schemes of other, less strongly excited, ^{26}Si states, n-γ coincidence spectra were accumulated to good statistics at 10 MeV and 7.8 MeV. The neutron counter was at 0°, and 8 cm from the target; the Ge(Li) counter was at 90°, and 2 cm from the target. Figure 6.2C

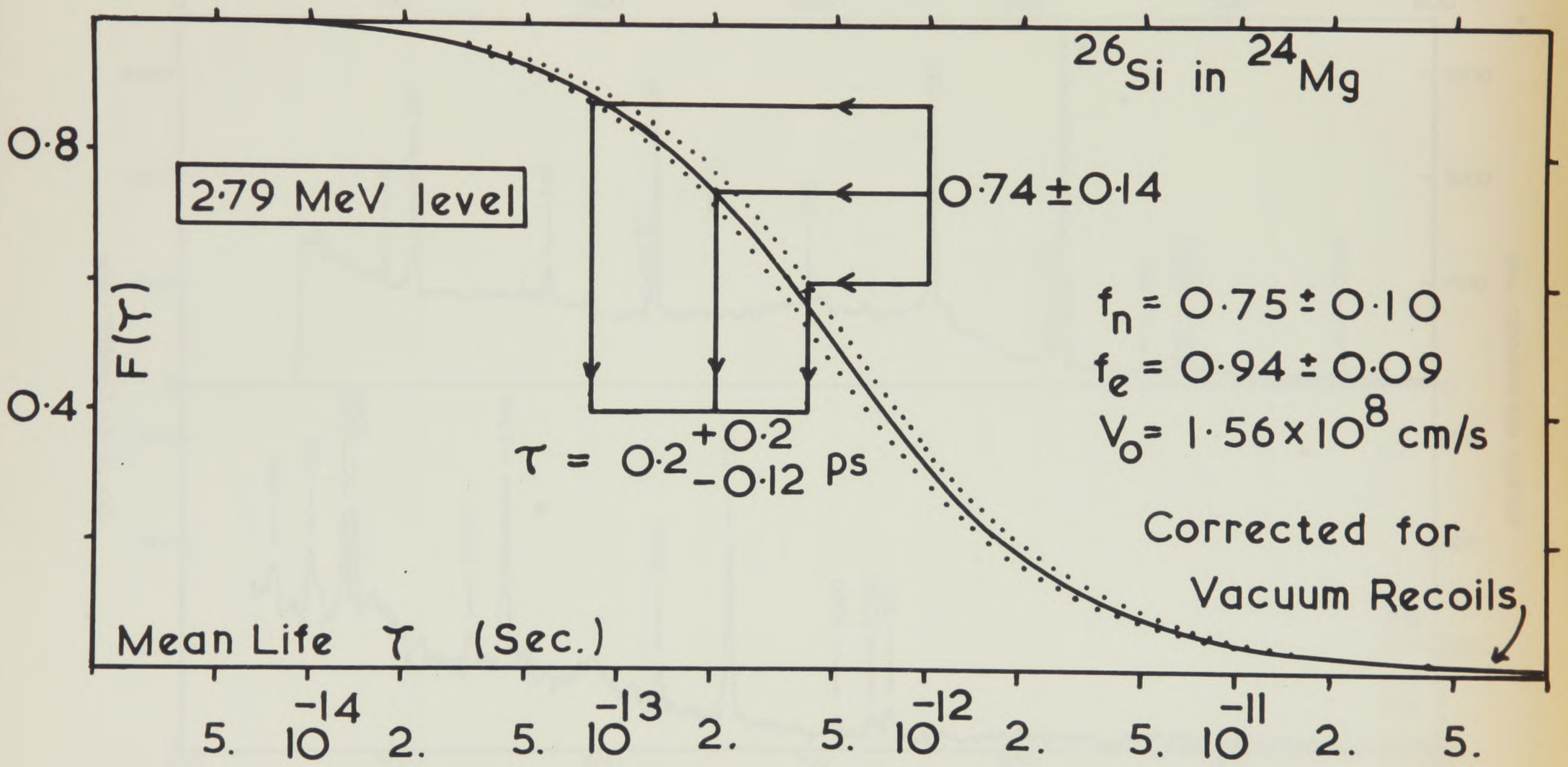

^{26}Si in ^{24}Mg
2·79 MeV level
0·74 ± 0·14
f_n = 0·75 ± 0·10
f_e = 0·94 ± 0·09
V_o = 1·56 × 10^8 cm/s
$\tau = 0.2^{+0.2}_{-0.12}$ ps
Corrected for Vacuum Recoils
F(τ)
0·8
0·4
Mean Life τ (Sec.)
5. 10^{-14} 2. 5. 10^{-13} 2. 5. 10^{-12} 2. 5. 10^{-11} 2. 5.

Figure 6·2B

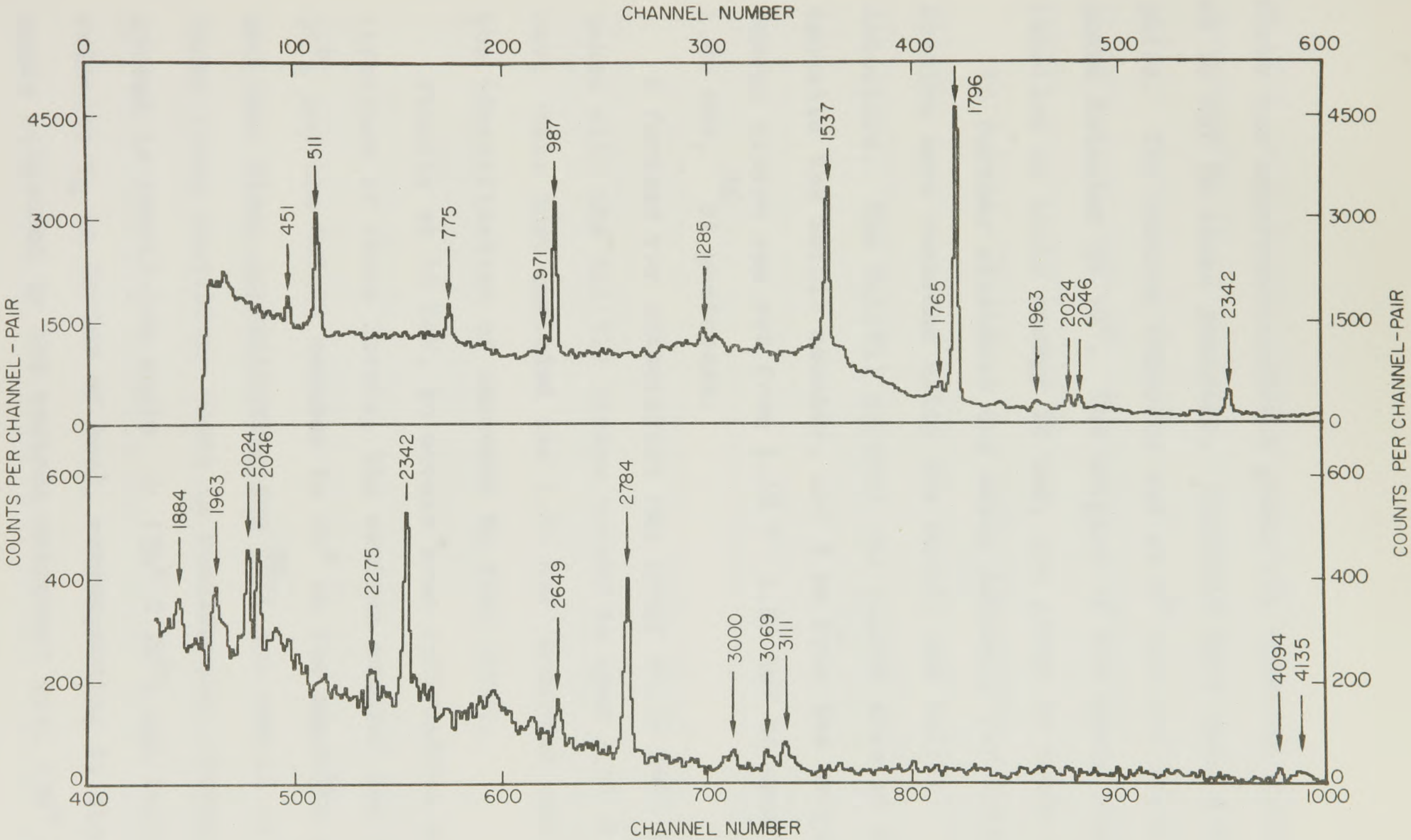

CHANNEL NUMBER
0
100
200
300
400
500
600
4500
3000
1500
0
COUNTS PER CHANNEL-PAIR
451
511
775
971
987
1285
1537
1765
1796
1963
2024
2046
2342
1884
1963
2024
2046
2275
2342
2649
2784
3000
3069
3111
4094
4135
400
500
600
700
800
900
1000
CHANNEL NUMBER

FIGURE 6.2C

shows the neutron-coincident gamma ray spectrum obtained at 10 MeV in close geometry. Channels have been added in pairs. The neutron detector was at 0° and the Ge(Li) gamma detector at 90°. The origins of the gamma rays, labelled by their energy in keV, are given in table 6.3D.

To further elucidate the decay schemes, γ-γ coincidence spectra were recorded using the Ge(Li) and NaI(Tl) detectors. The NaI(Tl) crystal was placed also at 90°, opposite the Ge(Li) counter, and 5 cm from the target; its energy window was set from 1.68 → 1.86 MeV to span the 1.80 MeV, ^{26}Si photopeak.

A further γ-γ coincidence run (only at 10 MeV) was taken with the NaI(Tl) window raised to span 1.92 → 2.07 MeV. This just excluded the 1.80 MeV photopeak and aided the identification of cascades to that level.

Finally at 10 MeV, to obtain some information on the lifetimes of these levels, the neutron counter was moved to 30°, and the Ge(Li) counter to 20° on the opposite side of the beam line, approximating the ^{26}Si ion recoil direction. Under these conditions there is considerable kinematic spread in recoil-ion angle ψ ($34^{\circ} \pm 20^{\circ}$) and initial velocity v_o (a factor of two), corresponding to the wide angle subtended by the neutron detector: viz. ($30^{\circ} \pm 30^{\circ}$)

as well as in Ge(Li) detector angle $\theta(20^{o} \pm 20^{o})$. However, the quantity of interest is the mean value of $\frac{v_o}{c}.\cos(\theta - \psi)$ and the reaction kinematics cause v_o to increase with ψ in such a way that the variations fortuitously largely cancel in the above product.

With this geometry, at 10 MeV beam energy, for levels between 2 and 4 MeV excitation in ^{26}Si, and for plausible neutron distributions (Mc 67; Aj 60), a mean value of $(5.5 \pm 0.5) \times 10^{-3}$ for $\frac{v_o}{c}.\cos(\theta - \psi)$ was obtained. Using this value the various $F(\tau)$ values were calculated from the observed shifts, and lifetime limits obtained (table 6.3B).

Vindication of this somewhat crude method was provided by the agreement with the nicer distant geometry results (section 6.2.2) for the 1.80, 2.78, 3.33 and 4.14 MeV levels.

6.3 Experimental Results for ^{26}Si

The experimental results discussed in this section have been summarised in tables 6.3A,B,C,D, and in fig. 6.1A.

6.3.1 The 1.80 MeV Level of ^{26}Si

This level was studied firstly in distant geometry at 5.5 MeV. Although states up to $\sim$4 MeV were kinematically

TABLE 6.3A

^{26}Si Level Energy Determinations (keV)

Level	J^{π}	Ajzenberg-Selove and Dunning	Miller and Kavanagh	McMurray et al	Hagen et al	Rolfs and Trost	Davies et al	Present work
1	2^+	1780 ± 60	1790 ± 30	-	1800 ± 30	1790±10	1806±50	1795.9±0.2
2	2^+	2790 ± 80	2800 ± 30	2780±40	2790 ± 30	2780±10	2777±50	2783.5±0.4
3	0^+			3350±40	3360 ± 30	3320±20	-	3332.5±0.3
4	3^+			(3770±40)	3780 ± 30	-	3745±50	3756±2
5	$4^{(+)}$			3890±40	-	(3820±40)	-	3842±2
6	1,2					-	-	4093±3
				4160±30	4160 ± 30			
7	$1,2^+$					4130±30	-	4138±1
8	(2^+)				4460 ± 30		4425±50	4445±3
9					(4650 ± 30)			-
10	$0^+,1,2,3,4^+$				4830 ± 30			4805±2
11					(5140 ± 30)			
REF:		Aj60	Mi67	Mc67	Ha68	Ro68	Da67 Sk67	

TABLE 6.3B

Lifetime Measurements in ^{26}Si

Level	Transition (MeV)	E_γ (MeV)	Branch %	F(τ)			τ (ps)	Γ_{total} (μeV)	Notes
				a)	b)	c)			
1	1.80 → 0	1.80	100	0.23±0.15	0.3±0.1	0.16±0.03	$1.38^{+0.7}_{-0.5}$	480^{+270}_{-160}	d
2	2.78 → 0	2.78	30±5		0.7±0.15	0.54±0.20	$0.20^{+0.20}_{-0.12}$	3300^{+5000}_{-1600}	e
	→ 1.80	0.99	70±5		0.9±0.15	0.85±0.16			
3	3.33 → 1.80	1.54	100		0.2±0.15	0.15±0.05	$2.7^{+2.3}_{-1.0}$	250^{+140}_{-120}	e
4	3.76 → 1.80	1.96	70±10		0.8±0.3				f
	→ 2.78	0.97	30±10		0.75±0.5		<0.7	>1000	
7	4.14 → 1.80	2.34	80±10		1.1±0.2	0.87±0.12	$0.11^{+0.11}_{-0.10}$	$6000^{+\infty}_{-3000}$	e
8	4.45 → 1.80	2.65	100		0.8±0.3		<0.5	>1300	f
10	4.81 → 1.80	3.01	30±10		1.0±0.2		<0.1	>6600	f
	→ 2.78	2.02	70±10		>0.95	1.4±0.6			

a) 5.5 MeV, distant geometry, cf. section 6.2.2

b) 10 MeV, close geometry, cf. section 6.2.1
Assumed $\overline{v/c} = 0.0055 \pm 0.0005$.

c) 10 MeV, distant geometry, cf. section 6.2.2

d) τ and Γ based on col. c) result for F(τ), and corrected for cascades to this state, cf. section 3.3.4

e) τ and Γ based on col. c) only.

f) Limits quoted at one standard deviation.

TABLE 6.3C

Gamma Transition widths in ^{26}Si

Level	Transition (MeV)	E_γ (MeV)	Branch %	Γ_γ (μeV)	J_i^π	J_f^π	δ	$\lvert M\rvert^2_{M1}$	$\lvert M\rvert^2_{E2}$	Notes
1	1.80→0	1.80	100	480^{+270}_{-160}	2^+	0^+	0		7^{+11}_{-4}	
2	2.78→0	2.78	30±5	1000^{+1500}_{-500}	2^+	0^+	0		$1.6^{+2.4}_{-0.8}$	a
	→1.80	0.99	70±5	2300^{+3500}_{-1100}		2^+	0.21 ±0.10	$0.11^{+0.17}_{-0.05}$	29^{+51}_{-24}	a
3	3.33→0	3.33	<2	<8	0^+	0^+				a
	→1.80	1.54	100	250^{+140}_{-120}		2^+	0		$7.8^{+4.5}_{-4.0}$	a
	→2.78	0.55	<2	<8		2^+	0		<40	a
4	3.76→0	3.76	<15		3^+?	0^+				c
	→1.80	1.96	70±10	>700		2^+	0		$>4\times10^{-3}$	b
	→2.78	0.97	30±10	>300		2^+	0		$>15\times10^{-3}$	b
5	3.84→0	3.84	<20		4^+?	0^+				c
	→1.80	2.05	100			2^+				
	→2.78	1.06	<15			2^+				
6	4.09→0	4.09	100			0^+				
	→1.80	2.30	<20			2^+				
	→2.78	1.31	<40			2^+				
	→3.33	0.76	<30			0^+				
7	4.14→0	4.14	20±10	>600		0^+				
	→1.80	2.34	80±10	>2400		0^+				
	→2.78	1.35	<10			2^+				
	→3.33	0.81	<10			0^+				
8	4.45→0	4.45	<10			0^+				
	→1.80	2.65	100	>1300		2^+				
	→2.78	1.66	<20			2^+				
	→3.33	1.11	<15			0^+				
10	4.81→0	4.81	<10			0^+				
	→1.80	3.01	30±10	>2000		2^+				
	→2.78	2.02	70±10	>4600		2^+				
	→3.33	1.47	<20			0^+				

a) Branching and mixing ratios from (Ro68)

b) $\delta=0$ assumed

c) J^π from section 7.4.4

TABLE 6.3D

Summary of Gamma Rays observed

Observed Gamma Energy (keV)	n-γ 10 MeV 0°/90°	n-γ 10 MeV 30°/20°	γ-γ a) 10 MeV 90°/90°	γ-γ b) 10 MeV 90°/90°	n-γ 7.8 MeV 0°/90°	γ-γ a) 7.8 MeV 90°/90°	Origin	Expected Energy (keV)
451±2	x	x	x	x	•	x	0.45→0 (^{25}Al)	455±2 c)
511.0±0.1 e)	x	x	x	x	x	x	e^+e^-	511.0
775±2	x	x	•	W	x	•	1.80"	744
971±3	x	x	?	W	x	?	3.76→2.78	972
987.0±0.5	x	x	x	W	x	x	2.78→1.80	987.6
1285±3	W	W	W	•	W	•	1.80'	1285
1536.6±0.2	x	x	x	•	x	x	3.33→1.80	1536.6
1765±3	x	x	•	•	W	•	2.78"	1762
1795.9±0.2	x	x	x	W	x	W	1.80→0	1795.9
1884±3	x	x	W	•	W	x	1.89→0 (^{18}Ne)	1887 d)
1963±4	x	x	x	?	x	•	3.76→1.80	1960
2024±2	x	x	W	•	x	•	4.8→2.78	2021
2046±2	x	?	W	•	x	x	3.84→1.80	(2046)
2275±3	x	x	W	•	x	•	2.78'	2273
2342±1	x	x	x	•	x	x	4.14→1.80	2342
2649±3	x	x	x	•	•	•	4.45→1.80	(2649)
2784.4±1.0	x	x	•	W	x	•	2.78→0	2783.5
3000±8	x	x	x	W	?	W	4.81→1.80	3009
3069±4	x	•	•	•	•	•	4.09"	3071
3111±8	x	x	•	•	x	•	4.14"	3116
4094±4	x	•	•	•	•	•	4.09→0	4093
4135±6	x	x	•	•	x	•	4.14→0	4138

x Clearly present

? Doubtful

W Present, but weak

• Absent

a) NaI(Tl) window: 1.68→1.86 MeV

b) NaI(tl) window: 1.92→2.07 MeV

c) ref.(En68).

d) ref.(Ro69).

e) This measurement served as a check on the ^{88}Y calibration of the ADC (Ma68).

detectable in n-γ coincidence, the gamma ray spectrum showed that cascades from higher states totalled less than 15% of the state population. Yield was poor however and only rather inaccurate results were obtained for the energy and lifetime (~1.5 ps).

Much higher yield was obtained in distant geometry at 10 MeV, though here the state was primarily populated by cascades from higher levels: particularly those at 2.80, 3.33 and 4.14 MeV (roughly 20%, 40% and 10% respectively). Within other errors, the initial velocities (and therefore the $F(\tau)$ curves)were the same for all levels. In section 3.3.4 it was shown that in this situation, where several levels each with lifetime τ_i and direct population ν_i ($i \geq 2$) decay to a level with τ_1 and ν_1, then the observed Doppler shift for the latter level depends on

$$\overline{F(\tau_1)} = \nu_1 F(\tau_1) + \sum \frac{\nu_i}{\tau_i - \tau_1} (\tau_i F(\tau_i) - \tau_1 F(\tau_1))$$

where $\nu_1 + \sum \nu_i = 1$.

The most important effect on the observed $\overline{F(\tau_1)}$ for the 1.80 MeV level is from the strongly populated, longer lifetime (section 6.3.2), J = 0, 3.33 MeV state (Ro 68).

Its population was accurately determined from the intensity of the (isotropic) 1.54 MeV gamma ray using Ge(Li) photopeak efficiencies (La 67; An 68).

The relative intensities of the other levels, which had short lifetimes (table 6.3B), were less critical and were determined sufficiently well from the 90°, close geometry, 10 MeV, n-γ run. Angular correlations were unlikely to introduce more than 20% error into these populations.

The state energy was found to be 1795.9 ± 0.2 keV, and the lifetime $1.38^{+0.7}_{-0.5}$ps. The latter error includes the effects of errors in τ_i and ν_i.

It should be noted that the effect of recoil after gamma ray emission is negligible. For a 1 MeV gamma ray emitted from ^{26}Si, the nuclear recoil velocity is $\sim 1.2 \times 10^6$ cm/s whilst the initial nuclear velocity is $\sim 1.6 \times 10^8$ cm/s, so that the effect is of order 0.8% (and is in fact even smaller since gamma rays are emitted into 4π steradians with forward-backward symmetry).

6.3. 2 The 2.78, 3.33 and 4.14 MeV levels of ^{26}Si

These states were all studied in distant geometry (section 6.2.2) at 10 MeV. The energies for the 2.78 MeV state deduced from its decay branches to the ground and 1.80

MeV states were in good agreement, and the F(τ) values reasonably so. The adopted energy is 2783.5 ± 0.4 keV, and the lifetime $0.20^{+0.20}_{-0.12}$ ps. The error covers the possible effect of decays to this level from the 3.76 and 4.81 MeV states (~25% such indirect population determined from fig. 6.2C), and the proximity of the 0.97 MeV gamma ray resulting from the 3.76 → 2.78 MeV decay.

The lifetime and energy of the 3.33 MeV level were determined from its 1.54 MeV decay to the first excited state. To facilitate determination of the background under the 1.54 MeV photopeak, it was in each case necessary to remove the Compton edge of the 1.80 MeV gamma ray. This edge occurred at only slightly higher energy. The removal was accomplished by fitting a 1.84 MeV (^{88}Y source) lineshape to the 1.80 MeV photopeak, and then subtracting it from the n-γ coincidence spectrum.

The adopted value of 1536.6 ± 0.2 keV for the gamma ray energy puts the state at 3332.6 ± 0.3 keV excitation. The lifetime was found to be $2.7^{+2.3}_{-1.0}$ ps.

The energy and lifetime of the 4.14 MeV state were determined from its 2342 ± 1 keV branch to the 1.80 MeV state. The level energy is then 4138 ± 1 keV, in agreement with the ground state transition energy 4135 ± 6 keV

obtained from the close geometry, 90^{o}, n-γ spectra. The lifetime is $0.11^{+0.11}_{-0.10}$ ps.

6.3. 3 Decay Schemes, Higher States

As can be seen from table 6.3A, there was some disagreement in the literature as to the positions of higher states of ^{26}Si, and the various spectra summarised in table 6.3D were taken to resolve this situation.

The ^{24}Mg(^{3}He,pn)^{25}Al reaction was also (En 68) energetically possible (Q = 5.23 MeV), and at the beam energies of 7.8 and 10 MeV one might kinematically expect to see n-γ coincidences corresponding to decay of ^{25}Al levels up to $\sim$ 1 and $\sim$3 MeV respectively. The energy levels of this nucleus are well known (En 68) and in fact only the decay of the 0.455 MeV, first excited state of ^{25}Al was observed (cf. fig. 6.2C and table 6.3D). The 1.887 MeV, first excited to ground state, transition of ^{18}Ne was seen (only) at 10 MeV beam energy. This results from oxygen contamination of the target, via the reaction ^{16}O(^{3}He,n)^{18}Ne. All other significant gamma rays have been identified as coming from known or anticipated ^{26}Si levels, and appeared or disappeared in the various n-γ and γ-γ coincidence spectra as appropriate to their origin (table 6.3D).

At 7.8 MeV the yields were lower than at 10 MeV, and some levels were not seen. At this energy the target was ~ 1 MeV thick and one expected in particular to see the 2.03 MeV decay of the 3.82 MeV state reported by Rolfs and Trost (Ro 68) who used a thin target and 7.3 MeV beam (section 6.3. 4).

Although no proper account could be taken of possible Y-ray angular correlations, very rough branching ratios could be determined in a number of cases (fig. 6.1A and table 6.3C). For the 2.78 and 4.14 MeV levels these ratios were in agreement with the more accurate determinations of Rolfs and Trost.

6.3. 4 The 3.76 and 3.84 Levels of ^{26}Si

These two levels have been the subject of particular disagreement in the literature (table 6.3A). (Mc 67) saw levels at 3770 ± 40 and 3890 ± 40 keV in a neutron time-of-flight experiment at 5.6 MeV ^{3}He beam energy, but (Ha 68) saw only a 3780 ± 30 keV state at 6.15 MeV. (Da 67; Sk 67) saw a state at 3745 ± 50 keV in the ^{28}Si(p,t)^{26}Si reaction. (Ro 68) saw a gamma ray of 2030 ± 40 keV implying a level at 3820 ± 40 keV, but their spectrum does not enable one to entirely exclude the possibility of more than one gamma ray

in this region.

Actually our n-γ spectra at 7.8 and 10 MeV showed three gamma rays: viz. 1.96, 2.02 and 2.05 MeV. Because of this fact the 2.03 MeV gamma ray correlation of Rolfs and Trost (Ro 68), from which a spin $J = 3$ was assigned to their 3.82 MeV state, must be regarded with extreme caution.

The 1.96 MeV gamma ray we assign to a 3.76 MeV level decay to the 1.80 MeV level. This is supported by the observation of an ~25% branch of 0.97 MeV to the 2.78 MeV state. The energies are in good agreement (cf. tables 6.3A, D).

The 2.02 MeV gamma ray is discussed in section 6.3.5.

The 2.05 MeV gamma ray appeared from the γ-γ spectra to be associated with a 3.84 → 1.80 MeV level decay. This would be in agreement with the level energies observed by (Ro 68), and by (Mc 67). No other gamma ray branches were observed from this 3.84 MeV level.

These two, apparently somewhat coy, states at 3756 ± 2 keV and 3842 ± 2 keV are then in substantial agreement with previous observation. From the close geometry runs it appears that the lifetime of the 3.76 MeV state is less than 0.7 ps; no limits could be placed on the 3.84 MeV state lifetime.

6.3. 5 The 4.09, 4.45 and 4.81 MeV Levels of ^{26}Si

The 4.09 MeV level was apparent only from its ground state branch, and for this reason cannot be considered as absolutely established. It has not been previously reported, although, by analogy with ^{26}Mg, a further state near 4 MeV would be expected. Its closeness to the 4.14 MeV level is adequate explanation for its previous non-observation, though Hagen et al (Ha 68) did note changes in the shape of the neutron group from the 4.14 MeV state suggesting the presence of an unresolved level. The absence of the 4.09 MeV gamma ray from the $30^{o}/20^{o}$ n-γ close geometry spectrum (table 6.3D) precluded determination of its lifetime.

The 2.65 MeV gamma ray is believed to be the decay of the 4.45 MeV level to the 1.80 MeV state. This level has been previously observed (Ha 68; Da 67; Sk 67). No other decay modes were seen. The lifetime is less than 0.5 ps and the exact energy 4445 ± 3 keV.

The 2.02 and 3.00 MeV gamma rays indicate a state at 4.81 MeV decaying to the 1.80 and 2.78 MeV levels respectively. The energies are in quite good agreement with this hypothesis. A state at 4.83 ± 0.03 MeV has been reported by (Ha 68). The lifetime is less than 0.1 ps and the exact energy 4805 ± 2 keV.

"It is a capital mistake to theorize before one has data".

Sir Arthur Conan Doyle.

C H A P T E R 7

DISCUSSION OF RESULTS

7.1 The 4.44 and 5.02 MeV Levels of ^{11}B

The various experimental determinations of the mixing ratios, widths, and branching ratios of these ^{11}B levels are reviewed in table 7.1A. The mixing ratios have been converted to the sign convention of (Ro 67) by reanalysis of the published gamma ray angular distributions or Legendre coefficients.

(i) The width and mixing ratio of the 4.44 MeV level decay have been well established using a variety of techniques: e.g., resonance fluorescence (Ra 58), gamma ray angular distributions (Jo 59, Gr 62), inelastic proton scattering at 150 MeV (Cl 61), and high energy inelastic electron scattering (Sp 67). The absence of a 4.44 → 2.12 MeV branch has been noted previously (Ol 65; Do 61). The present solution for the 4.44 MeV → g.s. mixing ratio, $\delta(E2/M1) = -0.19 \pm 0.03$, assuming an initial spin of $J = 5/2$, is in good agreement with the magnitude and sign of previous determinations. The mixing ratio for the

Table 7.1A

Review of Various Workers' Experimental Results[a] for ^{11}B

Ref:	Ra 58	Ja 59	Do 61	Cl 61	Gr 62	Ol 65	Sp 67	Ea 68	Present work	Weighted Means
Reaction :	(γ,γ)	(α,γ)	$(^3He,p)$	(p,p')	(α,γ)	$(^3He,p)$ (d,p)	(e,e')	$(^3He,p)$	(t,p)	
4.44 → 0 $(5/2^- \rightarrow 3/2^-)$ $\delta(E2/M1)$	$\Gamma = 0.56 \pm 0.08$ $\delta = -0.22 \pm 0.22$	$\delta = -0.2$		$\Gamma(E2) = 0.01$	$\delta = -0.20 \pm 0.02$	$\Gamma > 0.001$	$\Gamma(M1) = 0.60 \pm 0.09$ $\Gamma(E2) = 0.016 \pm 0.002$ $\lvert\delta\rvert = 0.16 \pm 0.03$		$\delta = -0.19 \pm 0.03$	$\Gamma = 0.58 \pm 0.06$ $\delta = -0.19 \pm 0.015$ 100%
4.44 → 2.12			$< 0.5\%$			$< 1\%$			$< 3\%$	$< 0.5\%$
5.02 → 0 $(3/2^- \rightarrow 3/2^-)$ $\delta(E2/M1)$			$(86 \pm 3)\%$			$\Gamma > 0.001$ $(84 \pm 2)\%$	$\Gamma(M1) = 1.73 \pm 0.14$ $\lvert\delta\rvert < 0.045$	$(88 \pm 2)\%$	$\delta = 0.03 \pm 0.05$ $(88 \pm 2.5)\%$	$\Gamma = 1.73 \pm 0.14$ $\delta = 0.03 \pm 0.05$ $(87 \pm 1.5)\%$
5.02 → 2.12 $(3/2^- \rightarrow 1/2^-)$ $\delta(E2/M1)$			$(14 \pm 3)\%$			$(16 \pm 2)\%$		$(12 \pm 2)\%$	$\delta = -0.05 \pm 0.2$ $(12 \pm 2.5)\%$	$\Gamma = 0.28 \pm 0.05$ $\delta = -0.05 \pm 0.2$ $(13 \pm 1.5)\%$
5.02 → 4.44			$< 0.3\%$							$< 0.3\%$

a) Mixing Ratios (δ), Widths (Γ, in eV), and Branching Ratios.

corresponding transition in ^{11}C is $\delta = 0.17 \pm 0.02$ (Ga 66; Blk 67; Ea 68).

Poletti et al. (Po 67) have compared these determinations with LS and intermediate coupling calculations. In the LS case both mixing ratios have the wrong sign and are too small in magnitude by a factor of two; but the intermediate coupling calculations, based on the p-shell effective interaction results of (Co 65), reproduce the measured values and signs quite closely when an additional effective charge of + 0.5e is ascribed to each nucleon. The opposite phases of the mixing ratios in ^{11}B and ^{11}C are to be expected in view of the reasonably strong natures of both the M1 and E2 parts of the transitions (Po 67).

(ii) The spin of the 5.02 MeV, ^{11}B level was expected (Do 61; Co 67; Ea 68) to be $3/2$, and this is confirmed unambiguously by the present results. Spamer and Artus (Sp 67) have used high energy electron scattering experiments to measure $\Gamma(5.02 \rightarrow \text{g.s; M1}) = 1.73 \pm 0.14$ eV, and $\Gamma(E2)/\Gamma(M1) < 0.002$, so that $|\delta| < 0.045$, in agreement with our smaller solution ($\delta = 0.03 \pm 0.05$) for the 5.02 MeV $\rightarrow$ g.s. transition mixing ratio. From their width measurement and the present branching and mixing ratios for the 5.02 $\rightarrow$ 2.12 MeV transition, the absolute M1 and E2 transition

widths can be calculated. The larger solution for δ(5.02 → 2.12) would given an E2 width > 0.12 eV which is 500 Weisskopf units and was discarded since it violates various sum rules (Wi 60), but the smaller solution is acceptable.

The branching ratio measurement is in good agreement with previous determinations (Aj 68; Ol 65; Do 61; Ea 68).

Identifying the 5.02 MeV level with Kurath's second $J = 3/2$ state ($3/2^*$) predicted in intermediate coupling (Ku 56), the experimental widths are compared in table 7.1B with the predictions of this model (Ku 57). Best agreement is obtained for $3 \leqslant a/K \leqslant 6$. The predictions of a more recent p-shell effective interaction fit (Co 65) are included for comparison and also give good agreement.

Donovan et al. (Do 61) have previously discussed the 5.02 MeV state in some detail, concluding that $J^\pi = 3/2^-$ was most likely for the level. On this assumption they noted that a value $a/K \approx 4$ would give best agreement with intermediate coupling calculations, both for the 5.02 MeV branching ratio, and for the ^{11}B ground state magnetic moment (cf. In 53; Co 65).

An alternative collective model description has been proposed by Clegg et al. (Cl 61a). The ground, 4.44 MeV, and 6.74 MeV levels ($J^\pi = 3/2^-$, $5/2^-$, $7/2^-$ respectively)

Table 7.1B

^{11}B, 5.02 MeV level : electromagnetic transition widths in eV.

Transition, Multipolarity	Experimental values a)	8 - 16 2BME (Co 65)	Intermediate Coupling (Ku 56, Ku57)					
			a/K = 0	1.5	3	4.5	6	7.5
5.02 →g. s., M1	1.73 ± 0.14	2.0	0.12	0.51	1.6	1.9	2.0	1.9
5.02→g. s., E2	< 0.01	-	0.025	0.016	0.005	0.002	0.002	0.002
5.02→2.12, M1	0.28 ± 0.05	0.26	0	0.077	0.19	0.20	0.19	0.18
5.02→2.12, E1	< 0.015	-	0.0014	0.0015	0.0013	0.0012	0.0011	0.0010

a) this work combined with (Sp 67)

would belong to a $K = 3/2$ band, whilst the 2.12 and 5.02 MeV levels ($J^{\pi} = 1/2^-$, $3/2^-$ respectively) would belong to a $K = \frac{1}{2}$ band. This model's particular merits are (i) an explanation of the strong 6.74 → 4.44 MeV and 4.44 MeV → g.s. E2 decays; (ii) the energy of the $7/2^-$, 6.72 MeV level (which is predicted too low in intermediate coupling); and (iii) the absence of a 4.44 → 2.12 MeV branch (which would be forbidden since it would be between different bands).

7.2 The ^{14}C Results

7.2.1 Introduction

Historically the mass 14 nuclei have been of considerable theoretical interest because of the comparative ease of calculations near the ^{16}O doubly-closed shell, and because of the wealth of experimental data available.

Intermediate-coupling calculations within the $1s^4 1p^{10}$ configuration were able to reproduce quite well the positions of a number of low-lying positive-parity states (In 53; Ku 56; Ku 57; Un 58; Ta 60; Co 65), but notably failed to account for the gamma decay properties of the first two excited states of ^{14}N and for the anomalously long β-decay lifetime of ^{14}C (In 53; Vi 57; Ho 68a). These latter

difficulties are now considered to be explained within the $1s^4 1p^{10}$ configuration by the presence of nuclear tensor forces (Ja 54; El 56; Vi 57; Za 66; Ro 68a), but an explanation (which failed (Ro 68a)) was also sought (In 53; Ba 58) in terms of mixing of the configurations $1s^4 1p^{10}$ and $1s^4 1p^8 (sd)^2$. [By $(sd)^2$ is meant the presence of two particles in the $2s_{1/2}$, $1d_{5/2}$ and $1d_{3/2}$ orbitals.] The possibility of excitation of two particles into the sd-shell was enhanced by the observation of low-lying negative-parity states (fig. 4.1B) which are due to excitation of one particle into the sd-shell and have the configurations $1s^4 1p^9 (sd)^1$, and by the binding energy calculations of Unna and Talmi (Un 58; Ta 60).

One might anticipate the presence of even more complex configurations due to excitation of particles from the 1s core, or into the 2p1f shell, or even $1s^4 1p^6 (sd)^4$ excitations. These should be less significant however because of the greater energy changes involved; it is for this reason, and because of the considerable computational difficulties, that these more complex configurations are not included in presently published theoretical treatments. There is some experimental evidence to support this omission (Ha 57; Ho 58; Ba 58; Ro 64, and further references in Ro 68a).

On the basis of the calculations of (In 53; El 56; Vi 57)

Warburton and Pinkston (Wa 60) calculated electromagnetic transition widths, reduced stripping widths, and inelastic scattering cross-sections for T = 0 and T = 1 states arising from the configurations s^4p^{10}, $s^4p^9(sd)^1$, and $s^4p^8(sd)^2$. By comparison with existing experimental data, shell model jj-coupling assignments were made for the predominant configurations of each known ^{14}C level below 9 MeV excitation, and for many ^{14}N levels. Configuration admixture was also examined and of particular interest here is their conclusion that the 9.17 and 10.43 MeV, $J^\pi = 2^+$, T = 1 levels of ^{14}N result from strong admixture of the s^4p^{10} and $s^4p^8(sd)^2$ configurations. These ^{14}N, T = 1 states correspond to the 7.01 and 8.32 MeV levels of ^{14}C.

The works of Unna and Talmi (Un 58; Ta 60) and of Warburton and Pinkston (Wa 60) identified those states containing appreciable admixture of "core-excited" configurations arising from excitation of particles out of the $1p^{3/2}$ orbitals. Sebe (Se 63) considered core-excitation in the negative parity states of ^{14}C. He calculated mixed-configuration wavefunctions for a model in which a single neutron in the sd-shell was coupled to $J^\pi = 1/2^-$ and $3/2^-$, $T = 1/2$ states of ^{13}C obtained from an s^4p^{10} intermediate-coupling calculation. In particular the $J^\pi = 1^-$ and 2^- states (6.09

and 7.35 MeV in ^{14}C) were found to contain appreciable core-excited configuration admixtures.

Also of interest is the work of True (Tr 63) who performed a shell-model calculation of those levels of ^{14}N which are not core-excited, i.e., which could be described as two nucleons moving in the $1p_{1/2}$, $2s_{1/2}$, $1d_{5/2}$ and $1d_{3/2}$ orbitals. Quite good agreement with experimental energies, spins and parities was obtained but, as noted earlier, True's wavefunctions do not explain the ^{14}C β-decay, nor the decays of the first two excited states of ^{14}N (Ro 68a).

Alburger et al. (Al 66) studied ^{14}C gamma transitions using the ^{13}C(d,pγ)^{14}C reaction, and obtained decay schemes and lifetime limits for the 6.09(1^-), 6.58(0^+), 6.72(3^-), 6.89(0^-), and 7.35(2^-) MeV levels. Comparing these to theoretical calculations it was found that True's mixed-configuration wavefunctions (Tr 63) gave a better description of most transitions than did extreme jj-coupled eigenfunctions. In some cases an increase in the $1p_{1/2}1d_{3/2}$ eigenfunction admixture further improved the fit.

The 7.35 MeV → g.s. (M2) and the 6.59 → 6.09 MeV (E1) rates were not well described however and it was conjectured that excitation of the $p^8_{3/2}$ core was responsible for the discrepancy.

In the present work we have studied decays of the 6.72(3^-), 7.01(2^+), and 7.35(2^-) MeV levels of ^{14}C, and will compare these to various model predictions with particular reference to those of True (Tr 63). Past and present experimental information on these states and their decays is summarised in tables 7.2A and 7.2B.

7.2. 2 The 6.72 MeV Level of ^{14}C

Early stripping studies of the 6.72 MeV level gave inconclusive and contradictory spin-parity assignments (Mc 55; Mi 64; Ja 60). A recent study by Glover and Jones (Gl 66) using the $^{12}C(t,p)^{14}C$ reaction, analysing their results with the zero-range DWBA double-stripping theory of Rook and Mitra (Ro 64a), indicated $J^\pi = 3^-$; they later found confirmatory evidence from the $^{13}C(d,p)^{14}C$ reaction (Gl 66a). Warburton and Rose (Wa 66) combined their lifetime limit for the 6.72 MeV level with the stripping data of McGruer et al. (Mc 55), and the pair ratio measurements of Bent et al. (Be 55), to deduce $J^\pi = 2^-$ or 3^-, with 3^- strongly preferred. This is supported by more recent measurements (Al 66); $J^\pi = 2^-, 3^-$ was given by the multipolarity measurements of Warburton et al. (Wa 64). The various determinations are summarised in table 7.2A.

Table 7.2A

Summary of J^{π} determinations in ^{14}C

Level	Mc 55	Mi 64	Ja 60	G166	G166a	Wa66 +B155	A163	Wa64	La65	A1 66	a)	
6.72	$1^-, 2^-, 3^-$	(2^+)	3^-	3^-	(3^-)	$3^-, (2^-)$		$2^-, 3^-$	$2^-, 3^-$	$3^-, (2^-)$	3	3^-
7.01		(2^+)	$0^+, (2^+)$	2^+	(2^+)		(2^+) $J \geqslant 1$				2	2^+
7.35	$1^-, 2^-, 3^-$				(2^-)	1^+ or $J > 1$			$1, 2^-$	2^-	2	2^-

a) Present Result

b) Adopted

Table 7.2B

Comparison of determinations of ^{14}C branching ratios (%)

Level Transition	(Al 66)	(Al 66 + La65)	(Ca 66)	Present work
6.72 → g. s.	93 ± 2		91 ± 5	97.3 ± 1
→6.09	7 ± 2		9 ± 3	2.7 ± 1
7.01 → g. s.			100^{+0}_{-5}	98.6 ± 0.7
→6.09			< 5	1.4 ± 0.7
7.35 → g. s.	18 ± 4	13 ± 5	13 ± 3	14 ± 4
→6.09	47 ± 4	29 ± 13	60 ± 5	52 ± 5
→6.72	35 ± 7	58 ± 7	27 ± 5	34 ± 4

Table 7.2B

The 6.72 MeV → g.s. correlation (fig. 4.2H) uniquely determined $J = 3$, with no appeal to transition rates or specific models. The $(2.7 \pm 1)\%$ decay branch observed to the 6.09 MeV level is somewhat smaller than that reported by Carlson (Ca 66) or by Alburger et al. (Al 66) (cf. table 7.2B). No simple reason for the discrepancies between the different sets of measurements could be found. The present results were very carefully examined and rechecked.

The lifetime of the ^{14}C, 3^-, 6.72 MeV level is 97 ± 15 ps (Al 68). In table 7.2C are shown theoretical and experimental transition widths to the 1^-, 6.09 MeV and the 0^+, ground states. Columns 1 and 2 are calculations for pure jj coupled eigenfunctions and for True's model respectively and were taken directly from (Al 66). However the experimental widths in that reference were based on a preliminary lifetime estimate of 140 ± 20 ps so they have been recalculated using the correct value (97 ± 15 ps). Column 3 corresponds to the mean $(8 \pm 2)\%$ branching to the 6.09 MeV level of refs. (Al 66; Ca 66), whilst column 4 is based on the present $(2.7 \pm 1)\%$ branching.

The theoretical values are based on an effective neutron charge of 0.5e. They are nearly the same for the 6.72 → 6.09 MeV ($3^- \rightarrow 1^-$) transition, and lie between the

TABLE 7.2C

Transition Widths of the ^{14}C, 3^- level in μeV

Transition	Theory		Experiment	
	jj	(Tr 63)	(Al66; Ca 66)	Present
6.72 → 6.09 (E2)	0.29	0.31	0.55 ± 0.1	0.18 ± 0.07
6.72 → 0 (E3)	2.74	3.32	6.3 ± 0.9	6.6 ± 1.1

alternative experimental values, so that agreement must be considered satisfactory. The ground state transition is predicted to be too weak by a factor of ~2. This is not easily explained on any of the models assumed here: Sebe found very little simple core-excitation in the 3^- level and both True and Sebe find the 0^+ g.s. to be nearly pure $p_{1/2}^2$, with some $d_{5/2}^2$. The transition strength is fairly insensitive to (sd) admixture however (Al 66). One might speculate on the presence of 3^- configurations of type

$$\left| p_{3/2}^{-1} \; p_{1/2}^{-4} \; (sd)^3 \right\rangle$$

which could have appreciable matrix elements connecting to the

ground state $| p_{1/2}^{-4}(sd)^2 \rangle$ components.

7.2. 3 The 7.01 MeV Level of ^{14}C

The remarks on stripping results for the 6.72 MeV level apply also to the 7.01 MeV level (table 7.2B). Early stripping indications (Ja 60) that $J^\pi = 0^+$ have since been disputed (Mi 64; Gl 66; Gl 66a) in favour of $J^\pi = 2^+$, but, possibly because of the complex structure of this state, differential cross-sections have generally been poorly fitted by stripping theory. Alburger and Warburton (Al 63) have noted indirect evidence that $J^\pi = 2^+$. Here a unique assignment $J = 2$ is obtained.

The 0.92 MeV, 7.01 → 6.09, $2^+ \rightarrow 1^-$ transition has not been previously reported, although as will be seen on certain theoretical grounds it should be comparable in intensity to the ground state transition.

Warburton and Pinkston (Wa 60) have identified the $J^\pi = 2^+$, T = 1, 9.17 MeV level of ^{14}N as the analogue of the 7.01 MeV level of ^{14}C. These levels, together with the (presumably) analogue levels at 8.32 MeV in ^{14}C and 10.43 MeV in ^{14}N, are the lowest 2^+, T = 1 levels of mass 14, and result from strong mixing of two distinct 2^+, T = 1 states which appear in this energy region. One arises from the p^{10}

configuration, the other from $p^{8}_{3/2}(2s,1d)$, where $p^{8}_{3/2}$ is coupled to J = 0 and (2s,1d) is primarily $(2s_{1/2},1d_{5/2})$. These mixed states may therefore be written as

$$|\,2^+,1\,\rangle = A\,|\,p^{7}_{3/2}p^{3}_{1/2}\,\rangle + B\,|\,p^{8}_{3/2}(2s,1d)\,\rangle \quad .$$

The magnitudes of A and B have been estimated from the $^{13}C(p,\gamma)^{14}N$ reaction (Wa 60; Ro 64; Ro 60), from the $^{13}C(d,p)^{14}C$ reaction (Gl 66a), and from inelastic electron scattering experiments (Cl 68a), with, in all cases, the result $|A| \sim |B| \sim 0.7$.

Replacing $|\,p^{8}_{3/2}(2s,1d)\,\rangle$ by the lowest energy $2^+,1$ configuration of ^{14}N given by (Tr 63), dropping minor terms, and omitting the $p^{8}_{3/2}$ core from the notation, one obtains

$$|\,2^+,1\,\rangle = 0.7\,|\,p^{10}\,\rangle \pm 0.7\,\{\,0.90\,|\,s_{1/2}d_{5/2}\,\rangle + 0.36\,|\,d^{2}_{5/2}\,\rangle + C\,|\,s_{1/2}d_{3/2}\,\rangle\,\}$$

where an arbitrary coefficient C of $|\,s_{1/2}d_{3/2}\,\rangle$ is retained since this term is primarily responsible for the $2^+ \rightarrow 1^-$, E1 transition rate. For small values of C the overall normalization will not be sensibly affected. By $|\,p^{10}\,\rangle$ is still understood $|\,p^{7}_{3/2}p^{3}_{1/2}\,\rangle$.

For the ^{14}C ground and 6.09 MeV states the wave functions

given by (Tr 63) for the analogue 2.31 and 8.06 MeV, T = 1, states of ^{14}N are used. These also have $|\, p^8_{3/2}; 0^+ \,\rangle$ cores

$$|\, 0^+, 1 \,\rangle = -0.95 |\, p^2_{1/2} \,\rangle + 0.12 |\, s^2_{1/2} \,\rangle + 0.26 |\, d^2_{5/2} \,\rangle + 0.11 |\, d^2_{3/2} \,\rangle ,$$

$$|\, 1^-, 1 \,\rangle = -0.99 |\, p_{1/2} s_{1/2} \,\rangle + 0.11 |\, p_{1/2} d_{3/2} \,\rangle .$$

Evaluating the electromagnetic operators of section 3.1 between these states, and ascribing an effective charge of -0.5 to the neutron for E1 transitions (Wi 60), and + 0.5 for E2 transitions, gives

$$\Gamma(E2;\ 2^+ \to 0^+) = (5.5 \pm 2.9) \times 10^{-3} \text{ eV},$$

where the positive (negative) sign is to be used accordingly as the (unknown) sign of A/B is positive (negative), and

$$\Gamma(E1;\ 2^+ \to 1^-) = 0.1\ C^2 \text{ eV}.$$

For True's $|\, 2^+, 1 \,\rangle$ wave function C = -0.22, which gives $(E1;\ 2^+ \to 1^-) = 5 \times 10^{-3}$ eV, and so a branch of about 50% to the 6.09 MeV level. One in fact observed only a $(1.4 \pm 0.7)\%$ branch, which requires $0.01 < |C| < 0.04$. The discrepancy almost certainly arises from the approximations inherent in mixing the excited core and the closed core plus (s,d) configurations, and in the assumptions implicit in the effective charge approximation for E2 transition strengths.

7.2. 4 The 7.35 MeV Level of ^{14}C

The assignment J = 2 is in agreement with the particle-gamma ray correlation results of (La 65) and with the most likely value of J = 2 deduced in (Al 66) from gamma ray branching ratios, lifetime limits, and multipolarity measurements (table 7.2A). The measured branches are in close agreement with the results of (Ca 66), and of (Al 66), but not with those of (La 65) (table 7.2B).

On True's model (Tr 63) the 6.09, 6.72 and 7.35 MeV states have primarily the configurations $|p_{1/2}s_{1/2};1^-\rangle$, $|p_{1/2}d_{5/2};3^-\rangle$, and $|p_{1/2}d_{5/2};2^-\rangle$ respectively. To explain the relative branchings of 7.35 → 6.09 MeV and 7.35 → 6.72 MeV requires (Al 66) an amplitude admixture of about 20% of the $|p_{1/2}d_{3/2};1^-\rangle$ configuration into the 6.09 MeV state. This permits an M1 transition otherwise forbidden between the primary configurations. In True's wavefunction for the 1^-, T=1 analogue of the ^{14}C, 6.09 MeV state, the amplitude admixture is in fact 10%, which is also about the minimum necessary to fit the observed E2/M1 mixing ratio ($\delta = -0.04 \pm 0.09$) for the 7.35 → 6.09 MeV decay.

Admixture of the $|p_{1/2}d_{3/2};2^-\rangle$ configuration into the 7.35 MeV state appears to be small (Tr 63; Se 63) and neither of the low energy decay branches or mixing ratios is

very sensitive to it. For True's wavefunctions the predicted 7.35 → 6.72 MeV ($2^- \rightarrow 3^-$) mixing ratios is $|\delta| = 0.005$, well within the measurement of $\delta = 0.07 \pm 0.3$.

(Al 66) have remarked upon the difficulty of explaining the comparative weakness of the 7.35 MeV → g.s. transition within the framework of True's model. To obtain the requisite cancellation of M2 transition matrix elements would require a $|\, d^2_{5/2}; 0^+ \,\rangle$ amplitude in the ^{14}C g.s. of about 0.75 and seems rather unlikely.

For the Sebe calculation (Se 63) the wavefunction of the mass 14, T=1, $J^\pi = 2^-$ state is

$$
\begin{aligned}
|\, 2^-, T=1 \,\rangle \;=\; & 0.144\, |\, c_{1/2} d_{3/2} \,\rangle \;-\; 0.858\, |\, c_{1/2} d_{5/2} \,\rangle \\
& -0.065\, |\, c_{3/2} s_{1/2} \,\rangle \;-\; 0.021\, |\, c_{3/2} d_{3/2} \,\rangle \\
& -0.484\, |\, c_{3/2} d_{5/2} \,\rangle \;+\; (\text{small})\, |\; \text{E.C.M.} \,\rangle
\end{aligned}
$$

where $|\, c_{1/2} \,\rangle$ and $|\, c_{3/2} \,\rangle$ are $J=\frac{1}{2}$ and $3/2$, $T=\frac{1}{2}$ states of the $|1p^9\rangle$ configuration, and $|\; \text{E.C.M.} \,\rangle$ contains small correction terms for excited centre-of-mass motion. Clearly the "core-excited" configuration $|\, c_{3/2} d_{5/2} \,\rangle$ is quite important in the $|\; 2^- \,\rangle$ wavefunction and may strongly influence the transition rate to the ground state.

7.3 ^{18}Ne Results

7.3. 1 Deformed v. Shell Model States

For some time the nuclei ^{18}O, ^{18}F, and ^{18}Ne were thought to be examples par excellence for the shell model of nuclear states. Thus in ^{18}O for example one would have an inert $\left|1s^4 1p^{12}\right\rangle \equiv \left|^{16}O\right\rangle$ core about which two neutrons circulated in $2s_{1/2}$-$1d_{5/2}$ orbitals. In extreme jj-coupling, six T=1 positive parity states would be formed in this way:

$$\left|d_{5/2}^2\right\rangle \qquad J^\pi = 0^+, 2^+, 4^+$$

$$\left|s_{1/2}^2\right\rangle \qquad J^\pi = 0^+$$

$$\left|d_{5/2}s_{1/2}\right\rangle \qquad J^\pi = 2^+, 3^+.$$

From the ^{17}O spectrum it was known that the $d_{5/2}$-$s_{1/2}$ single-particle splitting was only $\sim$0.87 MeV so that there would be some configuration mixing between the two 0^+ states, and likewise between the 2^+ states. As the $d_{3/2}$ single-particle level occurs at 5.08 MeV in ^{17}O it was thought unlikely that $d_{3/2}^2$ states would occur below 10 MeV excitation, nor $d_{5/2}d_{3/2}$ configurations below about 7 MeV. A large number of workers have performed calculations of ^{18}O

properties using this shell model and with various representations of the residual nucleon-nucleon interaction (e.g., El 55; Fl 64; Ar 68; Cl 68). The results of these have three features in common:

(i) The relative spacings of six of the lower ^{18}O levels (0_1^+, 2_1^+, 4_1^+, 0_2^+, 2_2^+, 3_1^+) could be roughly fitted, as expected, but there was no explanation at all for the existence of two further positive parity levels ($J^\pi = 0^+$ and 2^+ near 5 MeV; fig. 5.2A) lying too low to be ascribed to $d_{3/2}^2$ or $d_{3/2}d_{5/2}$ configurations.

(ii) The $2_1^+ \rightarrow 0_1^+$ E2 transition strength could be fitted with a fairly large effective charge, but the $0_2^+ \rightarrow 2_1^+$ E2 matrix element always showed configurational cancellation effects so that the predicted decay width was one or two orders of magnitude too small.

(iii) Stripping reaction spectroscopic factors gave only patchy agreement with the shell model (Wi 66; Ho 65; Mi 64; Ja 60). The $^{16}O(t,p)$ and $^{17}O(d,p)$ reactions have shown appreciable shell model components in the 0_1^+, 0_3^+, 2_1^+, 2_2^+, 2_3^+, 3_1^+, and 4_1^+ levels, but not in the 0_2^+ state which should have been mainly $\left|s_{1/2}^2\right\rangle$. This non-shell-model aspect of the 0_2^+ level made the strength of the $0_2^+ \rightarrow 2_1^+$

transition particularly mysterious. [It may be noted here that the same situation arises in ^{18}Ne, where the 0_2^+ states is very poorly excited in the ^{16}O(^{3}He,n) reaction.]

The solution to these difficulties was first proposed by Brown (Br 64) who introduced a collective state formed by excitation of two protons from the 1p-shell core into the 2s-1d shell. Although considerable energy is required to raise the two protons, the mutual interaction of the four nucleons in the 2s1d shell is so great as to largely compensate for this and a set of low-lying $p^{-2}(sd)^4$ states are obtained. These turn out to be highly deformed and have a rotational spectrum (seen more clearly in the very similar $(sd)^4$ states of ^{20}Ne). The model also accounts for collective features seen in ^{18}F, ^{18}Ne and ^{16}O levels.

A difficulty in the ^{18}O calculations is the proper selection of the deformed state from the large number of possible $(sd)^4$ states. Brown (Br 64) and Engeland (En 65) used the SU_3 formalism to select the deformed state wavefunctions. Encouraging agreement with experiment was obtained both for the energy spectrum and the E2 transition rates (using an effective charge of 0.5e). Federman and Talmi (Fe 65a,b; Fe 67) performed a similar calculation, but obtained the deformed states by projection from the Nilsson

model, with an effective interaction. Benson and Irvine (Be 66) repeated the calculation using the phenomenological Kallio-Koltveit interaction. These various calculations reproduced reasonably well the additional 0^+ and 2^+ states near 5 MeV, and the observed stripping reaction cross-sections. Shlomo and Moreh (Sh 68) have compared the gamma transition rates predicted by the ^{18}O wavefunctions of (Fe 65a; Be 66; Fe 67) and found that those of (Be 66) gave best agreement with experiment. Accordingly the Benson and Irvine wavefunctions have been used here to calculate the ^{18}Ne level transition widths as a further test.

7.3. 2 The Deformed State Wavefunctions and Matrix Elements

The ^{18}Ne wavefunctions will have the form

$$\left| {}^{18}\mathrm{Ne};J \right\rangle = \alpha \left| \text{Shell Model};J \right\rangle + \beta \left| \text{Deformed};J \right\rangle$$
$$= \alpha \left| (sd)^2;J \right\rangle + \beta \left| p^{-2}(sd)^4;J \right\rangle . \qquad (7.3a)$$

Clearly the shell model and deformed parts will not be connected by the single-body EM transition operators. Matrix elements within the shell model states have been discussed in section 3.1; here we consider matrix elements of the

deformed states following (Fe 67; Be 66; Ben 69; Un 63; Sh 68).

Intrinsic single-particle states $|k\rangle$ of a deformed (Nilsson) potential can be expanded in a spherical basis $|jm\rangle$ using the deformation parameters χ_{jk}

$$|k\rangle = \sum_j \chi_{jk} |j,m=k\rangle \quad . \tag{7.3b}$$

We manufacture our deformed state by placing four nucleons in a Nilsson orbital and projecting out that part of the wavefunction with the desired J and M, and then express this in terms of spherical single particle states. The notation follows (Fe 67; Be 66; Sh 68).

Let P^J_M be the operator (Un 63) which projects out the part of a wavefunction with spin J and projection M on the laboratory z-axis:

Then $P^J_M \left| k_1 k_2 k_3 k_4 \right\rangle$

$$= \sum_{j_1 j_2 j_3 j_4} \chi_1 \chi_2 \chi_3 \chi_4 \; P^J_M \left(\left| j_1 k_1 \right\rangle \left| j_2 k_2 \right\rangle \left| j_3 k_3 \right\rangle \left| j_4 k_4 \right\rangle \right)$$

$$= \sum_{j_i} \chi_1 \chi_2 \chi_3 \chi_4 \; P^J_M \sum_{\substack{J' \; K' \\ J'' \; K'' \\ J''' \; K'''}} (j_1 k_1 j_2 k_2 | J' K') (j_3 k_3 j_4 k_4 | J'' K'')$$

$$\times (J' K' J'' K'' | J''' K''')$$

$$\times \left| j_1 j_2 J'; j_3 j_4 J''; J''' K''' \right\rangle$$

$$= \sum_{j_i} \chi_1 \cdots \chi_4 \sum_{\substack{J' K' \\ J'' K''}} (j_1 k_1 j_2 k_2 | J' K') (j_3 k_3 j_4 k_4 | J'' K'')$$

$$\times (J' K' J'' K'' | JK)$$

$$\times \left| j_1 j_2 J'; j_3 j_4 J''; JM \right\rangle \qquad (7.3c)$$

But $$\left| JM \right\rangle = \sum_{\substack{M' M'' \\ m_i}} (J' M' J'' M'' | JM) (j_1 m_1 j_2 m_2 | J' M')$$

$$\times (j_3 m_3 j_4 m_4 | J'' M'')$$

$$\times \left| j_1 m_1 \right\rangle \left| j_2 m_2 \right\rangle \left| j_3 m_3 \right\rangle \left| j_4 m_4 \right\rangle \qquad (7.3d)$$

whence

$$P^{J}_{M} \left|k_1 k_2 k_3 k_4\right\rangle = \sum \chi_1 \chi_2 \chi_3 \chi_4 \; (j_1 k_1 j_2 k_2 \mid J'K')$$

$$\times \; (j_3 k_3 j_4 k_4 \mid J''K'')(J'K'J''K'' \mid JK)(J'M'J''M'' \mid JM)$$

$$\times \; (j_1 m_1 j_2 m_2 \mid J'M')(j_3 m_3 j_4 m_4 \mid J''M'')$$

$$\times \; \left|j_1 m_1\right\rangle \left|j_2 m_2\right\rangle \left|j_3 m_3\right\rangle \left|j_4 m_4\right\rangle$$

$$= \left|\text{deformed};JM\right\rangle \qquad (7.3e)$$

Now we choose the k = $\frac{1}{2}$ Nilsson orbital (the lowest), associate subscripts 1 and 2 with two protons, and 3 and 4 with two neutrons, and evaluate EM matrix elements in the second quantization formalism with the Rose and Brink phase convention. After some simplification one obtains:

$$\left\langle \text{def};J \,\middle\|\, G_L^{\pi} \,\middle\|\, \text{def};J' \right\rangle$$

$$= \sum_{J_1 J_2 J_2'} (J_1 0 J_2 0 \mid J0)(J_1 0 J_2' 0 \mid J'0)\ \hat{J}'\ \hat{J}_2\ W(J_1 J_2'; J' J_2)$$

$$\times\ \frac{N_2^2(J_1)}{N_4(J) N_4(J')} \sum_{\substack{j_1 j_1' \\ j_2 j_2'}} \chi_1 \chi_2 \chi_3 \chi_4\ (-)^{1+j_2+j_2'}$$

$$\times\ (J_1\, \tfrac{1}{2}\, j_2 - \tfrac{1}{2} \mid J_2 0)(j_1'\, \tfrac{1}{2}\, j_2' - \tfrac{1}{2} \mid J_2' 0)\ C_{12}\ C_{12}'$$

$$\times \left\langle j_1 j_2 J_2 \,\middle\|\, G_L^{\pi}(\text{neutron}) + G_L^{\pi}(\text{proton}) \,\middle\|\, j_1' j_2' J_2' \right\rangle \qquad (7.3f)$$

where $C_{12} = +\sqrt{1 + \delta_{j_1 j_2}}$

$$N_2^2(J_1) = 2 \sum_{j_1 j_2} (j_1\, \tfrac{1}{2}\, j_2 - \tfrac{1}{2}\ J_1 0)^2\ \chi_1^2\ \chi_2^2$$

$$N_4^2(J) = \sum_{J_1 J_2} (J_1 0 J_2 0 \mid J0)^2\ N_2^2(J_1) N_2^2(J_2)$$

and $j_1 = 2s_{1/2}$, $1d_{3/2}$, and $1d_{5/2}$.

The matrix element in the last line is between properly antisymmetrised two-proton or two-neutron states, and effective charges may be inserted into the G^{π}_{L}(nucleon) operators which are those of section 3.1.

7.3. 3 Comparison with Experiment

The ^{18}Ne and ^{18}O transition widths have been calculated using equation 7.3f for the deformation parameters of Benson and Irvine's ^{18}O wavefunctions (Be 66)

$$\chi_{1/2} = -0.46 \qquad \chi_{3/2} = 0.44 \qquad \chi_{5/2} = -0.77$$

and using an effective charge of 0.5e for both neutrons and protons. The results are shown in table 7.3A and the agreement is quite impressive.

One of the more successful ^{18}O shell model treatments is that of Arima et al. (Ar 68) and the predictions of their model for ^{18}Ne have been included for comparison. Their E2 widths were computed using a neutron effective charge of 0.7e, so that the ^{18}Ne widths are obtained from the corresponding ^{18}O ones by multiplying by the factor

TABLE 7.3A

Theoretical and Experimental Transition Widths

Transition Spin	MeV	Width (μeV) Experiment*	Benson (Be 66)	Arima (Ar 68)
		Oxygen - 18		
$2_1^+ - 0_1^+$	1.98 - 0	200 ± 15	230	130
$4_1^+ - 2_1^+$	3.55 - 1.98	⩽ 95	30	30
$0_2^+ - 2_1^+$	3.63 - 1.98	270 ± 45	260	4.3
$2_2^+ - 2_1^+$	3.92 - 1.98	$4000\ ^{+5000}_{-1500}$	13,000	-
$2_2^+ - 0_1^+$	3.92 - 0	$730\ ^{+1000}_{-260}$	900	160
		Neon - 18		
$2_1^+ - 0_1^+$	1.89 - 0	1300 ± 300	800	600
$4_1^+ - 2_1^+$	3.37 - 1.89	350 ± 100	150	140
$0_2^+ - 2_1^+$	3.58 - 1.89	< 330	50	30
$2_2^+ - 2_1^+$	3.62 - 1.89	$11,000\ ^{+5500}_{-3500}$	11,000ø	-
$2_2^+ - 0_1^+$	3.62 - 0	< 1000	400	600

* ^{18}O experimental data from (La 68)

ø Benson model also predicts a $\delta(E2/M1)$ of -0.17 to be compared with the experimental value of $-1.1^{+1.0}_{-0.3}$.

$$\left(\frac{1.7}{0.7}\right)^2 \cdot \left[\frac{E_\gamma(\mathrm{Ne})}{E_\gamma(\mathrm{O})}\right]^5 \qquad (7.3g)$$

As pointed out in section 7.3.1, the Arima model fails badly in the ^{18}O, $0_2^+ \rightarrow 2_1^+$ transition, but the lifetime measurement in ^{18}Ne is not good enough to make the corresponding comparison.

Lastly a comment on the effective charge hypothesis. This is justified in the weak surface coupling model (Bo 53) of interactions between the core and the outer nucleons. In the foregoing treatment the $p_{1/2}^{-2}$ core has been assumed inert. More recently Benson and Flowers (Ben 69) have studied T=0 and T=1 states of ^{18}F arising from $p^{-2}(sd)^4$ configurations in which both $p_{1/2}$ and $p_{3/2}$ holes are permitted, and transitions are found to be further enhanced. They also find that use of Saxon-Woods wavefunctions, because of the larger tail in the radial integrals, gives stronger E2 rates. With these refinements the T=0 state transitions of ^{18}F are well explained <u>without</u> an effective charge. A small effective charge is still needed to explain transitions between T=1 states of ^{18}O, ^{18}F, and ^{18}Ne; the explanation may lie in the admixture of three-particle, one-hole states such as $(1s)^{-1}\ (2s1d)^3$ and $(1p)^{-1}(2s1d)^2(2p1f)^1$ as discussed

by (Ben 69; Ku 59; Br 66; Cl 68).

7.4 Discussion of the ^{26}Si Results

7.4. 1 Spins, Parities and Transition Strengths

The level schemes of ^{26}Mg and ^{26}Si were given in fig. 6.1A. With the possible exceptions of the 4.32 and 4.33 MeV levels (Had 68; Hi 65; En 68) there are no known negative parity levels below 5.5 MeV in ^{26}Mg. This nucleus is the isobaric analogue of ^{26}Si. It is therefore most probable that all of the ^{26}Si levels discussed here are of positive parity. Two of the four ^{26}Si levels between 3.76 and 4.14 MeV might however have negative parity.

In the next two sections we consider the most probable spin and parity assignments for ^{26}Si levels on the basis of the observed properties.

7.4. 2 The 1.80, 2.78 and 3.33 MeV Levels of ^{26}Si

Rolfs and Trost (Ro 68) have shown the spins of the 1.80, 2.78 and 3.33 MeV levels of ^{26}Si to be 2, 2 and 0. They also measured the E2/M1 mixing ratio of the $2^+ \rightarrow 2^+$, 2.78 $\rightarrow$ 1.80

MeV transition* to be $|\delta| = 0.21 \pm 0.10$ or 3.7 ± 1.8.

Using these quantities the transition strengths, $|M|^2$, in Weisskopf units have been calculated (table 7.4B).

All E2 transitions, except the 2.78 → 0 MeV branch, are enhanced. This is also (Haü 68) the case in ^{26}Mg. The 2.78 → 1.80 MeV, M1 transition strength is quite normal (Sk 66). Of particular interest is the 2.78 → 1.80 MeV, E2 transition strength. From the measured lifetime it is possible to exclude the larger solution for $|\delta|$ as the E2 strength would exceed 270 Weisskopf units. This is forbidden by the rigorous $|M|^2 < Z^2 = 196$ sum rule (Wi 60). The smaller solution ($|\delta| = 0.21 \pm 0.10$) is acceptable and gives $|M|^2_{E2} = 29^{+54}_{-24}$. It is unfortunate that the errors are so large on the measured mixing ratio* and lifetime (particularly the former which enters $|M|^2$ as δ^2), nevertheless it is clear that the E2 part of this transition is strong, and it is also (Haü 68) in ^{26}Mg ($|M|^2 = 23.4^{+25}_{-11}$ for the corresponding E2 strength). More accurate determinations

---

* Note that the determination of δ in (Ro 68) may contain a further (non-statistical) error due to possible distortion of the 0.98 MeV angular correlation by the unresolved (with NaI(Tl) detector) 0.97 MeV gamma ray resulting from the 3.76 → 2.78 MeV transition.

of δ and τ would clearly be of interest for this level.

The measured width of the 3.33 → 1.80 MeV transition excludes (Wi 60; Sk 66) multipolarity M2, for it would require $|M|^2_{M2} > 100$. Since the 3.33 MeV state has J=0, and the 1.80 MeV state has $J^\pi = 2^+$, the transition must then be E2, so that we can definitely assign positive parity to the 3.33 MeV level.

7.4. 3 The 3.76, 3.84, 4.09, 4.14, 4.45 and 4.81 MeV Levels of ^{26}Si

Recalling that the 2.03 MeV angular correlation of Rolfs and Trost, assigned to a 3.82 → 1.79 MeV transition, may contain gamma rays from two, or even three, levels of ^{26}Si (section 6.3.4), one has no information from that experiment on the spins of the 3.76 and 3.84 MeV levels observed by the present writer.

From the lower limit on its width (table 6.3C), the 3.76 → 2.78 MeV transition is predominantly (Wi 60; Sk 66) M1 or E1 ($|M|^2 > 100$ if pure E2) so that the level has J = 1, 2 or 3. Lacking D.S.A.M. information on the 3.84 MeV lifetime, one can only note that $J \geq 6$ is excluded by observation of n-γ coincidences (resolving time ~80 ns).

The observation of only the 4.09 → 0 MeV transition

leads to $J^{\pi} = 1^{\pm}$ or 2^{+} for the 4.09 MeV state. Similarly the 4.14 MeV level has spin J = 1 or 2. This is in agreement with (Ro 68) who found $J \leq 3$ from the 4.14 → 1.80 MeV angular correlation. (For the latter NaI(Tl) correlation analysis it was assumed that only one gamma ray entered the 2.34 MeV photopeak. This is confirmed by the present experiments.)

Finally, it appears that both the 4.45 → 1.80 MeV and the 4.81 → 1.80 MeV transitions are E1, M1, or E2, so that the 4.45 and 4.81 MeV levels have $J \leq 4$, but $J^{\pi} \neq 0^{-}, 4^{-}$. (Da 67; Sk 67) tentatively assigned $J^{\pi} = (2^{+})$ to the 4.45 MeV state.

7.4. 4 Analogue Levels in Mass 26

It is of interest to pair analogue levels in ^{26}Mg and ^{26}Si. Up to the 3.33 MeV state the pairing is obvious (fig. 6.1A) and the correspondence in electromagnetic properties is good. The next four ^{26}Mg levels (3.94 up to 4.35 MeV) probably correspond to the ^{26}Si levels from 3.76 up to 4.14 MeV. In ^{26}Mg, the 3.94 MeV level has $J^{\pi} = 3^{+}$ and the 4.32 MeV level almost certainly $J^{\pi} = 4^{(+)}$ (Ha 68; Br 69; Hi 65). There is some confusion over the spins of the ^{26}Mg 4.33 and 4.35 MeV levels, though these lie in the

range J = 1 to 3.

In ^{26}Si, the only candidate for a $J^{\pi} = 4^{(+)}$ assignment is the 3.84 MeV level. This being so, it is clear that the analogue of the ^{26}Mg, 3.94 MeV, $J^{\pi} = 3^{+}$ level must be the ^{26}Si, 3.76 MeV level. The analogous decay schemes support these inferences.

Insufficient information is available to identify higher analog pairs. Those analog levels which have been identified, together with the corresponding (En 68) T=1 levels of ^{26}Al, are shown in fig. 7.4A.

7.4. 5 Shell Model Calculations for Mass 26

Robinson and Bent have considered in some detail (Rob 68) the description of ^{26}Mg by a rotation-vibration model, an asymmetric rotator model, and a vibrational model. All three models gave a poor account of the nucleus - particularly with respect to decays of the second J=2 state, for which none could explain the strengths of the transition to the first J=2 state. It was thought to be of interest to see to what extent a presently feasible shell-model calculation could reproduce observed mass 26 properties.

The calculation of the transition strengths was performed in collaboration with I.S. Towner using the Oxford shell

model programme (To 69). The T=1 states in mass 26 nuclei were described by wave functions constructed by placing 10 nucleons in the orbitals $1d_{5/2}$ and $2s_{1/2}$, an inert core of ^{16}O being assumed. The $1d_{3/2}$ orbit was not included in the shell model configuration space in order that the matrices to be diagonalised could be kept to reasonable proportions; this truncation must be considered as a serious deficiency in the current calculations. The effective interaction between the 10 active nucleons is specified by 16 two-body matrix elements together with 2 single-particle energies describing the interactions with the core. These 18 quantities were taken from the literature and were not adjusted in the current computations. The single particle matrix elements of the electromagnetic transition operators were evaluated using harmonic oscillator wave functions, an oscillator parameter $\alpha = 0.6$ fm^{-1} was used which corresponds to an energy splitting $\hbar\omega$ equal to 15 MeV. For electric transitions an effective charge of 0.5 was used. For magnetic transitions the gyromagnetic ratios g_ℓ and g_s took their corresponding single particle values.

Two shell model calculations were performed. The first used the two body matrix elements and single particle energies which had been obtained empirically by Wildenthal

et al. (Wi 68) from a least squares fit to 80 energy levels in mass 20 to 28 region. The $1d_{3/2}$ orbit was not included in this determination, and consequently the effective interaction contains some renormalisation effects due to this truncation. The predicted spectrum for mass 26 is shown in fig. 7.4A; and the comparison with the experimental data is good, but this is no doubt due to the fact that the low lying levels in mass 26 were used in the fitting criteria.

The second shell model calculation uses the reaction matrix elements of Kuo (Ku 67) which have been calculated from the Hamada-Johnston nucleon-nucleon potential (Ha 64) and include some state dependence, i.e., the matrix elements are corrected for interactions with the ^{16}O core. However, the shell model space used in these determinations is the complete s-d shell. The present calculations do not include the $1d_{3/2}$ orbit, and the Kuo matrix elements used have not been corrected for this truncation. The predicted spectrum for mass 26 is shown in fig. 7.4A. One notes that the lowest calculated 2^+ and 4^+ states (the members of the ground state rotational band of the collective model) lie too low in the spectrum, while the excited 0^+ state is too high. (Only the first few levels of each spin are shown in the figure.)

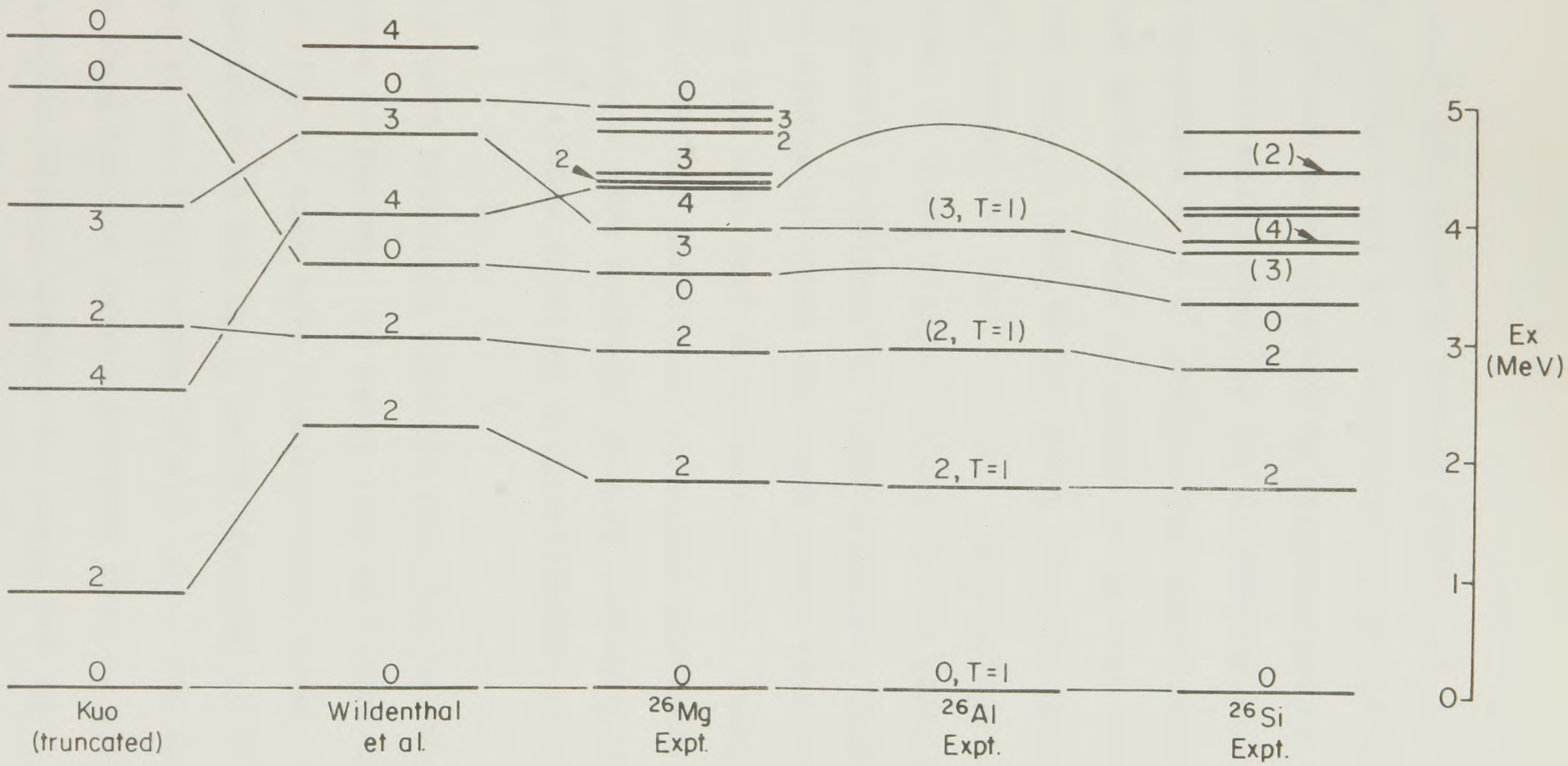

0
0
3
2
4
2
0
4
3
0
2
2
0
Kuo
(truncated)
4
0
3
4
0
2
2
2
0
Wildenthal
et al.
0
3
2
2
3
4
3
0
2
2
0
26Mg
Expt.
(3, T=1)
(2, T=1)
2, T=1
0, T=1
(2)
(4)
(3)
0
2
2
0
26Al
Expt.
26Si
Expt.
5
4
3
2
1
0
Ex
(MeV)

FIGURE 7.4A

Figure 7.4B shows a typical portion of the computer output: in this case the wavefunctions of the first ten $J^{\pi} = 0^{+}$ states were obtained by diagonalisation of the 12 x 12 energy matrix calculated for the Wildenthal elements. The twelve component $J^{\pi} = 0^{+}$ shell-model eigenfunctions are specified by the number of particles in each orbital (i.e., $1d_{5/2}$ and $2s_{1/2}$), and by the spin, isospin, seniority, and reduced isospin for each orbital. Examination of the amplitudes of these eigenfunctions in the various excited states reveals considerable fragmentation. This was usual also for states of other spins and meant that one could not associate the main part of electromagnetic transition strength with any particular component configurations. Other matrices were somewhat larger: computation of the $J^{\pi} = 2^{+}$ and 4^{+} states entailed diagonalisation of 35 x 35 element arrays.

The wave functions obtained from the two calculations were quite different. In table 7.4A is listed the percentage in intensity of each wave function which comes from having zero particles in the $2s_{1/2}$ orbit (denoted by d^{10}), one particle in the $2s_{1/2}$ orbit ($d^{9}s^{1}$), etc.. The wave functions derived from the Kuo matrix elements show considerably more configuration mixing between the $1d_{5/2}$ and $2s_{1/2}$ orbits than those derived from the Wildenthal matrix elements.

TYPICAL ATLAS COMPUTER OUTPUT WILDENTHAL MATRIX ELEMENTS $J^{\pi} = 0^{+}$ STATES

Number of nucleons

N = 10 JT(0, 1) ← Spin and Isospin

12 ← Number of J=0 States

Binding Energy → EB = -106.055 -102.312 -100.954 -96.911 -93.426 -92.049 -89.379 -86.929 -83.684 -81.912

Excitation Energy → EX = 0.000 3.743 5.101 9.144 12.629 14.006 16.676 19.126 22.371 24.143

Component Eigenfunctions Description.

1d5/2 orbital			2s1/2 orbital								
J1	10	1 VT 0	J2	0	0 VT 0	0.654	-0.318	0.532	0.217	0.041	0.121	0.308	0.094	0.124	0.052
J1	9	101 VT11	J2	1	101 VT11	0.284	-0.241	0.094	-0.043	-0.048	-0.017	-0.718	0.048	-0.510	-0.196
J1	8	0 VT 0	J2	2	1 VT 0	0.409	-0.367	-0.625	-0.282	-0.361	-0.129	0.063	-0.098	0.225	0.005
J1	8	0 VT40	J2	2	1 VT 0	0.045	-0.069	-0.145	0.151	0.439	-0.503	0.030	0.357	-0.159	0.184
J1	8	101 VT20	J2	2	100 VT20	-0.004	0.028	0.035	-0.617	0.057	0.257	0.092	0.701	-0.061	-0.042
J1	8	101 VT40	J2	2	100 VT20	-0.032	-0.235	0.051	-0.201	0.425	0.009	-0.383	-0.234	0.310	0.473
J1	8	2 VT 0	J2	2	1 VT 0	0.445	0.622	0.100	-0.432	0.206	-0.243	0.012	-0.288	0.019	-0.022
J1	7	101 VT31	J2	3	101 VT11	0.121	-0.072	-0.347	0.125	0.299	-0.071	0.355	-0.038	-0.471	0.138
J1	7	101 VT51	J2	3	101 VT11	0.010	-0.047	-0.045	0.134	0.244	-0.352	-0.102	0.153	0.423	-0.677
J1	7	103 VT31	J2	3	101 VT11	-0.209	-0.412	0.065	-0.287	0.361	0.128	0.139	-0.144	0.121	-0.095
J1	6	1 VT 0	J2	4	0 VT 0	0.247	0.241	-0.395	0.299	0.348	0.645	-0.169	0.085	0.154	-0.085
J1	6	1 VT40	J2	4	0 VT 0	-0.061	-0.152	0.023	-0.189	0.214	0.171	0.212	-0.399	-0.329	-0.453

Amplitudes of Component Eigenfunctions in the Calculated Fourth $J^{\pi} = 0^{+}$ State.

100 × total orbital spin + total orbital isospin

Number of nucleons in Orbital

Seniority (V) and Reduced Isospin (T) for orbital

Figure 7·4B

TABLE 7.4A

Percentage Calculated $(s,d)^{10}$ Configuration Intensities for A=26

		d^{10}	d^9s^1	d^8s^2	d^7s^3	d^6s^4	
0_1^+	W:	43	8	37	6	6	0_1^+
	K:	1	-	27	29	43	
0_2^+	W:	10	6	58	18	8	0_2^+
	K:	4	2	67	19	8	
0_3^+	W:	28	1	43	13	15	0_3^+
	K:	22	4	33	8	33	
2_1^+	W:	22	33	23	18	4	2_1^+
	K:	-	5	15	42	38	
2_2^+	W:	12	26	33	21	8	2_2^+
	K:	2	6	36	44	12	
3_1^+	W:	-	42	44	14	-	3_1^+
	K:	-	14	19	48	19	
4_1^+	W:	32	20	34	11	3	4_1^+
	K:	-	2	19	41	38	

W:= (Wi68) K:= (Ku67)

There are two reasons for this:

(i) The single particle energy splitting $\varepsilon_{s_{1/2}} - \varepsilon_{d_{5/2}}$ was found empirically by Wildenthal to be 1.05 MeV, whereas for the calculation with the Kuo matrix elements the splitting was taken from the experimental spectrum of ^{17}O, i.e., 0.87 MeV. The smaller the splitting the greater the configuration mixing.

(ii) The average T=1 configuration interaction, defined by

$$W = (1/12) \sum_{J} (2J+1) \left\langle ds \left| V \right| ds \right\rangle_{J,T=1}$$

is repulsive (i.e., positive) for the Wildenthal matrix elements and is attractive for the Kuo matrix elements. The more attractive is W, the greater the configuration mixing.

A comparison of the calculated and experimental electromagnetic transition strengths $|M|^2$ is given in table 7.4B, where $|M|^2$ is quoted in Weisskopf Units (Wi 60). The essential features of the comparison are:

(i) The ratio of E2 transition strengths in the ground state rotational band

$$R = \frac{(M^2;\ 4_1^+ - 2_1^+)}{(M^2;\ 2_1^+ - 0_1^+)}$$

TABLE 7.4B

Comparison of Calculated and Measured Transition Strengths

Transition and Multipolarity			^{26}Mg			^{26}Si		
J_i	J_f	L^π	$\|M\|^2$ Wildenthal	$\|M\|^2$ Kuo	$\|M\|^2$ Expt.	$\|M\|^2$ Wildenthal	$\|M\|^2$ Kuo	$\|M\|^2$ Expt.
2_1	0_1	E2	8.1	8.5	$17^{+4}_{-2.7}$	5.6	7.5	7^{+11}_{-4}
2_2	0_1	E2	0.17	0.75	$1.88^{+1.12}_{-0.75}$	1.03	0.29	$1.6^{+2.4}_{-0.8}$
	2_1	M1	0.33	0.14	$0.37^{+0.22}_{-0.12}$	0.3	0.13	$0.11^{+0.17}_{-0.05}$
		E2	10	2.2	23.4^{+25}_{-11}	7.1	0.84	29^{+51}_{-24}
		(δ)	(+)	(-)		(-)	(+)	(+)
0_2	2_1	E2	0.08	0.1	$3.25^{+2.2}_{-1.4}$	0.002	0.26	$7.8^{+4.5}_{-4.0}$
	2_2	E2	12	11	<20	8.0	4.7	<40
3_1	0_1	M3	0.022	0.45		0.013	0.11	
	2_1	M1	0.055	0.31	$0.0023^{+0.0007}_{-0.0005}$	0.039	0.30	0.004
		E2	0.003	0.77		2.4	0.50	
		(δ)	(+)	(-)		(-)	(+)	
	2_2	M1	0.09	0.08	$0.034^{+0.010}_{-0.007}$	0.10	0.06	>0.015
		E2	7.1	7.6		6.1	8.0	
		(δ)	(+)	(+)		(-)	(-)	
4_1	2_1	E2	0.03	10.2	$5.8^{+2.8}_{-1.2}$	0.007	9.5	
		[Branch]				[5%]	[100%]	[100%]
	2_2	E2	4.5	0.04	<2.2	4.0	0.0023	
		[Branch]				[95%]	[0.001%]	[<15%]
0_3	2_1	E2	0.47	0.09	<0.4	1.0	0.41	
	2_2	E2	0.56	0.00037	$9.3^{+5.3}_{-3.3}$	0.7	0.79	
4_2	2_1	E2	9.0			7.6		
	2_2	E2	0.75			0.38		

The initial and final states all have positive parity; the notation is J_n for the n^{th} state of spin J. Transition strengths are $|M|^2$ in Weisskopf Units. Experimental values for ^{26}Mg are from (Haü68) and for ^{26}Si from this work. "Wildenthal" refers to calculations based on the matrix elements of (Wi68), "Kuo" to (Ku67). Where an E2/M1 mixing ratio occurs, its sign is given in the third row. Only branching ratios were determined for the 4 → 2 transition in ^{26}Si: these are given in square brackets.

is calculated to be approximately the same for ^{26}Mg and ^{26}Si, and with the Kuo matrix elements R = 1.25, whilst the rotational model predicts R = 10/7. The experimental value for ^{26}Mg is R = 0.34 ± 0.1. The Wildenthal matrix elements give ($|M|^2$; $4_1^+ \rightarrow 2_1^+$) to be 100 times too weak. Hence the corresponding value for R is likewise too small.

Furthermore the experimental ratios in ^{26}Si for the decay of the 4_1^+ state indicate almost 100% decay to the 2_1^+ state and less than 15% to the 2_2^+ state. The Wildenthal prediction is the complete opposite of this, namely 95% decay to the 2_2^+ state and 5% to the 2_1^+ state. The situation for ^{26}Mg is similar. The second excited 4^+ state predicted by Wildenthal lies at 1.4 MeV above the first 4^+ state. The prediction for this level is ($|M|^2$; $4_2^+ \rightarrow 2_1^+$) = 9.0 for ^{26}Mg and 7.6 for ^{26}Si. Thus if this level is identified with the ground state rotational band, then the ratio R = 1.05 is in much closer agreement with the collective model. Furthermore the branching ratios for this level agree with experiment if one identifies the second calculated 4^+ state of Wildenthal with the lowest experimental 4^+ state.

(ii) The experimental decay of the second 2^+ state is fairly well reproduced in magnitude by both shell model calculations. However the sign of the E2/M1 mixing ratio,

δ, in the $2_2^+ \rightarrow 2_1^+$ transition is of some interest. Kuo predicts δ = +0.08 for ^{26}Si and δ = -0.12 for ^{26}Mg, whereas Wildenthal predicts δ = -0.05 for ^{26}Si and δ = +0.06 for ^{26}Mg; that is the two calculations predict opposite signs for the mixing ratios. Experimentally the ^{26}Si mixing ratio is determined to be positive, whereas only the magnitude* of the ^{26}Mg mixing ratio is known, $|\delta|$ = 0.12. These results again suggest that the Kuo matrix elements give a better agreement with experiment.

(iii) The calculated E2 decay strengths for the excited 0^+ state, viz. ($|M|^2$; $0_2^+ \rightarrow 2_1^+$) is too weak by an order of magnitude in both calculations. This suggests that the excited 0^+ state has a deformed character which is not reproduced by a shell model calculation in a restricted

---

* The phase-consistency of the present calculations was assured in the following manner: (i) consistent usage of the definitions of eigenfunctions and operators of (Ro 67), (ii) semi-empirical checks on the phases of the two-body matrix elements of Kuo and Wildenthal et al. by reproducing the correct signs of $2_2^+ \rightarrow 2_1^+$, E2/M1 mixing ratios in ^{18}O and ^{18}Ne. The only two-body matrix element which is different in sign when comparing the two sets is the $\langle dd | V | dd \rangle_{21}$ element; however, at least for mass 18, one can easily see that this does not alter the relative signs of eigenfunction-coefficients and hence the mixing ratios.
The experimental sign of the E2/M1 mixing ratio in ^{26}Si was extracted phase-consistently (Ro 67) from the A_2 and A_4 values given in (Ro 68). It was not possible to trace the relation of the sign of the experimental mixing ratio (Br 63) in ^{26}Mg. Therefore, only the magnitude could be used.

configuration space. The inclusion of the $1d_{3/2}$ orbit into the calculation would have a big effect on the wave function for this state.

To conclude, the $(1d_{5/2} \rightarrow 2s_{1/2})^{10}$ shell model calculations succeed to some extent where the collective model has failed: the account given of the $2_2 \rightarrow 2_1$ decays is somewhat better. One anticipates that calculations including the $1d_{3/2}$ shell would improve the description of the first few states in mass 26 considerably.

The Moving Finger writes; and having writ,
Moves on; nor all thy Piety nor Wit
Shall lure it back to cancel half a Line,
Nor all thy Tears wash out a Word of it.

Omar Khayyam.
(Fitzgerald.)

REFERENCES

Ad 68 J.M. Adams et al., J. of Phys. A (Proc. Phys. Soc. Lond.) Ser 2, 1 (1968) 549.

Aj 60 F. Ajzenberg-Selove and K.L. Dunning, Phys. Rev. 119 (1960) 681.

Aj 68 F. Ajzenberg-Selove and T. Lauritsen, Nucl. Phys. A114 (1968) 1.

Al 63 D.E. Alburger and E.K. Warburton, Phys. Rev. 132 (1963) 790.

Al 66 D.E. Alburger et al., Phys. Rev. 148 (1966) 1050.

Al 68 K.W. Allen et al., Can.J.Phys. 46 (1968) 1575.

An 68 R. Anderson, University of Oxford Nuclear Physics Laboratory Report 11 (1968).

An 68a R. Anderson, D.Phil.Thesis, University of Oxford (1968).

Ar 66 N.P. Archer et al., Nucl. Instr. 44 (1966) 114.

Ar 68 A. Arima et al., Nucl. Phys. A108 (1968) 94.

Ba 58 E. Baranger and S. Meshkov, Phys.Rev.Lett. 1 (1958) 30.

Ba 61 R. Batchelor et al., Nucl.Instr.Meth. 13 (1961) 70.

Ba 60 R. Batchelor et al., Nucl.Instr.Meth. 8 (1960) 146.

Ba 70 K. Bharuth-Ram, D.Phil.Thesis, University of Oxford, 1970.

Be 55 R.D. Bent et al., Phys.Rev. 100 (1955) 771.

Be 66 H.G. Benson and J.M. Irvine, Proc.Phys.Soc. 89 (1966) 249.

Be 68 R.A.I. Bell et al., Nucl.Phys. A118 (1968) 481.

Be 69 R.A.I. Bell et al., 'Level Energies and Lifetimes in ^{26}Si', Oxford University Nuclear Physics Laboratory Preprint 15/69; submitted for publication in Nucl. Phys.

Ben 69 H.G. Benson and B.H. Flowers, Nucl.Phys. A126 (1969) 305 and Ibid 332.

Bl 66 A.E. Blaugrund, Nucl.Phys. 88 (1966) 501.

Bl 67 A.E. Blaugrund et al., Phys.Rev. 158 (1967) 893.

Blk 67 R.S. Blake et al., Nucl.Phys. A102 (1967) 305.

Bl 69 J. Bleck et al., Nucl. Phys. A123 (1969) 65.

Bo 53 A. Bohr and B.R. Mottleson, Mat.Fys.Medd.Dan.Vid. Selsk. 27, no. 16 (1953) (ed. 2, 1957).

Bo 63 R.R. Borchers and C.H. Poppe, Phys.Rev. 129 (1963) 2679.

Br 63 C. Broude and H.E. Gove, Ann.Phys. 23 (1963) 71.

Br 64 G.E. Brown, Congres International de Physique Nucleaire, Paris, 1 (1964) 129.

Br 66 G.E. Brown and T.T.S. Kuo, Nucl.Phys. A108 (1968) 27.

Bry 64 H.C. Bryant et al., Nucl.Phys. 53 (1964) 97.

Br 69 C. Broude et al., Can.J.Phys. (1969), to be published.

Ca 66 R.R. Carlson, Phys.Rev. 148 (1966) 991.

Cl 61 A.B. Clegg et al., Proc. Phys. Soc. 79 (1962) 1017.

Cl 61a A.B. Clegg, Phil.Mag. 6 (1961) 1207.

Cl 68 D.M. Clement and E.U. Baranger, Nucl.Phys. A108 (1968) 27.

Cl 68a H.G. Clerc and E. Kuphal, private communication, 1968, to be published.

Co 65 S. Cohen and D. Kurath, Nucl.Phys. 73 (1965) 1.

Co 67 W.R. Coker et al., Nucl. Phys. A91 (1967) 97.

Da 61 J.A. Davies and G.A. Sims, Can.J.Chem. 39 (1961) 601.

Da 67 W.G. Davies et al., PLA Prog. Rep. (Rutherford Lab. Rep.) RHEL/R 156 (1967) 111.

Do 61 P.F. Donovan et al., Phys.Rev. 123 (1961) 589.

Ea 68 L.G. Earwaker and J.H. Montague, Nucl.Phys. A109 (1968) 507.

El 55 J.P. Elliott and B.H. Flowers, Proc.Roy.Soc.A, 229 (1955) 536.

El 56 J.P. Elliott, Phil.Mag., 1 (1956) 503.

En 65 T. Engeland, Nucl.Phys. 72 (1965) 68.

En 68 P.M. Endt and C. Van der Leun, Nucl.Phys. A105 (1968) 1.

Fe 65a P. Federman and I. Talmi, Phys.Lett., 15 (1965) 165.

Fe 65b P. Federman and I. Talmi, Phys.Lett., 19 (1965) 491.

Fe 67 P. Federman, Nucl.Phys. A95 (1967) 443.

Fi 59 O.B. Firsov, J.E.T.P. (U.S.S.R.) 36 (1959) 1517.

Fl 64 B.H. Flowers and D. Wilmore, Proc.Phys.Soc., 83 (1964) 683.

Ga 66 A. Gallmann et al., Phys.Rev. 151 (1966) 735.

Gi 68 R.D. Gill, D.Phil.Thesis, University of Oxford (1968).

Gi 68a R.D. Gill, B.C. Robertson, J. L'Ecuyer, R.A.I. Bell and H.J. Rose: Phys.Lett. 28B (1968) 116.

Gl 63 P.W.M. Glaudemans and P.M. Endt, Nucl.Phys. 42 (1963) 367.

Gl 66 R.N. Glover and A.D.W. Jones, Nucl.Phys. 81 (1966) 277.

Gl 66a R.N. Glover and A.D.W. Jones, Nucl.Phys. 84 (1966) 673.

Go 59 H.E. Gove and A.E. Litherland, Phys.Rev. 113 (1959) 1078.

Gr 62 L.L. Green et al., Proc. Phys.Soc. 79 (1962) 1017.

Gu 68 K. Gul, B.H. Armitage and B.W. Hooton, Nucl.Phys. A122 (1968) 81.

Ha 57 E.C. Halbert and J.B. French, Phys.Rev. 105 (1957) 1563.

Ha 64 T. Hamada and I.D. Johnston, Nucl.Phys., 53 (1964) 87.

Ha 66 O. Haüsser, J.S. Lopes, H.J. Rose and R.D. Gill, University of Oxford Nuclear Physics Laboratory Report (1966).

Ha 68 M. Hagen et al., Phys.Lett. 26B (1968) 432.

Haü 68 O. Haüsser et al., Can.J.Phys. 46 (1968) 1035.

Hi 65 S. Hinds et al., Nucl.Phys. 67 (1965) 257.

In 53 D.R. Inglis, Rev.Mod.Phys. 25 (1953) 390.

Ja 60 A.A. Jaffe et al., Proc.Phys.Soc. 76 (1960) 914.

Ja 54 B. Jancovici and I. Talmi, Phys.Rev. 95 (1954) 289.

Ja 62 L. Jarczyk et al., Nucl.Instr. 17 (1962) 310.

Jo 59 G.A. Jones et al., Phil.Mag. 4 (1959) 796.

Jo 68 D.W. Jones, I.E.E.E. Trans. Nuc.Sci. 15, no.3. (1968) 491.

Kr 66 M. Krick and G.J.F. Legge, Nucl.Phys. 89 (1966) 63.

Ku 56 D. Kurath, Phys.Rev. 101 (1956) 216.

Ku 57 D. Kurath, Phys.Rev. 106 (1957) 975.

Ku 59 D. Kurath, Nucl.Phys. 14 (1959) 398.

Ku 67 T.T.S. Kuo, Nucl.Phys., A103 (1967) 71.

La 65 J.M. Lacambra et al., Nucl.Phys. 68 (1965) 273.

La 67 B. Lalovic, Nuc.Instr.Meth. 47 (1967) 173.

La 68 P. Lawson, D.Phil.Thesis, University of Oxford, 1968.

La 68a P.G. Lawson, Oxford University Nuclear Physics Laboratory Report (1968).

Le 50 H.W. Lewis, Phys.Rev. 78 (1950) 526.

L'Ec 69 J.L'Ecuyer et al., private communication (1969).

Li 61 A.E. Litherland and A.J. Ferguson, Can.J.Phys. 39 (1961) 788.

Li 63 A.E. Litherland et al., Nucl.Phys. 44 (1963) 220.

Li 63a A.E. Litherland, M.A. Clark and C. Broude, Phys.Lett. 3 (1963) 204.

Lin 63 J. Lindhard, M. Scharff and H.E. Schiott, Dan. Vid.Selsk., Matt.Fys.Medd. 33 (1963) No.14.

Lo 66 J.S. Lopes et al., Nucl.Phys. 89 (1966) 127.

Lo 67 J.S. Lopes, D.Phil.Thesis, University of Oxford, 1967.

Ma 63 J.B. Marion and J.L. Fowler, Fast Neutron Physics, Interscience Publ., 1963.

Ma 68 J.B. Marion, Nuclear Data A4 (1968) 301.

Mc 55 J.N. McGruer et al., Phys.Rev. 100 (1955) 235.

Mc 67 W.R. McMurray et al., Nucl.Phys. 92 (1967) 401.

Mi 64 R. Middleton and D.J. Pullen, Nucl.Phys. 51 (1964) 63.

Mi 67 R.G. Miller and R.W. Kavanagh, Nucl.Phys. A94 (1967) 261.

Mo 58 W.E. Moore et al., Phys.Rev.Lett. 1 (1958) 29.

Mo 65 R. Moreh and T. Daniels, Nucl.Phys. 74 (1965) 403.

Mu 58 R.B. Murray, Nucl. Instr. 2 (1958) 237.

Mu 66 S. Mubarakmand, D.Phil.Thesis, University of Oxford, 1966.

Mu 67 G.L. Murray and B.E.F. Macefield, Nucl.Instr.Meth. 51 (1967) 229.

NE 68 Nuclear Enterprises (G.B.) Ltd. Catalogue (1968).

Ol 65 J.W. Olness et al., Phys.Rev. 139 (1965) B512.

Ol 65a R.W. Ollerhead et al., Nucl.Phys. 66 (1965) 161.

Ol 66 J.W. Olness and D.H. Wilkinson, Phys.Rev. 141 (1966) 966.

Ol 67 J.W. Olness et al., Phys.Rev. 161 (1967) 1131.

Or 63 J.H. Ormrod and H.E. Duckworth, Can.J.Phys. 41 (1963) 1424.

Or 65 J.H. Ormrod, J.R. MacDonald and H.E. Duckworth, Can. J. Phys. 43 (1965) 275.

Ow 58 R.B. Owen, Nuclear Electronics, U.N. Atomic Energy Agency (1958).

Ow 62 R.B. Owen, I.R.E. Trans. Nuc. Sci. 9, No.3. (1962) 285.

Ph 67 G.W. Phillips et al., Phys.Rev. 159 (1967) 891.

Po 62 D. Powers and W. Whaling, Phys.Rev. 126 (1962) 61.

Po 63 A.M. Pozkanzer, Phys.Rev. 129 (1963) 385.

Po 64 A.R. Poletti, D.Phil.Thesis, University of Oxford, 1964.

Po 65 A.R. Poletti and E.K. Warburton, Phys.Rev. 137B (1965) 595.

Po 67 A.R. Poletti et al., Phys.Rev. 155 (1967) 1096.

Ra 58 W.K. Rasmussen et al., Phys.Rev. 110 (1958) 154.

Ro 53 M.E. Rose, Phys.Rev. 91 (1953) 610.

Ro 60 H.J. Rose, Nucl.Phys. 19 (1960) 113.

Ro 64 H.J. Rose et al., Nucl.Phys. 52 (1964) 481.

Ro 64a J.R. Hook and D. Mitra, Nucl.Phys. 51 (1964) 96.

Ro 67 H.J. Rose and D.M. Brink, Revs.Mod.Phys. 39 (1967) 306.

Ro 68a H.J. Rose et al., Revs.Mod.Phys., 40 (1968) 591.

Ro 68 C. Rolfs and W. Trost, Nucl.Phys. A122 (1968) 633.

Rob 68 S.W. Robinson and R.D. Bent, Phys.Rev. 168 (1968) 1266.

Ro 69 B.C. Robertson, R.A.I. Bell, J. L'Ecuyer, R.D. Gill and H.J. Rose: Nucl.Phys. A126 (1969) 431.

Ro 69a B.C. Robertson, D.Phil.Thesis, Oxford University, 1969.

Ru 59 A.H. Rutledge, A.E.C. Report CRP-85L (1959).

Se 63 T. Sebe, Progr. Theoret.Phys. (Kyoto) 30 (1963) 290.

Sh 68 S. Shlomo and R. Moreh, Nucl.Phys. A110 (1968) 204.

Si 67 K. Siegbahn, Alpha-, Beta-, and Gamma-Ray Spectroscopy, North-Holland (1966).

Sk 66 S.J. Skorka et al., Nucl. Data 2 (1966) 347.

Sk 67 D.J. Skyrme, D.Phil.Thesis, University of Oxford, 1967.

Sp 67 E. Spamer and H. Artus, Zeit.Phys. 198 (1967) 445.

St 68 D.F.H. Start, D.Phil.Thesis, University of Oxford (1968).

Ta 60 I. Talmi and I. Unna, Ann.Rev.Nuc.Sci. 10 (1960) 353.

Th 66 M.F. Thomas et al., Nucl.Phys. 78 (1966) 298.

Tow 61 J.H. Towle and B.E.F. Macefield, Proc.Phys.Soc. 77 (1961) 399.

Tow 68 J.H. Towle and G.J. Wall, Nucl.Phys. A118 (1968) 500.

To 68 D.D. Tolbert et al., Phys.Rev.Lett., 21 (1968) 1535.

To 69 I.S. Towner and W.G. Davies, 1969, unpublished.

Tr 63 W.W. True, Phys.Rev. 130 (1963) 1530.

Un 58 I. Unna and I. Talmi, Phys.Rev. 112 (1958) 452.

Un 63 I. Unna, Phys.Rev. 132 (1963) 2225.

Vi 57 W.M. Visscher and R.A. Ferrell, Phys.Rev. 107 (1957) 781.

Wa 59 A.H. Wapstra, G.J. Nijgh, and R. van Lieshout, Nuclear Spectroscopy Tables, North-Holland (1959).

Wa 60 E.K. Warburton and W.T. Pinkston, Phys.Rev. 118 (1960) 733.

Wa 64 E.K. Warburton et al., Phys.Rev. 133 (1964) B42.

Wa 65 E.K. Warburton et al., Phys.Rev. 138 (1965) B104.

Wa 66 E.K. Warburton and H.J. Rose, Phys.Rev. 109 (1966) 1199.

Wa 67 B. Wakefield, D.Phil.Thesis, University of Oxford, 1967.

Wi 60 D.H. Wilkinson, in Nuclear Spectroscopy, Part B, ed. by F. Ajzenberg-Selove (Academic Press, New York, 1960).

Wi 62 A. van Wijngaarden and H.E. Duckworth, Can.J.Phys. 40 (1962) 1749.

Wi 66 J.L. Wiza et al., Phys.Rev. 141 (1966) 975.

Wi 68 B.H. Wildenthal et al., Phys.Lett. 26B (1968) 692.

Za 66 L. Zamick, Phys.Lett. 21 (1966) 194.